CHALMERS
UNIVERSITY OF TECHNOLOGY

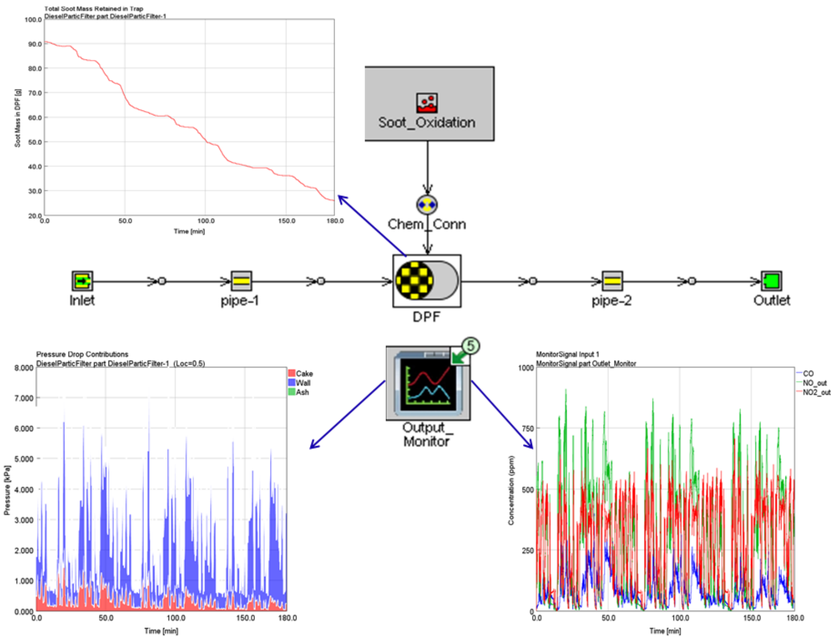

# 1D Modeling and Simulations of Soot Oxidation in Diesel Particulate Filters and Monoliths using GT-POWER

MASTER'S THESIS IN INNOVATIVE AND SUSTAINABLE
CHEMICAL ENGINEERING

CHANIN LERDMALEEWONG &
STAFFAN LUONG

Department of Applied Mechanics
CHALMERS UNIVERSITY OF TECHNOLOGY
Gothenburg, Sweden 2016

MASTER'S THESIS IN INNOVATIVE AND SUSTAINABLE CHEMICAL ENGINEERING

# 1D Modeling and Simulations of Soot Oxidation in Diesel Particulate Filters and Monoliths using GT-POWER

CHANIN LERDMALEEWONG & STAFFAN LUONG

Department of Applied Mechanics
*Division of Combustion*
CHALMERS UNIVERSITY OF TECHNOLOGY
Gothenburg, Sweden 2016

1D Modeling and Simulations of Soot Oxidation
in Diesel Particulate Filters and Monoliths using GT-POWER
CHANIN LERDMALEEWONG & STAFFAN LUONG

Supervisor: Soran Shwan, Volvo Group Trucks Technology (GTT)
Examiner: Jonas Sjöblom, Department of Applied Mechanics

Master's Thesis 2016:26
ISSN 1652-8557
Department of Applied Mechanics
Division of Division Combustion
Chalmers University of Technology
SE-412 96 Gothenburg
Telephone +46 31 772 1000

Cover: The cover page figure represents a typical flow-sheet layout of modules for exhaust aftertreatment simulations in GT-POWER. The plots are from one of the simulations of this work regarding soot oxidation with $NO_2$ in DPF, where The bottom left plot shows the pressure drop contribution from the soot layer and filter wall and the plot on the other side represents the outlet concentration of $NO_x$ and $CO$. The plot on top monitors the change of soot mass inside DPF during soot oxidation by $NO_2$.

Typeset in LaTeX
Printed by Reproservice
Gothenburg, Sweden 2016

1D Modeling and Simulations of Soot Oxidation in Diesel Particulate Filters and Monoliths using GT-POWER

Master's thesis in *Innovative and Sustainable Chemical Engineering*
CHANIN LERDMALEEWONG & STAFFAN LUONG
Department of Applied Mechanics
Chalmers University of Technology

# Abstract

Diesel particulate filter (DPF) is part of the exhaust aftertreatment system for diesel engines. The DPF's main function is to trap particulate matter (soot) from the exhaust stream. The trapped soot is removed by regeneration of the filter. The regeneration process involves soot oxidation via oxygen and nitrogen dioxide. Simulations on kinetics and pressure drop are widely used in the assessment of the DPF. In this work detailed kinetic models of soot oxidation (by oxygen) were investigated and implemented in a flow-through monolith model and also in a DPF model using GT-POWER. The detailed kinetic models and data origins from previously published data. The DPF model consists of a number of interrelated sub-models soot oxidation by $NO_2$, $NO$ oxidation and pressure drop. These sub-models were developed by using semi-steady state and transient engine data on a catalyzed DPF. Kinetics and pressure drop analysis were found to be the key in finding parameters for the models. The implementation of these models into GT-POWER required some special techniques due to rigid built-in model structure. The detailed kinetics was adequate to predict the low temperature experiment, in general, the detailed kinetic model was able to reduce the residual by approximately 25% compared to global kinetics model.

Keywords: GT-POWER, Diesel Particulate Filter, Soot Oxidation, Detailed Kinetics Modeling, 1-D Simulation, Pressure Drop Model

# Acknowledgements

Per-Anders Carlson, Wang-Hansen Carolin, Competence Centre for Catalysis (KCK) and Chalmers University of Technology for providing the experimental data of soot oxidation for this thesis.

AB Volvo and EATS simulation group for providing DPF experimental data that was used in this thesis to develop the DPF model.

CHANIN LERDMALEEWONG & STAFFAN LUONG, Gothenburg, June 2016

# Contents

# List of Figures

# List of Tables

# Notations

| | |
|---|---|
| ASC | Ammonia Slip Catalyst |
| BDF | Back Diffusion Formula |
| CCRT© | Catalytic Continuously Regenerating Trap |
| CDPF | Catalyzed Diesel Particulate Filter |
| CO | Carbon monoxide |
| $CO_2$ | Carbon dioxide |
| CRT© | Continuously Regenerating Trap |
| DOC | Diesel Oxidation Catalyst |
| DPF | Diesel Particulate Filter |
| EATS | Exhaust After-treatment System |
| HC | Hydrocarbon Compound |
| NO | Nitrogen monoxide, also known as nitric acid |
| $NO_2$ | Nitrogen dioxide |
| ODE | Ordinary Differential Equation |
| PM | Particulate Matter |
| QS | Quasi-Steady |
| RK | Range-Kutta |
| SCR | Selective Catalytic Reduction |
| TEM | Transmission Electron Microscope |
| TWC | Three-Way Catalyst |

| | |
|---|---|
| $[i]$ | denoted concentration of species $i$ |
| `i` | denoted the index of the slab |
| $z$ | denoted vector in axial direction ($m$) |
| $-^*$ | superscript denoted reactive species |
| $-_g$ | subscript denoted gas |
| $-_i$ | subscript denoted species |
| $-_j$ | subscript denoted reaction index |
| $-_k$ | subscript denoted surface site family |
| $-_s$, $-^s$ | subscript and superscript denoted substrate |
| $-_0$ | subscript denoted initial properties |
| $-_{ash}$ | subscript denoted properties of ash |
| $-_{cake}$ | subscript denoted soot cake |
| $-_{ext}$ | subscript denoted properties of external source |
| $-_{pore}$ | subscript denoted properties of pore |
| $-_{soot}$ | subscript denoted properties of soot |

| | |
|---|---|
| $\Delta G$ | Gibbs energy ($J/mol$) |
| $\Delta S$ | Reaction's entropy ($J/mol \cdot K$) |
| $\beta$ | Forchheimer factor ($m^{-1}$) |
| $\Delta H_j$ | Enthalpy of reaction index $j$ $\left(\frac{J}{mol}\right)$ |
| $\Delta P$ | Pressure drop ($Pa$) |
| $\dot{m}$ | Mass flow rate $\left(\frac{kg}{s}\right)$ |
| $\dot{n}$ | Molar flow rate $\left(\frac{mol}{s}\right)$ |
| $\dot{V}$ | Volumetric flow $\left(\frac{m^3}{s}\right)$ |
| $\epsilon$ | Reactor void fraction/ porosity |
| $\epsilon_{cake}$ | Soot cake porosity |
| $\epsilon_s(\mathtt{i}, 0)$ | Clean filter porosity slab `i` |
| $\epsilon_s(\mathtt{i}, t)$ | Filter porosity of the slab `i` at time $t$ |
| $\eta_i$ , $n_i$ | Order on concentration term of species $i$ |
| $\eta_{DR}$ | Combined spherical unit collector efficiency |
| $\eta_D$ | Single spherical unit collector efficiency due to particle interception |
| $\eta_R$ | Single spherical unit collector efficiency due to Brownian diffusion |
| $\kappa_{T,i}$ | Thermal conductivity of species $i$ $\left(\frac{J}{m \cdot s \cdot K}\right)$ |
| $\lambda_k$ | Active site density of site family $k$ $\left(\frac{mol}{m^3}\right)$ |
| $_{w,s}(\mathtt{i}, 0)$ | Mass of soot in the slab `i` at time $t$ ($kg$) |
| $\mu$ | Dynamic viscosity $\left(\frac{kg}{m \cdot s}\right)$ |
| $\mu_m$ | Reduce mass ($kg$) |
| $\omega_i$ | Mass fraction of species $i$ |
| $\rho_i$ | Density $\left(\frac{kg}{m^3}\right)$ |
| $\rho_{soot,cake}$ | Soot packing density in the cake layer $\left(\frac{kg}{m^3}\right)$ |
| $\rho_{soot,s}$ | Soot packing density in the wall substrate $\left(\frac{kg}{m^3}\right)$ |
| $\sigma_{ik}$ | Stoichiometric coefficient for species $i$ in site family $k$ |
| $\sigma_{O-C}$ | Average bond length between oxygen and carbon atom ($m$) |
| $\tau$ | Torosity |
| $\theta_i$ | Surface coverage of species $i$ |
| $\xi$ | Channel pressure drop correlation |
| $A_d$ | Area of a surface site on carbon spherules ($m^2$) |
| $A_j$ | Pre-exponential factor of reaction index $j$ |
| $C_i$ | Concentration of species $i$ $\left(\frac{mol}{m^3}\right)$ |
| $C_{p,i}$ | Specific heat capacity $\left(\frac{J}{kg \cdot K}\right)$ |
| $D$ | Channel diameter ($m$) |
| $d_0$ | Spherules diameter ($m$) |
| $d_c(\mathtt{i}, 0)$ | Clean filter unit collector diameter of the slab `i` |
| $d_c(\mathtt{i}, t)$ | Unit collector diameter of the slab `i` at time $t$ |
| $D_h$ | Hydraulic diameter ($m$) |
| $D_i$ | Diffusion coefficient of species $i$ $\left(\frac{m^2}{s}\right)$ |
| $D_i$ | Effective diffusion coefficient of species $i$ $\left(\frac{m^2}{s}\right)$ |
| $d_{pore}$ | Average pore diameter ($m$) |
| $E(\mathtt{i}, t)$ | Collection efficiency of slab `i` at time $t$ |

| | |
|---|---|
| $E_{A,j}$ | Activation energy of reaction index $j$ |
| $f$ | Friction factor |
| $f(\epsilon_{cake})$ | Kuwabara function for soot unit cell in cake layer |
| $f_j(\theta)$ | Surface coverage function for reaction index $j$ |
| $g(\epsilon_s)$ | Kuwabara function for soot unit cell in deep bed filtration |
| $G_j$ | General function for reaction index $j$ |
| $h$ | heat transfer coefficient $\left(\frac{J}{s\cdot m^2\cdot K}\right)$ |
| $k_j$ | Reaction rate constant of reaction index $j$ |
| $k_p$ | Permeability $(m^2)$ |
| $K_{eq}$ | Equilibrium constant |
| $k_{m,i}$ | Mass transfer coefficient $\left(\frac{m}{s}\right)$ |
| $k_{p,s}(\mathtt{i},0)$ | Local clean substrate permeability of the slab `i` $(m^2)$ |
| $k_{p,s}(\mathtt{i},t)$ | Local substrate permeability of the slab `i` at time $t$ $(m^2)$ |
| $Kn$ | Particle Knudsen number |
| $L$ | Channel length $(m)$ |
| $M_i$ | Molecular weight of species $i$ $\left(\frac{g}{mol}\right)$ |
| $m_i$ | Mass of species $i$ |
| $m_{i,0}$ | Initial mass of species $i$ |
| $N_A$ | Avogadro's number $(mol^{-1})$ |
| $N_R$ | Interception parameter |
| $R$ | Universal gas constant $\left(\frac{Pa\cdot m^3}{K\cdot mol}\right)$ |
| $r_i$ | Reaction rate generating species $i$ $\left(\frac{mol}{s\cdot m^3}\right)$ |
| $S_p$ | Specific surface area $(m^{-1})$ |
| $s_{ij}$ | Stoichiometric coefficient of species $i$ in reaction index $j$ |
| $SCF$ | Stokes-Cunningham slip correction factor |
| $T$ | Temperature (K) |
| $v$ | Linear space velocity $\left(\frac{m}{s}\right)$ |
| $w_s(\mathtt{i})$ | Thickness of the slab `i` $(m)$ |
| $w_{ash}$ | Ash thickness $(m)$ |
| $w_{cake}$ | Cake thickness $(m)$ |
| $w_s$ | Wall thickness $(m)$ |
| $X_c$ | Conversion of carbon |
| S.V | Space velocity at standard conditions $(h^{-1})$ |

# 1

# Introduction

## 1.1 Context and problem description

The usage of diesel engines is trending positively for transportation vehicles such as cars, trucks and heavy-duty construction equipment. The reason is because of excellence in fuel efficiency compared to the engine´s torque output. Although, one drawback of diesel engines is the emission of undesired by-products after combustion of diesel fuel. This emission is not only harmful to human health but also the cause of environmental pollution. It is important to have a long-term solution. Meanwhile, other alternatives such as zero emission engines that use non-fossil fuel as energy sources (e.g. batteries and hydrogen fuel cells) are still on development phase. Therefore, in the aspect of sustainability, a diesel engine requires an exhaust aftertreatment system (EATS). Unlike gasoline engines' three-way catalyst (TWC) aftertreatment is not optimal for diesel engines, because of low temperatures and lean operating condition (excess in oxygen) in diesel engines that disfavor $NO_x$ reduction. Indeed, Not only improvements of the diesel engine and fuel are important but also EATS should be emphasized to develop an environmental sustainable solution.

The Exhaust composition from the gasoline engine and diesel engine are different. Combustion of diesel fuel forms diesel particulate matter (PM) which is also referred to as soot and the greater part of it consists of carbon. The PM may carry other compounds that can be harmful to human health. For this reason, understanding formation and removal of soot is of interest for researchers and automotive industry. Apart from soot, there are also other unwanted compounds in the exhaust such as nitrogen oxide ($NO_x$), hydrocarbons ($HC$) and carbon monoxide ($CO$). The acceptable emission of these compounds is regulated by the legislation. The emission limit in the European Union is defined by the European emission standards. The regulations have only become more stringent over the decades and they are expected to be even more demanding in the future [1]. This stresses and motivates the development of the EATS.

The engine operation (i.e. speed, fuel injected) depends largely on the driving condition which is unpredictable. This gives large variations in temperature and composition in the exhaust after engine[2]. Thus, the design of EATS is a challenging problem for the automotive industry. The current design of EATS consists of three main components which are Diesel Oxidation Catalyst (DOC), Diesel Particulate Filter (DPF) and Selective Catalytic Reduction (SCR), see Figure 1.1.

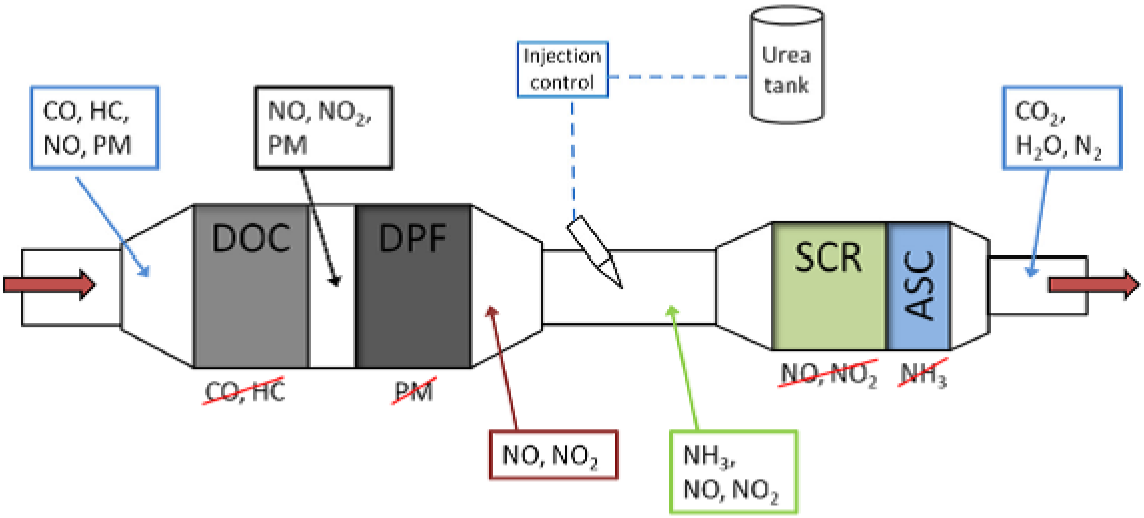

**Figure 1.1:** Schematic diagram of the arrangement of EATS downstream of diesel engines.

### Diesel Oxidation Catalyst

The DOC is a substrate monolith made of ceramic or metal material. The substrate is wash-coated with zeolites/alumina which contains noble metals, e.g. platinum (Pt). The main function of DOC is to oxidize $CO$, $HC$, and $NO$ compounds. The oxidation operates above 150°C depending on the composition of exhaust gas [3]. Moreover, very high temperatures is undersirable because of degradation of the catalytic material in DOC. The DOC is capable of converting $HC$ and $CO$ with an efficiency of 90-100%. DOC is also able to catalyze the oxidation reaction of nitrogen monoxide ($NO$) forming nitrogen dioxide ($NO_2$). The $NO_2$ is used as an oxidizer in DPF for soot oxidation.

### Diesel Particulate Filter

The main function of DPF is to trap soot through filtration. The soot is filtered by the porous filter media and the filter will eventually be saturated with soot. The soot particles in the filter's surface form cake layer which plugs and creates flow resistance in the filter. The saturation of substrate and the build-up of cake layer improve the filtration efficiency, but as a consequence causes a rise in the pressure drop, which leads to penalties in fuel consumption. Therefore, regeneration of the filter is necessary to increase the filter efficiency and fuel economy [4]. Furthermore, regeneration of the filter is achieved by oxidation of soot via reaction with oxygen ($O_2$) or $NO_2$.

### Selective Catalyst Reduction

SCR is usually at the rear of EATS and it is designed to reduce $NO_x$ to nitrogen $N_2$ using ammonia ($NH_3$). However, ammonia is in gas phase at ambient conditions. Hence, it is unpractical to store $NH_3$ onboard vehicles. One of the alternative solutions is to use Urea ($CO(NH_2)_2$) as a source of $NH_3$. Urea is in liquid phase at ambient conditions and is hydrolyzed to $NH_3$ at temperatures above 200°C [5]. Ammonia is also a hazardous compound and unreacted ammonia is treated by the Ammonia Slip Catalyst (ASC) at the rear end of the SCR.

### 1.1.1 Chemistry in the DPF

The non-catalytic soot oxidation by $O_2$, also known as active soot regeneration, occurs at temperatures above 550°C and 350°C if catalyzed by ($CeO_2$) [6]. The soot oxidation is an exothermic process and occurs relatively fast at high temperatures around 600°C. It is crucial to control the exhaust gas temperature and space velocity to avoid thermal runaway which degrades the filter material. For instance burning soot load of 10g/L in cordierite DPF gives an increase of ΔT=655 in temperature [7]. In general, soot loading in most filter systems does not exceed 5 g/L.
The soot oxidation reaction with $NO_2$, also known as passive soot regeneration, occurs at lower temperatures between 250-450°C [8–10]. It is critical to convert nitrogen $NO$ to $NO_2$ in order to maintain the passive soot oxidation. This is supported by the DOC (Pt-catalyst). The catalyst can be placed differently in the EATS to improve the passive regeneration. It is either only wash-coated in the DPF (CDPF) or non-catalyzed DPF with an upstream DOC or a combination of both. The commercial name of the second setup is known as Continuously Regenerating Trap ($CRT$©[1]). The latter mentioned setup is an extension of $CRT$©. The amount of catalyst is still the same but redistributed between the DOC and filter, which has the commercial name of Catalytic Continuously Regenerating Trap ($CCRT$©*1*). It is common that both active and passive regeneration are used in EATS for trucks depending on the circumstances [12]. The reaction condition of active regeneration is difficult to achieve naturally in urban area. Consequently, fuel injection is used to raise the temperature in order to initiate the active regeneration whenever passive regeneration is not sufficient.

### 1.1.2 Kinetic soot oxidation and DPF modeling

The fundamental approach in kinetic soot oxidation modeling is the global power-law model, which simplifies the soot oxidation into a single averaged reaction rate. The model is simple and practical to use for analysis of parameters for the rate-determining step, however, it lacks wider range validity. The solution to the issue is to account for significant elementary steps [13]. Among the proposed models is the mean-field kinetics and semi-global kinetics model. They are introduced in many different forms depending on underlying assumptions and desired features. However, their common feature accounts for the surface dependent mechanism by including surface coverage species in the reactions.

Soot oxidation is difficult to model due to ambiguity in soot composition and complex reaction mechanism [14, 15]. Kinetics of soot oxidation has been investigated by conducting experiments with synthetic soot (Printex-U) in a flow-through monolith under controlled conditions in order to find reliable kinetic data [16]. Printex-U is considered to be a good representative of diesel soot and it is highly referred in soot oxidation modeling [17]. It has been shown that a single rate expression is unable to describe the reaction rate of soot oxidation because the varying reaction order of carbon at low conversion. However, the reaction order at high conversion resembles the characteristics of shrinking core model [16].

---

[1] Trade name from Johnson Matthey [11]

In DPF modeling, it is critical to be able to estimate the soot loading and temperature during oxidation to develop regeneration strategies [18]. One common approach is utilizing the pressure drop to predict the soot loading. Pressure drop model is based on Darcy's law [19] and the total pressure drop is the sum of the contribution of pressure drop from DPF and soot cake. The pressure drop is coupled with a deep filtration model that accounts the distribution of soot between the substrate wall (deep filtration) and soot cake (filtration) [20]. The model is also able to predict soot collection efficiency which is one of the performance indicators of DPFs.

### 1.1.3 GT-POWER software

Computational aided simulations are widely used nowadays and it has become more popular since the advancement of computing capacity. Many software development companies (such as Gamma Technology, AVL, and SIMCAT) features EATS simulations as part of their software. GT-Power by Gamma Technology is utilized in the current work.

GT-POWER is widely used by major automotive companies to assess the design of combustion engines and EATS [16]. The key advantage of GT-POWER is the dedication to automotive applications and it is relatively easy to use the software. At the moment, simulation of aftertreatment system largely performs with one-dimensional (axial-direction) model and quasi-steady state assumption. The approach is efficient and relatively inexpensive in computation power. It has potentials to result in accurate and predictive models that for example can be used in scale-up operations. The quasi-steady state assumption assumes uniform flow in the cross section which does not always reflect reality. However, the result can be valuable when handled with caution.

## 1.2 Aims and objectives

The main purpose of the thesis is to develop detailed soot oxidation kinetic models and applied in a DPF model. The implementation of the models in GT-POWER is emphasized in this work. Other significant models such as pressure drop and $NO$ oxidation are included in the development of DPF model. Part of the development involves data analysis such as kinetic parameter estimation using Arrhenius equation to determine parameters of limiting step for the detailed kinetic mechanism. Also, utilize different analysis on DPF data to calibrate the pressure drop model and deep filtration model. Furthermore, investigate the models' limitations and if the models are physically meaningful. Investigation on the simulation performance is also required. The results shall highlight the important aspects of soot oxidation in DPF modeling, which may benefit the development of EATS modeling and regeneration control strategies.

## 1.3 Work overview

The reaction kinetics model is developed and optimized for each set of experimental data. The overview work flowchart is summarized in Figure 1.2.

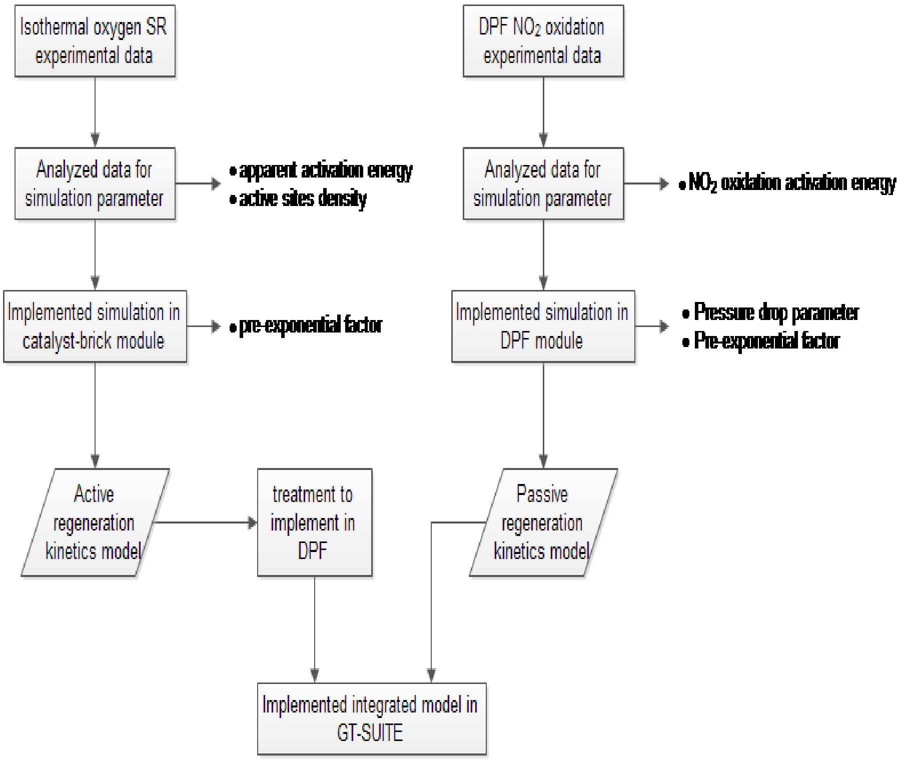

**Figure 1.2:** Overview of the work process as flowchart in current work.

## 1.4 Contributions to the current work

Detailed kinetics of soot oxidation and proposed mechanisms are described in Per-Anders Carlsson's work [15]. Experimental observations and parameter analysis were made in another work by Carolin Wang-Hansen et al. [16]. An additional work dedicated to parameter analysis of soot oxidation [21]. Regarding the reaction order of carbon is represented by shrinking core models [22]. Comprehensive work about soot oxidation and pressure drop in DPF by Schejbal et al. [23]. The pressure drop model in DPF is covered in a publication by Konstantopolous et al. [19]. Konstantopolous has also contributed to the deep filtration modeling in DPF [20].

# 2

# Kinetic modeling of soot oxidation in DPF

This chapter defines the frame of reference and relevant theories for the current work. This includes an overview of the chemistry in DPF and various approaches in kinetic modeling of soot oxidation. Also, pressure drop model as well as deep filtration model in DPF. Finally, a review of simulation theories is covered and this includes the governing equations and numerical solvers that are utilized in GT-POWER.

## 2.1 Chemical reactions in DPF

In fact, DPF is more or less a reactor with filtration properties where the main reactions are involved with soot oxidation. soot oxidation by $O_2$ is effective at high temperature (550°C) reaction condition, while oxidation using $NO_2$ occurs at lower temperature but requires catalysts to have adequate concentration of $NO_2$. Soot is simplified to a solid carbon element, but in reality, it is a distribution of different carbon compounds. For simplicity, the stoichiometry is assumed balanced when performing active or passive regeneration, see reactions (2.1), (2.2), (2.3) and (2.4).

**Active regeneration**

$$C(s) + O_2(g) \rightarrow CO_2(g) \tag{2.1}$$

$$C(s) + 0.5O_2(g) \rightarrow CO(g) \tag{2.2}$$

**Passive regeneration**

$$C(s) + NO_2(g) \rightarrow CO(g) + NO(g) \tag{2.3}$$

$$C(s) + 2NO_2(g) \rightarrow CO_2(g) + 2NO(g) \tag{2.4}$$

$NO/NO_2$ is formed during diesel fuel combustion in engine at very high temperatures (above 1100 ) which is known as Zeldovich mechanism [24].

$$0.5O_2 + N_2 \rightarrow NO \tag{2.5}$$

$NO$ can also react with excess oxygen and forms $NO_2$ in reaction (2.6). The oxidizer $NO_2$ must be maintained at sufficient levels in order to efficiently perform passive regeneration in the DPF. Therefore, it is common to use catalyst in DPF (CDPF). It enables conversion of $NO$ to $NO_2$ as DOC and increases the $NO{:}NO_2$ ratio. The Oxidation reactions with $NO_2$ (e.g. hydrocarbons, $CO$ and soot) produces $NO$ rather than $N_2$ due to thermodynamic limitation, since more heat is required to form $N_2$.

$NO$ oxidation is a reversible reaction and it is limited by thermodynamic equilibrium. The equilibrium depends on temperature and concentrations [25]. Also, space velocity (i.e. residence time) determines the operating points of NO oxidation within the equilibrium.

**NO oxidation**

$$NO(g) + 0.5O_2(g) \leftrightarrow NO_2(g) \tag{2.6}$$

The oxidation of $CO$ is catalyzed by platinum to react with either $O_2$ or $NO_2$ forming $CO_2$. $NO$ is formed if $NO_2$ is used as an oxidizer, see reactions (2.7) and (2.8). Therefore, the product stream out of CDPF or DOC is primarily $CO_2$. The concentration of $CO_2$ in diesel engine exhaust (combustion at lean condition) is typically 6-7% and 2-3 order of magnitude higher relative to $CO$ or $NO_x$.

**CO oxidation**

$$CO(g) + 0.5O_2(g) \rightarrow CO_2(g) \tag{2.7}$$

$$CO(g) + NO_2(g) \rightarrow CO_2(g) + NO(g) \tag{2.8}$$

Hydrocarbons ($HC$) in the exhaust is a group of compounds consisting of hydrogen and carbons. The actual composition of $HC$ is usually unknown and depends on fuel type, combustion characteristics, lubrication oil, cooling temperature [26]. A mixture of hydrocarbon compounds is usually used to represent $HC$. Similarly to soot, $HC$ can be oxidized by both $NO_2$ or $O_2$ to form $CO_2$. $HC$ inlet to the DPF depends on $HC$ conversion from the upstream DOC. The stoichiometry in the reactions (2.9) and (2.10) are not balanced because of the uncertain definition of $HC$.

**HC oxidation**

$$HC(g) + O_2(g) \rightarrow CO_2(g) + H_2O(g) \tag{2.9}$$

$$HC(g) + NO_2(g) \rightarrow CO_2(g) + H_2O(g) + NO \tag{2.10}$$

## 2.2 Soot oxidation kinetic modeling

### 2.2.1 Global power-law model

In kinetic modeling of soot oxidation, it is common to use global power-law model to describe the overall reaction rate of soot oxidation [16, 21, 27]. The model assumes a single reaction step. where soot is represented as carbon $C(s)$ reacting with gas phase $O_2$ which is expressed:

$$rate = km_{C,0}(1 - X_C)^{\eta_C}[O_2]^n \tag{2.11}$$

$m_{C,0}(1 - X_C)$ is derived from [C]=[$C_0$](1 − $X_C$), where [$C_0$] is the initial carbon concentration. The reaction order of oxygen $n$ is typically 0.5 to 1 for $CO$ and $CO_2$ [13]. The temperature dependence is accounted by Arrhenius rate constant k. It is defined by Arrhenius equation:

$$k = A \cdot exp(\frac{-E_a}{RT}) \tag{2.12}$$

Where $E_a$ is the activation energy, $R$ is the gas constant, $T$ is the variable temperature and $A$ is the pre-exponential factor. The Arrhenius constant can also be expressed as a linear function of temperature.

$$ln(k) = -\frac{E_a}{RT} + ln(A) \tag{2.13}$$

Note the natural logarithm of Arrhenius constant $ln(k)$ can also be the natural logarithm of the observed rate $ln(rate)$. If that is the case the pre-exponential factor $A$ is lumped with some constants (e.g. concentration of oxygen $[O_2]^n$ and initial carbon concentration $[C_0]$).

The soot oxidation by $NO_2$ is similar to equation (2.11) with following rate expression:

$$rate = km_{C,0}(1 - X_C)^{\eta_C}[NO_2]^m \tag{2.14}$$

The rate expression is a function of existing carbon mass or concentration which is defined as $m_{C,0}(1-X_C)^{\eta_C}$, where $m_{C,0}$ is the initial carbon mass, $X_C$ is the conversion with reaction order $\eta_C$. The reaction order in respect of $NO_2$ is $m$. $k$ is the rate constant from Arrhenius equation (2.12).

The advantage with global kinetics model is simplicity and it is able to estimate parameters from experiments. However, relying on one single rate expression is not sufficient to fully describe soot oxidation in details. Due to the change in carbon and oxygen reaction order (0.6-0.9 and 0.85-1.00 respectively) over time [21]. In addition, activation energy (approximately 20kJ/mol) decreases with conversion of soot [16].

### 2.2.2 Shrinking core model

The shrinking core model (see Equation 2.15) is usually used in the gas-solid reaction. It assumes that the reaction rate depends on the available surface area. Moreover, the solid particle is assumed to be smaller as the conversion increases.

$$S_p = S_{p,0}(1 - X_c)^{\eta_c} \tag{2.15}$$

The order $\eta_C$ is usually assumed to be 2/3. This value is derived from mono-dispersed spherical particles [21]. For soot oxidation, the value of 0.7 is experimentally observed in the conversion range of 0.25-0.90 [16, 28]. Studies of surface area by the method of Brunauer–Emmett–Teller (BET) by Ishiguro et al., Stanmore et al., Wang-Hansen et al. and Lussow et al. showed that the surface area increases with conversion and remains constant at high conversion [10, 16, 29, 30].

Tighe et al. reviewed on the morphology of soot and suggested that soot particles should be considered as the ensemble of individual spherules which reacts independently [31]. This explanation clarifies the problem since an ensemble of many tiny spherules is equivalent to one 'large porous particle'.

Zhdanov et al. investigated on different particle geometry and size distribution function [22]. He also suggested soot particles should be modeled as disks. The disk assumption combined with particle size distribution was considered to perform equally well compared to spherical particles.

Stanmore et al. show that the effectiveness factor is almost unity in all ranges of conversion [10]. However, the specific surface area changes greatly with the conversion. Transmission electron microscopy (TEM) observation of soot during the oxidation by Jung et al. report that individual spherules shrink uniformly [32]. Which imply that the total amount of spherules is conserved during the soot oxidation. Hence, the increase in surface area might come from the growth of porous channels.

These observations imply that the morphology changes during oxidation [31]. One hypothesis is that; at low conversion, the ensemble of soot spherules is selectively oxidized and breaks down into smaller ensembles (or can be considered as pore growth inside the 'large porous particle'). Liberating more surface area for the system [31]. This mechanism stops once the ensembles of the particle are relatively small. Then, the reaction becomes surface reaction controlled and spherules shrink uniformly.

### 2.2.3 Semi-global kinetics model

Semi-global kinetics model is an extension of the global kinetic model aimed to improve the selectivity of $CO/CO_2$ and oxygen dependency. The reaction is expanded into lumped reaction steps including formation of surface oxide complex $CO_{ads}$ and reacts further with gas phase oxygen. Haynes et al. suggests following reaction scheme [33]:

$$C(s) + O_2 \rightarrow CO_{ads} \tag{2.16}$$

$$CO_{ads} \rightarrow CO(g) \tag{2.17}$$

$$CO_{ads} + O_2(g) \rightarrow CO_2(g) \tag{2.18}$$

$C_s$ is a free active site on the carbon surface. The reaction step (2.16) suggests that oxygen interact with the surface complex. which imply destabilization of the metastable complex due to oxygen's attack on site resulting in desorption of $CO/CO_2$ [34]. Such reactions are observed for $CO_2$ in experiments where carbon surface complex with $^{18}$O reacting with gas phase $^{18}$O forming carbon dioxide with two isotopes [35].

### 2.2.4 Langmuir-Hinshelwood based model

Langmuir-Hinshelwood model describes adsorption of oxygen onto a vacant site $s$ of the surface of carbons as an elementary step in the oxidation reaction [27, 36]. Moreover, there are different assumptions available of gas adsorption on solid. It is either non-dissociative or dissociative.

If the adsorption is assumed as non-dissociative with the corresponding expression:

$$O_2 + 2s \rightarrow 2O_{ads} \tag{2.19}$$

While dissociative adsorption has the corresponding expression:

$$O_2 + s \rightarrow (O_2)_{ads} \tag{2.20}$$

The oxygen $O_2$ dissociates into two $O$ molecules and occupies two vacant carbon sites. The adsorbed oxygen may react further with carbon and desorbs as gaseous $CO$ or $CO_2$. Remark: the stoichiometry of the reactions below is not balanced.

$$C(s) + O_{ads} \rightarrow CO(g)/CO_2(g) \tag{2.21}$$

The overall rate laws for (2.19) and (2.21) is expressed as:

$$rate = \frac{k_1 k_2 [O_2]^n}{k_1 [O_2]^n + k_2} \tag{2.22}$$

The measured activation energy for adsorption is lower than activation energy of desorption in soot combustion with the inequality $E_{a,des} > E_{a,ads}$ [37]. Langmuir-Hinshelwood based models are unable to predict the global intrinsic reaction order at low temperatures (below 1000K). Although, with inverted inequality of activation energies Langmuir-Hinshelwood model is able to cover low temperatures [38]. However, this makes the model unphysical and not feasible.

### 2.2.5 Eley-Rideal based model

Another type of surface reaction models similar to Langmuir-Hinshelwood model is Eley-Rideal model [39]. The difference between these models is the assumption of the reaction mechanism, where Eley-Rideal assumes single adsorbed molecule reacting with gas phase proceeding to desorption. While Langmuir assumes two adsorbed molecules reacts and desorbs, see Figure 2.1.

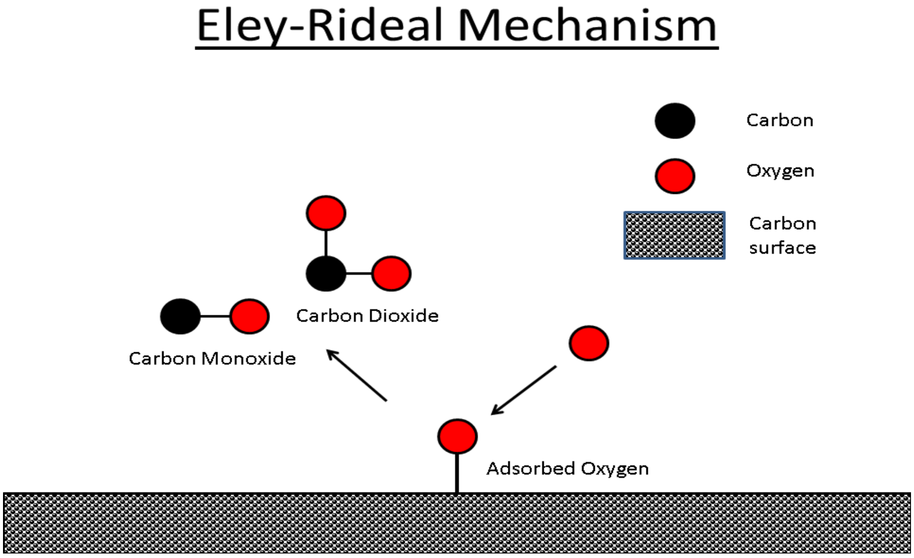

**Figure 2.1:** Illustration of Eley-Rideal's mechanism where gas phase oxygen interacts with adsorbed oxygen and carbon surface forming $CO$ and $CO_2$

### 2.2.6 Mean-field kinetics model

Previous models are unable to interpret soot oxidation in detailed at low conversion. A better solution is to use mean-field kinetics in order to add details features in soot oxidation modeling [15]. The mean-field kinetics model considers active sites on a heterogeneous surface with various activation energy according to theories of activated adsorption-desorption [40].

The reaction (2.16) is expanded to account for oxygen adsorption to active site $s$ on carbon surface as in (2.19) or (2.20). The adsorbed oxygen may react with elemental carbon atom $C(s)$ to form adsorbed surface oxide complex $CO_{ads}$ [41]:

$$C(s) + O_{ads} \rightarrow CO_{ads} \tag{2.23}$$

Reaction steps (2.19)/(2.20) and (2.23) will be the basis of mean-field models. Numerous of these types models were proposed with elementary steps in previous work of detailed modeling of carbon oxidation [15]. Two of these models are:

Model 1. Reactive oxygen species

$$0.5O_2(g) + O^*_{ads} + C(s) \rightarrow CO(g) + O_{ads} \tag{2.24}$$

$$0.5O_2(g) + O^*_{ads} + C(s) \rightarrow CO_2(g) + s \tag{2.25}$$

$$O_2(g) + 2s \rightarrow +2O_{ads} \tag{2.26}$$

$$O_{ads} + C(s) \rightarrow CO_{ads} \tag{2.27}$$

$$0.5O_2(g) + CO_{ads} \rightarrow CO(g) + O_{ads} \tag{2.28}$$

$$O_2(g) + CO_{ads} \rightarrow CO_2(g) + O_{ads} \tag{2.29}$$

Model 2. Reactive carbon species

$$O_2(g) + 2s^* \rightarrow 2O^*_{ads} \tag{2.30}$$

$$0.5\,\mathrm{O_2(g)} + \mathrm{C^*(s)} \xrightarrow{\mathrm{O_{ads}}^*} \mathrm{CO(g)} \tag{2.31}$$

$$\mathrm{O_2(g)} + \mathrm{C^*(s)} \xrightarrow{\mathrm{O_{ads}}^*} \mathrm{CO_2(g)} \tag{2.32}$$

$$O_2(g) + 2s \rightarrow 2O_{ads} \tag{2.33}$$

$$0.5\,\mathrm{O_2(g)} + \mathrm{C(s)} \xrightarrow{\mathrm{O_{ads}}} \mathrm{CO(g)} \tag{2.34}$$

$$\mathrm{O_2(g)} + \mathrm{C(s)} \xrightarrow{\mathrm{O_{ads}}} \mathrm{CO_2(g)} \tag{2.35}$$

The first model assumes that an additional reactive oxygen species $O^*_{ads}$ are present (in limited amounts), these species may represent adsorbed OH, water or other functional groups that affect the reactivity of the carbon. Reactions (2.24) and (2.25) are considered to be very fast and have a different activation energy compared to the overall activation energy. Reaction (2.26) and (2.27) are the initial rate-determining step, because of lower initial coverage that increases with conversion (or time) when new surface oxide complexes forms. The surface species reacts further through reactions (2.28) and (2.29) to form $CO$ and $CO_2$. The schematic reaction mechanism is illustrated in Figure 2.2.

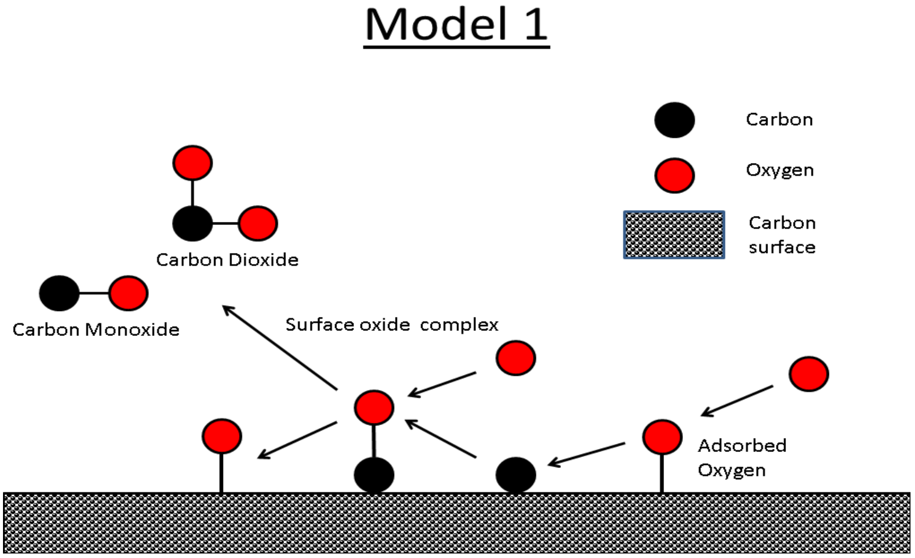

**Figure 2.2:** A representative illustration of the proposed mechanism in model 1.

The corresponding rate laws can be expressed as following (also note that the active sites are lumped in the Arrhenius constant):

$$\frac{d\theta_{O^*_{ads}}}{dt} = -k_1[C]^{nc}[O_2]^n\theta_{O^*_{ads}} - k_2[C]^{nc}[O_2]^n\theta_{O^*_{ads}} \tag{2.36}$$

$$\frac{d\theta_{O_{ads}}}{dt} = (k_3(1-\theta_{O_{ads}}-\theta_{CO_{ads}})^2 + k_1[C]^{nc}\theta_{O^*_{ads}} + k_5\theta_{CO_{ads}} + k_6\theta_{CO_{ads}})[O_2]^n - k_4[C]^{nc}\theta_{O_{ads}} \tag{2.37}$$

$$\frac{d\theta_{CO_{ads}}}{dt} = k_4[C]^{nc}\theta_{O_{ads}} - k_5[O_2]^n\theta_{CO_{ads}} - k_6[O_2]^n\theta_{CO_{ads}} \tag{2.38}$$

$$\frac{dC(s)}{dt} = -k_4[C]^{nc}\theta_{O_{ads}} \tag{2.39}$$

$$\frac{dCO(g)}{dt} = k_1[C]^{nc}[O_2]^n\theta_{O^*_{ads}} + k_5[O_2]^n\theta_{CO_{ads}} \tag{2.40}$$

$$\frac{dCO_2(g)}{dt} = k_2[C]^{nc}[O_2]^n\theta_{O^*_{ads}} + k_6[O_2]^n\theta_{CO_{ads}} \tag{2.41}$$

The second model suggests the presence of reactive carbon species $C^*$ (in limited amounts). It can be interpreted as soot surface with functional groups with different thermal stability such as carboxylic acid, lactone, or carboxylic anhydride [9]. Carbon with these functional groups has a relatively higher reactivity. In addition, the model suggests two types of carbon sites describing the heterogeneity of active site density. Many studies suggests existence of more than one type of active sites [10, 27, 41, 42]. The secondary site here represents an additional type of carbon sites $s^*$ which belong to $C^*$. In other words, there are two sets of reactions working independently to produce gaseous $CO$ and $CO_2$. One of the set is very fast (2.31) and (2.32) while the other is relatively slower (2.34) and (2.35). The rate-determining step in this model is reactions (2.30) and (2.33). This model uses lumped reactions compared to the first model. See Figure 2.3.

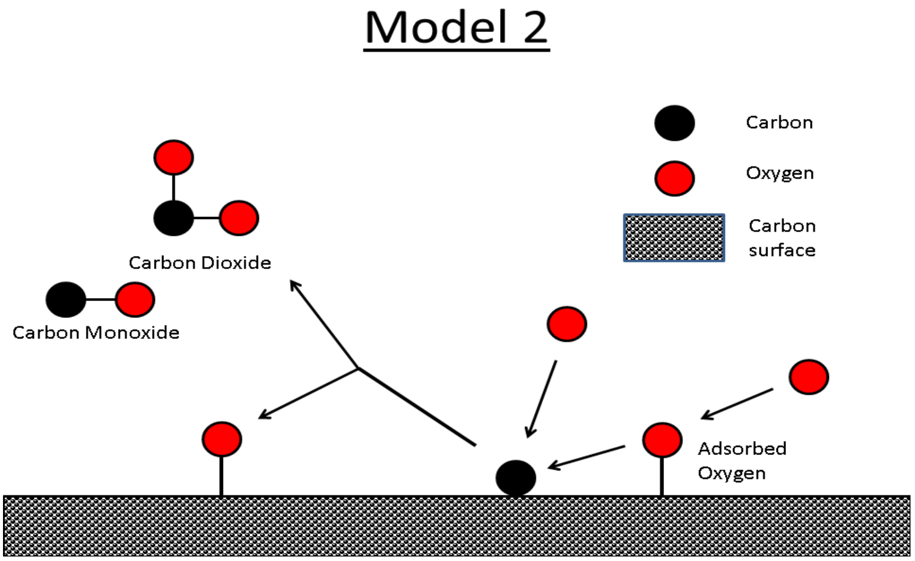

**Figure 2.3:** Model 2 is a lumped version of model 1 with similar assumption about existence of reactive species.

The corresponding rate laws expressions are:

$$\frac{d\theta_{O_{ads,s*}}}{dt} = k_1[O_2]^n(1-\theta_{O_{ads,s*}})^2 \tag{2.42}$$

$$\frac{d\theta_{O_{ads}}}{dt} = k_1[O_2]^n(1-\theta_{O_{ads,}})^2 \tag{2.43}$$

$$\frac{dC^*(s)}{dt} = (-k_2[O_2]^n\theta_{O_{ads,s*}} - k_3[O_2]^n\theta_{O_{ads,s*}})[C^*]^{n_C} \tag{2.44}$$

$$\frac{dC(s)}{dt} = (-k_5[O_2]^n\theta_{O_{ads}} - k_6[O_2]^n\theta_{O_{ads}})[C]^{n_C} \tag{2.45}$$

$$\frac{dCO(g)}{dt} = (k_2[O_2]^n\theta_{O_{ads}} + k_5[O_2]^n\theta_{O_{ads}})[C]^{n_C} \tag{2.46}$$

$$\frac{dCO_2(g)}{dt} = (k_3[O_2]^n\theta_{O_{ads,s*}} + k_6[O_2]^n\theta_{O_{ads}})[C]^{n_C} \tag{2.47}$$

The above-mentioned models are similar to the multi-population kinetics model, where three soot populations were found and each soot population has its own distinguishable activation energy [43]. The mean-field kinetic models tend to be empirical expressions. These models have more degrees of freedom compared to global kinetics. Therefore, it is easier to obtain a good fit due to the larger number of adjustable parameters. However, more observations are needed to make these models reasonable and practical to apply.

### 2.2.7 $NO$ oxidation

$NO$ oxidation has an important role in CDPF's performances because of passive regeneration depends on $NO$ and $NO_2$ concentrations. The platinum catalyst promotes conversion from $NO$ to $NO_2$ ($NO(g) + 0.5O_2(g) \leftrightarrow NO_2(g)$). The forward and backward reaction can be expressed as an equilibrium constant [44].

$$K_{eq} = \frac{k_{forward}}{k_{backward}} = \frac{[NO_2]}{[O_2]^{0.5}[NO]} \tag{2.48}$$

Or rewritten as:

$$\frac{NO_2}{NO_x} = \frac{K_{eq}[O_2]^{0.5}}{1 + K_{eq}[O_2]^{0.5}} \tag{2.49}$$

The equilibrium constant is a function of Gibbs free energy and temperature

$$K_{eq} = exp\left(\frac{-\Delta G}{RT}\right) \tag{2.50}$$

where$\Delta G$ is Gibbs energy (J/mol) described by Gibbs linear correlation with enthalpy ΔH and entropy ΔS change which is a function of temperature (K):

$$\Delta G = \Delta H - T\Delta S = -58353 + 76.46T \tag{2.51}$$

Finally using equation 2.48 the rate expression can be written as:

$$rate = k_{forward}[O_2]^{0.5}[NO] - \frac{k_{forward}[NO_2]}{K_{eq}} \tag{2.52}$$

$NO$ oxidation is a heterogeneous catalytic reaction that involves more complicated reaction steps for adsorption and desorption. However, the kinetics above are simplified to gas phase equilibrium reaction.

## 2.3 Simulation Governing Equations

GT-POWER aftertreatment application assumes quasi-steady (QS) approximation by default. It assumes that the system is in its steady-state (e.g. gas pressure, temperature, and velocity) at every time step and the change in each time step is small [45]. These conditions are satisfied in most of the aftertreatment applications because of short residence time compared to another time scale of interest [23, 46]. As a result, material (substantial) derivatives are simplified to spatial derivative and the governing equations are easier to be constructed, solved and simulated.

### 2.3.1 Flow-through Reactor Governing Equations

**Mass balance**

The flow-through monolith is effectively a reactor with wash-coat. 1D assumption simplifies the system by only allowing gradients in axial direction [45]. The mass balance has to be solved in the gas phase and in the wash-coat. They are shown in equation (2.53) and (2.54) respectively.

$$\frac{dC_i}{dt} = -\frac{d(vC_i)}{dz} + \frac{k_{m,i}S_p}{\epsilon}(C_i^s - C_i) \tag{2.53}$$

$$\frac{dC_i^s}{dt} = -\frac{k_{m,i}S_p}{(1-\epsilon)}(C_i^s - C_i) + s_{ij}r_i \tag{2.54}$$

Where $C_i$ and $C_i^s$ is the concentration for species $i$ in the gas and in the wash-coat respectively. $\epsilon$ is the reactor void fraction. $v$ is the linear velocity of the gas. $k_m$ is the mass transfer coefficient calculated by binary diffusion coefficients from Fuller correlation [47].

$$k_{m,i} = Sh\frac{D_{e,i}}{D_h} \tag{2.55}$$

$De, i$ is the effective diffusion coefficient calculated with following equation:

$$\frac{1}{D_{e,i}} = \frac{\tau}{\epsilon_w}\left(\frac{1}{D_i} + \frac{1}{D_{Knudsen,i}}\right) \tag{2.56}$$

$S_p$ is the specific surface area of the reactor. $s_{ij}$ denotes the stoichiometric coefficient of species $i$ in reaction $j$ while $r_i$ denotes the rate of production/consumption of species $i$. The quasi-steady state assumption also eliminates accumulation terms on the left-hand side. Wash-coat layer was not applied in this thesis because soot was implemented as stored carbon on the substrate layer. Wang-Hansen et al. show that the soot oxidation in the monolith is kinetic-limited [16]. Therefore, equation (2.53) and (2.54) is reduced to:

$$\frac{\epsilon v}{(1-\epsilon)}\frac{dC_i}{dz} = (s_{ij}r_i) \tag{2.57}$$

It can also be written in form of mass fraction as:

$$\epsilon\rho_g v\frac{d\omega_i}{dz} = \frac{M_i}{1000}s_{ij}r_i \tag{2.58}$$

Where $M_i$ denotes the molecular weight of species $i$ and $\omega_i$ is the mass fraction for species $i$ and $\rho_g$ is the gas density.

### Momentum balance

The continuity equation of conserved quantities is solved before solving the momentum balance.

$$\frac{\partial}{\partial z}(\rho_g v) = 0 \tag{2.59}$$

and the momentum balance is as following:

$$\epsilon\frac{\partial P}{\partial z} + \epsilon\rho_g v\frac{\partial v}{\partial z} = -\frac{1}{2}S_p f \rho_g v^2 \tag{2.60}$$

Where $P$ is the pressure and $f$ is the friction coefficient. If the change in gas density is negligible, then the second term in Equation 2.60 is eliminated.

### Reaction and coverage balance

The reaction rate for each species derived from the interested model has the general form of:

$$r_i = \sum_{j}^{\substack{\text{reaction involved} \\ \text{with species i}}} A_j exp(-\frac{E_{a_j}}{RT}) \cdot [O_2]^\eta \cdot f_j(\theta) \cdot G_j \tag{2.61}$$

Where $f_j(\theta)$ is the coverage function for reaction $j$, $\eta$ is species order of oxygen and $G_j$ is the additional function for reaction $j$.

The governing equation of active site balance is:

$$\begin{gathered} \frac{d\theta_i}{dt} = \sum_i \frac{\sigma_{ki} r_i}{\lambda_k} \\ \sum_i \theta_i = 1 \end{gathered} \tag{2.62}$$

Where $\theta_i$ denotes the coverage occupied by species $i$ on the active site, $\lambda_k$ denotes the active site density of site k and $\sigma_{ki}$ denotes stoichiometric coefficient of reactant species $i$ to active site $k$.

### Solid phase energy balance

$$\rho_s c_{p,s}\frac{\partial T_s}{\partial t} = \frac{\partial}{\partial z}((1-\epsilon)\kappa_{T,s}\frac{\partial T_s}{\partial z}) + hS(T_g - T_s) + h_{ext}S_{ext}(T_{ext} - T_s) - \sum_{j}^{rxn} \Delta H_j r_j \tag{2.63}$$

Where $\rho_s c_{p,s}$ is the effective heat capacity of the substrate, $T_g$ is the gas temperature and $T_s$ is the temperature of the substrate, which is assumed to be equal to the temperature of the gas at the gas-solid boundary. $\kappa_{T,s}$ is the thermal conductivity of the substrate, $h$ is the heat transfer coefficient between gas and substrate, $S$ is the surface area, $h_{ext}$ is the external heat transfer coefficient, $S_{ext}$ and $T_{ext}$ is the external surface area exposed to the external source and the external temperature. $\Delta H_j$ is the enthalpy of reaction index $j$, $r_j$

is the reaction rate for reaction index $j$. The first term on the right-hand side accounts for the heat conduction in the substrate to an adjacent unit. The second and third term accounts for thermal convection with bulk gas and external source respectively. The final term accounts for the heat generated or consumed by the reaction.

**Gas phase energy balance**

$$\epsilon v \rho_g C_{p,g} \frac{\partial T_g}{\partial z} = hS(T_s - T_g) \tag{2.64}$$

Where $C_{p,g}$ is the heat capacity of the gas. Since reaction is assumed to occur only on the active sites, the generation/consumption of heat by reaction in gas-phase is omitted.

### 2.3.2 DPF governing equation

GT-POWER allows 1-D simulation of the DPF. The DPF is discretized along the axial direction. However, the DPF is a wall-flow monolith, the radial wall flux is an important property for this system. The soot cake layer and substrate are discretized to improve the accuracy of the wall flux calculation.

**Mass balance**

$$\frac{\partial \rho_g v D_h^2}{\partial z} = (-1)^n 4 D_h \rho_s v_s \tag{2.65}$$

The change in mass flux along the axial direction is the result of mass flux to the wall direction. $\rho_s v_s$ is the mass flux. $D_h$ denotes the hydraulic diameter which defined for square channel:

$$D_h \equiv \frac{4\epsilon}{S_p}$$

**Component balance**

$$\frac{\partial \rho_g v D_h^2 \omega_i}{\partial z} = (-1)^n 4 D_h \rho_s v_s \omega_i^s - (-1)^n 4 D_h \rho_g k_c (\omega_i - \omega_i^s) \tag{2.66}$$

Where $\omega_i$ and $\omega_i^s$ are the mass fraction of interested species $i$ in gas phase and in the wall respectively. $k_c$ denotes the mass transfer coefficient. The first term on the right-hand side represents species transport by convection while the second term represents diffusion with driving force of $(\omega_i - \omega_i^s)$. $n$ is an odd number for inlet channel and even number for outlet channel.

The radial wall flow is modeled in the soot cake and substrate layer, where all the species are solved in a concentration gradient. if diffusion is insignificant the second term in equation (2.67) is eliminated. This equation is important because it governs how much reactant species that will reach the soot layer in each sub-volume.

$$\rho_g v_s \frac{\partial \omega_i^s}{\partial r} - \rho_s D_{e,i} \frac{\partial^2 \omega_i^s}{\partial r^2} = M_i \sum_i s_{ij} r_i \tag{2.67}$$

Where $D_{e,i}$ denotes the effective diffusion coefficient of species $i$ in the solid and $\rho_s$ is the density of the soot in the wall.

Diffusion modeling is based on work published by Mladenov et al. and it accounts for both inlet and outlet channels, soot cake layer and wall diffusion [48]. The model solves for concentration gradients for all species $i$.

### Momentum balance

The momentum governing equation from the catalyst brick is also used in the DPF, equation (2.60). However, the equation is rewritten with Ergun equation for the porous medium.

$$\begin{aligned} Re &= \frac{D_h \rho_g v}{\mu} && \text{Reynolds Number} \\ \alpha = f \cdot Re &= \frac{1-\epsilon}{2\epsilon^2}(150 + 1.75Re) && \text{Ergun Equation} \end{aligned}$$

Where $\mu$ denotes the dynamic viscosity. Equation (2.60) yields:

$$\frac{\partial (P + \rho_g v^2)}{dz} = -\frac{\alpha \mu v}{D_h^2} \tag{2.68}$$

The pressure $P$ in DPF is solved externally by the pressure drop model presented in Section (2.3.3.2) based on Darcy's law.

### Gas phase energy balance

$$C_{p,g} \frac{\partial D_h^2 \rho_g v T_g}{\partial z} = 4 D_h h (T_s - T_g) + 4 D_h \rho_s v_s C_{p,g} T_s \tag{2.69}$$

Where $C_{p,g}$ denotes specific heat capacity of the gas and $T_s$ is the temperature of the soot. The first term on the left-hand side represents convective heat flux transport between the gas and wall with the driving force of $(T_s - T_g)$. The second term represented the advection heat transport from mass flux.

**Soot layer energy balance**

$$\rho_s C_{p,s} \frac{\partial T_s}{\partial t} = \kappa_{T,s} \frac{\partial^2 T_s}{\partial z^2} - 4D_h h(T_s - T_g) - 4D_h \rho_s v_s C_{p,g} T_s + \Delta H_s r_s \tag{2.70}$$

**Soot mass balance**

$$\frac{dm_{C,s}}{dt} = V M_C r_C + \text{source term} \tag{2.71}$$

Where $m_{C,s}$ denotes the total soot mass in the DPF and $r_C$ denotes the total soot consumption rate in the unit of $mol/(s \cdot m^3)$.

### 2.3.3 External models in DPF

In DPF modeling, there are mainly three interconnected properties that are concerned 1) Regeneration of the filter, 2) The pressure drop due to flow resistance on walls and due to accumulated soot, 3) Soot deposition in the substrate. These properties are modeled by external model and appear as source terms in the governing equation.

#### 2.3.3.1 Deep filtration model

Deep filtration model is used to track the soot mass accumulation (collection efficiency) inside the substrate. This is important because the properties of the substrate can change with the amount of soot it stores. The model is formulated in a publication by kladopoulou et al. which assumes the main filtration of soot is a combination of deposition mechanisms; interception and Brownian diffusion from theories about aerosol particle deposition [20]. The first mechanism suggests particles moves along the flow field and intercepts with the filter medium. The second mechanism is filtration of particles due to random motion caused by collisions with other suspended particles. Particles are assumed to be collected by so-called spherical unit collectors in a number of discretized segments (slabs) of the substrate. The collection efficiency of DPF is defined by the contributions from the above-mentioned mechanisms. The number of equations is too many to be included here, see appendix A.1 for full sets of equations. In summary, the model consists of 9 equations in total. The equations describes the local wall porosity $\epsilon(\mathtt{i}, t)$, unit collector diameter $d_c(\mathtt{i}, t)$, collection efficiency at each slab. The calculated values are used to estimate the local loaded filter permeability $k_{p,s}(\mathtt{i}, t)$ (see Appendix A.2).

$$\frac{k_{p,s}(\mathtt{i}, t)}{k_{p,s}(\mathtt{i}, 0)} = \left( \frac{d_c(\mathtt{i}, t)}{d_c(\mathtt{i}, 0)} \right)^2 \frac{f(\epsilon(\mathtt{i}, t))}{f(\epsilon(\mathtt{i}, 0))} \tag{2.72}$$

The inlet soot mass is divided between the substrate (deep filtration) and soot cake (filtration). It is determined by the partition coefficient $\Phi$, which is the fraction of inlet soot mass that is deposited on soot cake. It is a function of time which is 0 at time=0 and transitions to 1 once the unit collector is full. (when unit collector diameter in the first slab $d_c(1, t)$ is equal to ($\Psi b$)), see equation (2.73).

$$\Phi = \left[ \frac{d_c^2(1,t) - d_c^2(\mathtt{i},0)}{(\Psi b)^2 - d_c^2(\mathtt{i},0)} \right] \tag{2.73}$$

Where the unit collector diameter is given by filter porosity and pore diameter: $d_c(\mathtt{i},0) = \frac{3(1-\epsilon_s(\mathtt{i},0))}{2\epsilon_s(\mathtt{i},0)} d_{pore}$. The percolation constant $\Psi$ and b is the unit cell diameter defined as $b = d_c(\mathtt{i},0) / \left(1 - \epsilon_s(\mathtt{i},0)\right)^{\frac{1}{3}}$. Therefore, increasing the percolation number means lower soot mass distributed to the substrate and vice versa.

#### 2.3.3.2 Pressure drop model

The Pressure drop model is based on previous work by Konstandopoulos et al. It assumes pressure drop to be the sum of all pressure drop sources [19]. The main pressure drop sources in DPF is friction in filter wall $\Delta P_5$, pressure losses due to the deposited soot cake layer $\Delta P_3$, losses due to inlet $\Delta P_2$ and outlet $\Delta P_6$ channels. There are also other pressure drop sources, such as contraction $\Delta P_1$ and expansion $\Delta P_7$ and ash loading $\Delta P_4$ [46]. An illustration of pressure drops is shown in Figure 2.4.

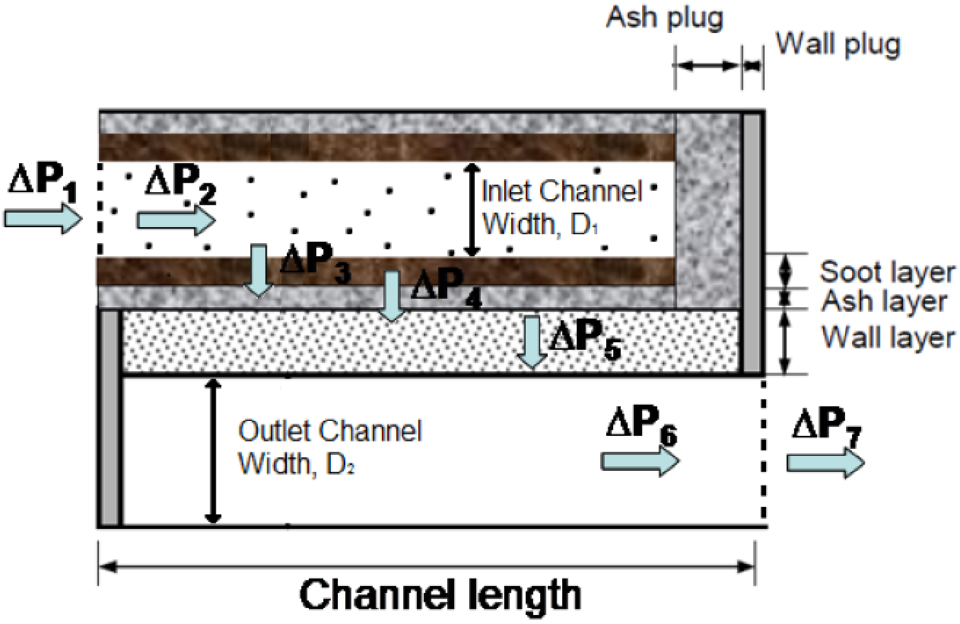

**Figure 2.4:** Modeling of pressure drop in DPF

In current work only $\Delta P_2$, $\Delta P_3$, $\Delta P_5$ and $\Delta P_6$ is considered. $\Delta P_3$ and $\Delta P_5$ follows Darcy's law fluid flow through porous medium [49]. The pressure drop for inlet channels ($\Delta P_2$) is an extension of clean filter pressure drop, which accounts for the decrease in channel size due to the build-up of cake layers. The equations for relevant pressure drop source are as following:

$$\Delta P_2 = \frac{\mu \dot{V}}{2V}(D + w_{wall})^2 \frac{4\xi L^2}{3 \cdot (D - 2w_{cake})^4} \tag{2.74}$$

$$\Delta P_3 = \frac{\mu v_{cake}(D - 2w_{cake} - 2w_{ash})}{2k_{p,cake}} ln\left(\frac{D}{D - 2w_{cake} - 2w_{ash}}\right) + \beta_{cake}\rho_g w_{cake} v_{cake}^2 \tag{2.75}$$

$$\Delta P_5 = \sum_{\mathtt{i}} \frac{\mu v_s(\mathtt{i}, t) w_s(\mathtt{i}, t)}{k_{p,s}(\mathtt{i}, t)} + \beta_s \rho_g w_s(\mathtt{i}) v_s^2 \tag{2.76}$$

$$\Delta P_6 = \frac{\mu \dot{V}}{2V}(D + w_s)^2 \frac{4\xi L^2}{3 \cdot D^4} \tag{2.77}$$

To apply Darcy's law, it requires properties such as permeability of the filter $k_{p,s}$ and soot cake layer $k_{p,cake}$. The permeability of filter wall $k_{p,s}$ is calculated from deep filtration model, see Appendix A.2. The soot permeability is calculated with Knudsen number, Stokes-Cunningham factor, and Kuwabara function, see Appendix A.1. An increase in permeability means decreases in pressure drop [19].

#### 2.3.3.3 Reaction kinetics model

The regeneration is assumed to occur at 3 possible layers as shown in the Figure 2.5 [46].

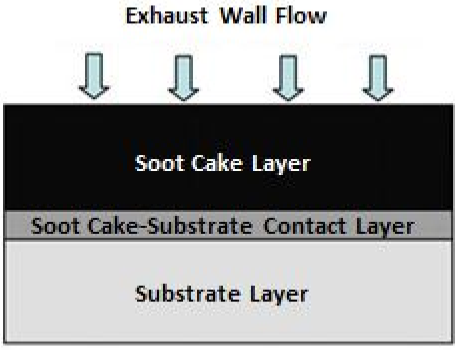

**Figure 2.5:** DPF modeling of layers in DPF module

Different kinetics may be applied to each layer if flexibility is needed, but there are a few limitations. The soot cake layer is designed for reactions involved with soot. Thus, absorption and desorption reactions are not allowed. Soot cake-substrate contact layer is an intermediate location intended for catalyzed soot oxidation. However, these modeling option origins from older publications and is considered outdated instead it is recommended to use the substrate layer for catalyzed reactions. The substrate layer represents the substrate wall which may include surface reactions.

## 2.4 Numerical Solvers

A brief explanation about solver's characteristic is presented with the aim to determine where caution is needed. The default ODE solver used in GT-POWER is explicit 5th order Runge-Kutta (RK) which is highly efficient for non-stiff problems such as flow problem in simple geometry. However, stiffness can arise when chemical reactions are introduced. Therefore, special solvers are needed for the calculation mesh inside the reaction module. In general, Advanced Adaptive solver is recommended for the mesh inside catalyst brick [46]. But this solver is not applicable in DPF module with diffusion model on. Other possible choices of solver are Backward Differential Formulation (BDF), Adaptive RK, RK-BDF and RADAU.

The advanced adaptive solver is a quasi-steady state solver designed specifically to be used in stand-alone aftertreatment application. It initializes by generating fixed mesh according to the discretization length set by the user and solves some of the governing equations on the sub-volume that have external source presented (i.e. boundary value is known, such as solid temperature, coverage [46]). Then, the solver adaptively generates a mesh to solve other governing equations on each time step.

Most tolerances limit can be set by the user except two. The first one is truncation error which can become large when axial conduction of heat is significant compared to convection and heat transfer with bulk gas. Second is the interpolation error, since the boundary condition for the adaptive mesh is interpolated from the fixed grid. The interpolation error could arise if the localized value of solid temperature rapidly changes. The recommended method to minimize these errors is to decrease the discretization length to have more than 40 axial sub-volume or no larger than 5 mm, whichever is applicable.

Time step provided by the user is considered as 'master' time step. Advanced adaptive solver dynamically chooses its own time step but can never exceed the master time step. On the numerical point of view, the recommendation provided with software is to choose large time step and not to intervene with the solver. It is recommended to measure the ratio between the dynamic time step used and master time step to examine the efficiency of the solver. 5 or higher indicates that the solver is working efficiently while values lower than 2 indicates that the solver is running inefficiently.

BDF solver is an implicit ODE solver which is robust to solve stiff equation systems. An example of such system is; when the system has interaction between very fast and very slow dynamics or when the magnitude of reaction rates between two reactions differ by a large margin. Adaptive RK, RK-BDF and RADAU are explicit solvers which are generally more efficient compared to BDF solver but cannot robustly handle stiffness [46, 50]. Adaptive-RK adaptively adjusts its mesh and time step similar to advanced adaptive does. It is the most efficient solver in this class. RK-BDF combined adaptive-RK and BDF together, the solver uses adaptive-RK but can dynamically change to BDF solver when facing with stiffness and thus, improve the efficiency from the standalone RK. Lastly, RADAU uses higher order RK method which has higher numerical robustness but is very computationally expensive [46].

# 3

# Experimental Data Description and Analysis

This chapter describes the provided raw data in this work and the experimental methods to obtain them. The data consists of both monolith and DPF soot oxidation experiments. They are summarized in Table 3.1. In addition, the analysis of data was performed and presented here. This includes parameter analysis of the kinetics, pressure drop and deep filtration model which were described in previous chapter.

**Table 3.1:** The provided experimental data in the current work.

| Experiments | Soot type | Setup |
|---|---|---|
| Step-response isothermal experiments[a] | Printex-U | Monolith |
| DPF engine data[b] | Diesel soot | DOC+DPF |

---

[a] Chalmers, [15, 16]

[b] AB Volvo

## 3.1 Isothermal step-response experimental data

The isothermal oxygen step-response experiments were performed in another work [16]. In summary, synthetic soot Printex-U was deposited onto the substrate of a flow-through monolith. The monolith had a total cell density of 400 cpsi, with a substrate wall thickness of 6.5 mil and size specifications of 22 mm diameter and 20 mm length. The oxidation process was performed under kinetically controlled conditions. The total gas flow of 1.5 L/min at normal temperature and pressure. The experiments were conducted in three temperatures (580,605,630°C) at 2 vol. % $O_2$. The supply of oxygen was switched on at t=60 s. The equipment setup consisted of a mass flow controller to control the inlet gas composition followed by an insulated part into a blank monolith acting as a thermal controller. Thermocouples were placed in the blank monolith, in the center of the soot loaded monolith and at the end as well. On-line infrared (IR) analyzers were utilized to measure the gas composition of $CO$ and $CO_2$.

The amount of soot (carbon) deposited on the monolith in these experiments is presented in Table 3.2, the underlying calculations can be found in Appendix A.3.

**Table 3.2:** The soot mass was obtained from integrating the $CO/CO_2$ outlet concentration of Isothermal step-response data

| Experiments | Temperature (°C) | Initial soot mass (mg) |
|---|---|---|
| SR 1 | 580 | 6.2 |
| SR 2 | 605 | 6.3 |
| SR 3 | 630 | 7.6 |

### 3.1.1 Data description

The initial sharp peak at the beginning in Figure 3.1 shows a high reactivity of soot oxidation. This indicates destabilization of metastable oxide surface complex, which in the presence of oxygen desorbs instantaneous at reaction temperature [34, 35]. The formation of these reactive surface oxide complex is evident, the initial high reactivity was reproduced by exposing the oxidized soot samples with ambient air[16]. The second broad peak at around 30% conversion shows a slowly increasing in reactivity. The broad peak might be related to the increase of accessible active sites. Studies show the number accessible active sites increases at low conversion until 34% [29]. Another explanation to the second peak is because of pore growth. The pore growth increases the porosity of soot at conversion 30-60% [51]. Thus, leading to increasing in carbon surface area and active sites.

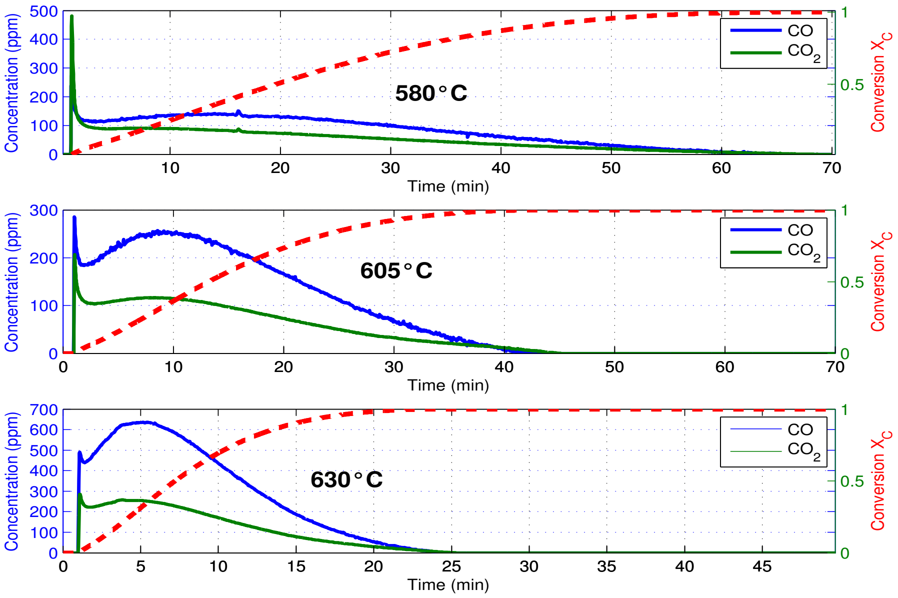

**Figure 3.1:** Data of step-response experiments for three different temperature levels. The red dashed line is the corresponding conversion of carbon $X_C$.

### 3.1.2 Global kinetic parameters for soot oxidation by $O_2$

Analysis of the experimental data was performed in order to find the range of kinetic parameters for model 1 and 2. Especially the kinetic parameters for the rate determining steps in these models. The rate determining step were investigated using Arrhenius plot analysis (equation (2.13)) and applying the global power-law model (equation (2.12)) over different carbon conversions [16, 21]. The carbon conversion was obtained by integrating the outlet concentration of $CO/CO_2$. A conversion interval of 5% was defined to obtain a comprehensive analysis.

The data was therefore divided into 20 separate conversion intervals. An averaged rate was calculated in each interval. Where the overall rate ($CO{+}CO_2$) was normalized to the carbon concentration $[C_0](1-X_C)$. The rate of $CO/CO_2$ was also treated separately. The equation was used (2.13) to analyze the pre-exponential factors and activation energy. The analysis of the activation energy and pre-exponential factors are presented in Figure 3.2.

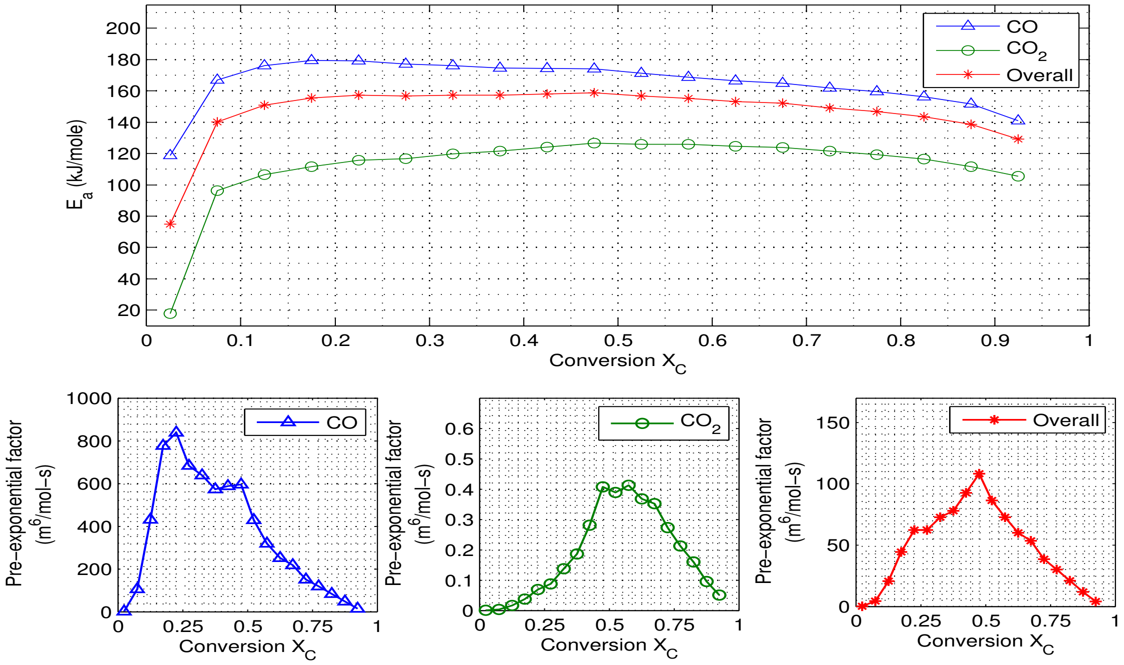

**Figure 3.2:** The plot on the top shows the analysis of activation energy versus carbon conversion. The pre-exponential factors in the bottom plots are calculated using the intercepts from the Arrhenius plot analysis. Note the units for the pre-exponential factor here is in $m^6$/mol-s.

The overall activation energy in Figure 3.2 is in the higher end of the reported range [21, 52, 53]. In contrast, other studies reported activation energy of 105-130 kJ/mol [27, 54, 55]. There are no consensuses regarding activation energy and one reason behind the wide range of reported values could be because the difference in the experimental method as well as data analysis method. The kinetics analysis might be valid but the data is limited to a narrow temperature interval, thus difficult to confirm the robustness of the parameters. In Figure 3.2, the overall activation energy is increasing when the conversion is between 0-20%. The activation energy is approximately constant when the conversion is between 20-

50%. The activation energy difference between $CO$ and $CO_2$ varies from 48-100 kJ/mol in the conversion range of 0-50%, while at higher conversion is the difference narrowed to 50-40 kJ/mol. The pre-exponential factor for $CO$ increases over the conversion range of 0-20% and it is approximately 3-4 orders of magnitude larger than the pre-exponential factor of $CO_2$.

It would be an unconventional approach to model the change in activation energy [56]. It is more likely a change in the pre-exponential factors or carbon reaction order, which reflects the change in active sites. The second broad peak for $CO/CO_2$ occurs at approximately at the same conversion for high temperatures (30% conversion), see Figure 3.3. One exception is the second broad $CO_2$ peak at 580°C.

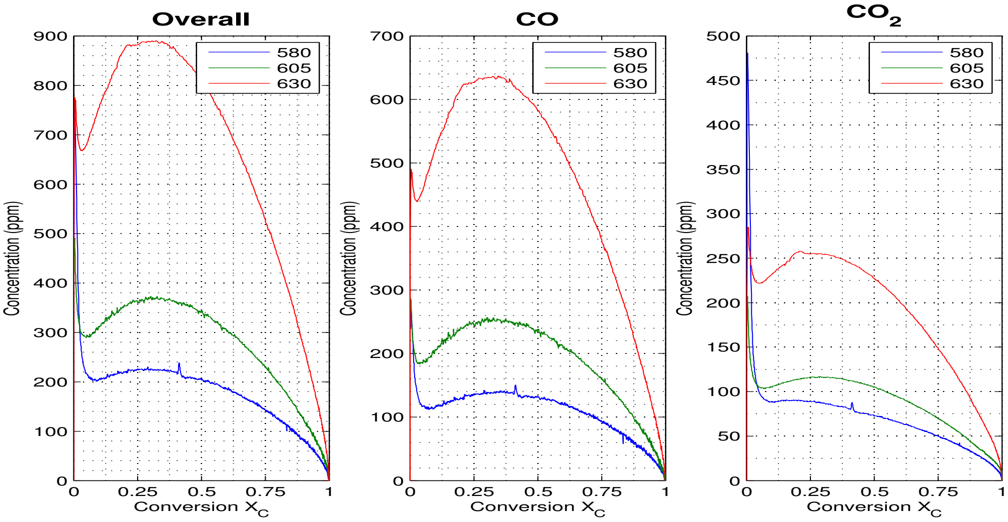

**Figure 3.3:** Plot of reaction rates against carbon conversion at different temperature levels. The reaction rates were generated using the values from the analysis. The first plot from the left represents the overall rates, $CO$ and $CO_2$.

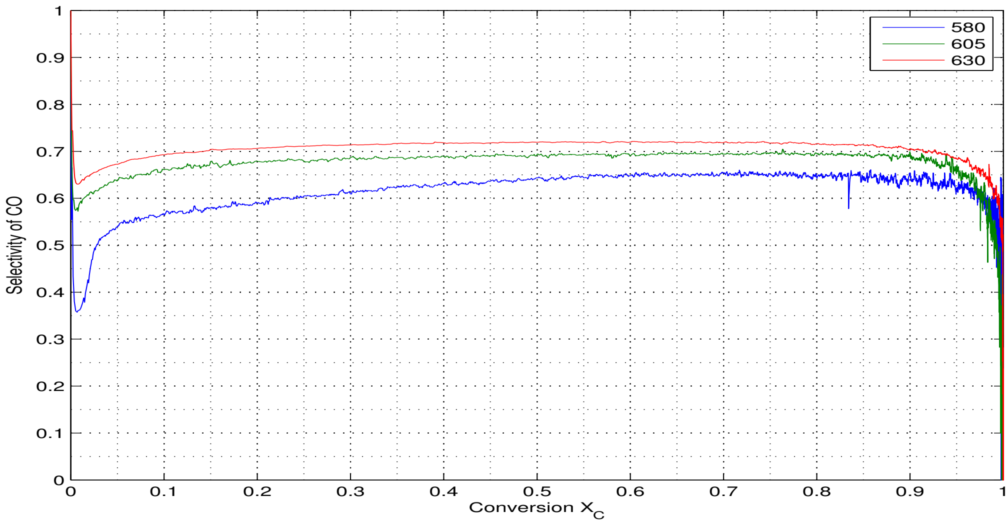

**Figure 3.4:** Plot of $CO$ selectivity against carbon conversion $X_c$.

The difference in kinetic parameters between $CO$ and $CO_2$ is greater at low conversion, see Figure 3.2. Since the $CO$ selectivity is unfavored at the beginning, see Figure 3.4. The $CO$ selectivity is approximately constant at high conversion and higher temperature, but that is not the case for 580 °C. The deviation in 580°C is likely that the Printex-U sample in the experiment is in different condition, such as carbon microscopic structure, available number of active sites, time exposure in ambient air or presence of other reactions that become significant at low temperature. Similar observation was seen in experiments from another study with reaction condition at 605°C [16] as well.

The previous analysis offered a range of parameters that was further investigated using global power-law model equation (2.11) by plotting $log(rate)$ against $log(1 - X_c)$ where $X_c$ is conversion of carbon, where the slope is affected by the reaction order of carbon, see Figure 3.5.

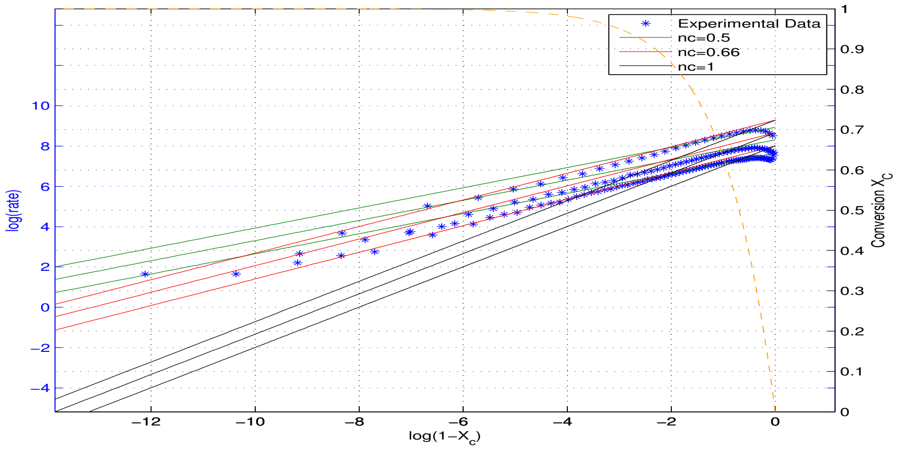

**Figure 3.5:** Plot $log(rate)$ against $log(1-X_c)$. The computed rates are the solid lines with green or red or black color. Each color represents the three temperature levels (580, 605 and 630°C) computed with different carbon reaction orders $\eta c$ 0.5, 0.66 and 1. The blue markers are the experimental values. The dashed orange line represents the conversion of carbon

The plots in Figure 3.5 corresponds to global power-law model with an activation energy of $E_a$=164 kJ/mol, pre-exponential factor $A$=2E9 $m^3$/mol-s and a carbon reaction order of 2/3. These parameters were obtained through iterative methods. Notice the unit of the pre-exponential factor which has already the reactor volume (V=7.6E-6 $m^3$) included, hence its order of magnitude.

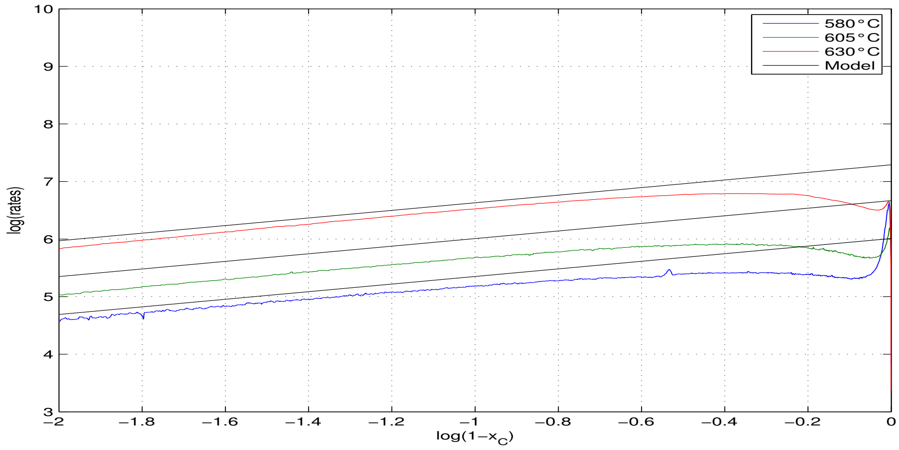

**Figure 3.6:** Plot $log(rate)$ against $log(1-X_c)$ in low conversion regime. The order of the carbon is not constant in this regime.

The carbon reaction order indicates shrinking sphere model is feasible here. However, the global power-law model from above is not sufficient to predict the low initial conversion, the model overestimate the soot oxidation which is displayed in Figure 3.6. Apparently, it is only capable of predicting the reactivity for conversions above 40%.

The same approach was performed on $CO$ and $CO_2$ separately to find the kinetic parameters for each reaction. The Activation energy for $CO$ and $CO_2$ was found to be 168 and 140 kJ/mol respectively, with the corresponding pre-exponential factors 2.0E11 and 1.8E9 $m^3$/mol-s. The carbon reaction order was approximately 0.66 for $CO$ and 0.6 for $CO_2$.

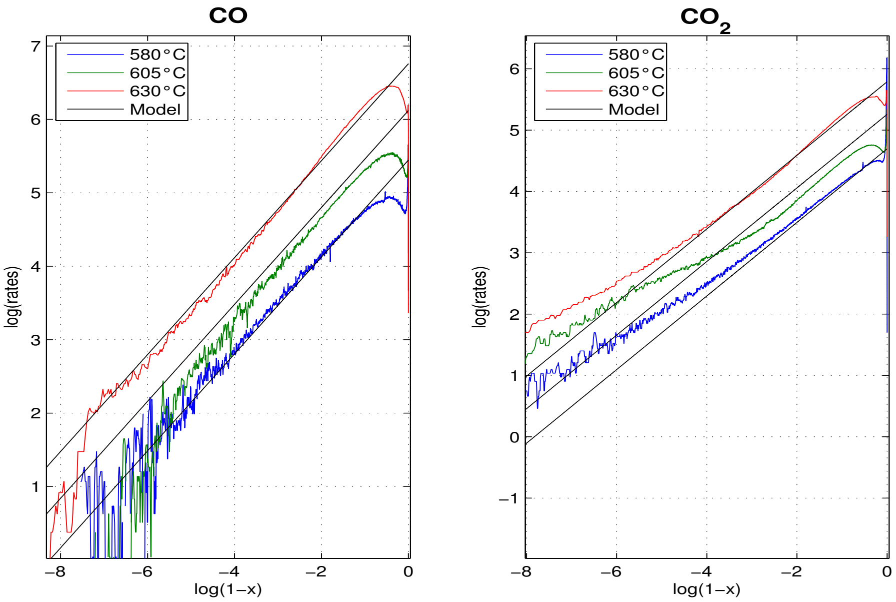

**Figure 3.7:** Plot $log(rate)$ against $log(1 - X_c)$ for individual rates of $CO$ and $CO_2$

### 3.1.3 Estimation of $C^*(s)/O^*_{ads}$

The detailed kinetic models described in Section 2.2.6 assumes soot is modeled by two species. One is relatively reactive compared to the other. The initial sharp $CO$ and $CO_2$ peaks shown in Figure 3.1 represent the reactive species that are accounted for in model 1 and 2 (model 1: $O^*_{ads}$ ; model 2: $C^*(s)$). Integration of the initial peak yields the estimation of the amount of reactive species. It is assumed that the reaction with these species are independent from each other. In addition, the relatively less reactive species is modeled with a polynomial model. The model was fitted towards the concentrations of $CO$ and $CO_2$ curves from the experimental data, see Figure 3.8. The fitted model subtract the measurement data yields the amount of reactive species. The amount of reactive species in each experiment was estimated and shown in Table 3.3. The total amount of reactive species cannot be correlated in any way, thus, inconclusive to predict the amount of initial reactive species. Note that the integrated difference is in the unit of concentration fraction and the molar flow rate is used to convert fraction to moles. The total concentration (mol/$m^3$) is obtained by dividing the moles with the reactor volume.

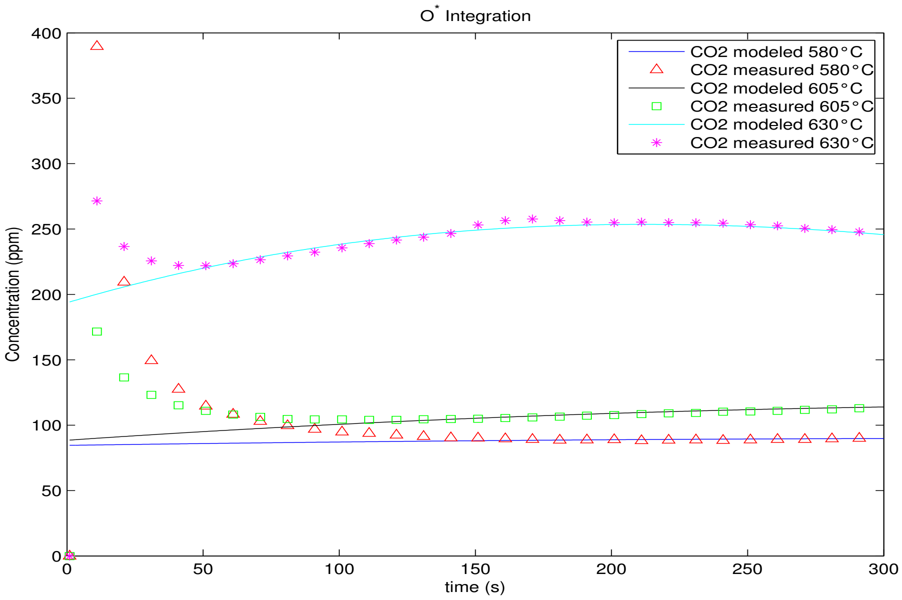

**Figure 3.8:** A $5^{th}$ degree polynomial function is used to model the data after approximately 50-75 seconds. The integration difference in the experimental data and model determines the concentration of reactive surface species.

**Table 3.3:** Concentration of reactive species: $O^*_{ads}/C^*(s)$

| **Temperature** (°C) | 580 | 605 | 630 |
|---|---|---|---|
| **Reactive species concentration** ($mol/m^3$) | 3.4 | 3.1 | 3.2 |

The initial concentration of reactive species is approximately 3.7-5.0% relative to the carbon concentration. On the other hand, it is reported that 10 wt % of Printex-U is not carbon element atoms. The reported composition ranges between 90.5-92 wt % for carbon, 8.1 - 8.4 wt % O , 0.52-0.70 wt % H, 0.17-0.22 wt % N and 0-0.4 wt % S [14, 16].

## 3.2 Diesel particulate filter $NO_2$ oxidation data

The data were provided by AB Volvo. It was taken from test runs of a $CCRT$© setup. It consists of a DPF made of cordierite with Platinum wash-coated and a DOC unit upstream. The setup is connected to a turbocharged, multi-cylinder engine (Euro VI). The temperature is increased by adjusting the engine load at a constant speed of 1200-1800 rpm depending on the data set. Both inlet and outlet of the filter media were wash-coated containing platinum catalyst. The total cell density is 200 cpsi, the substrate wall thickness is 12 mil and sized 12 inches in diameter and length. The soot inlet to DPF is measured by an on-line AVL483 micro soot sensor. Gauge pressure was measured at the inlet and outlet. The gas outlet composition is measured with standard engine workbench emission analyzer (HORIBA MEXA-7000 series) equipped with $CO_2$/$CO$ (IR) and $NO_x$ (chemiluminescence) analyzers.

### 3.2.1 Description of DPF engine data

There are two types of engine data that were available in the current work. They were either semi-steady state or transient. Table 3.4 shows an overview of operating conditions in DPF data. In the semi-steady state data, the experiment started on a clean filter and soot was introduced with the exhaust from an engine during the experiments. In order to investigate soot oxidation by $NO_2$, the engine load was increased step-wise to increase the $NO_x$ concentration, exhaust temperature and flow rate, see Appendix C for the plotted data. The transient data had an initial soot loading of 4.81 g/L. The transient experiments were performed consecutively and the soot mass was measured after each experiment, see Appendix D. More details about these data are described in the sections below.

**Table 3.4:** Summary of operating conditions in DPF engine data. The exhaust composition was taken from the outlet of upstream DOC.

| Experiments | Exhaust temp. (°C) | Pressure drop (kPa) | Initial Soot mass (g) | Massflowrate (kg/s) | $NO_x$ (ppm) | $O_2$ (%) | CO (ppm) | $CO_2$ (%) | $H_2O$(%) |
|---|---|---|---|---|---|---|---|---|---|
| SS 1 | 200-410 | 2.54-8.30 | 0 | 0.113-0.300 | 130-630 | 10.2-17.0 | 5-8 | 2.7-7.8 | 2.5-7.0 |
| SS 2 | 215-394 | 3.31.8.39 | 0 | 0.200-0.445 | 200-1000 | 15.9-10.0 | 5-9 | 3.4-7.8 | 2.6-7.0 |
| Transient 1 | 170-327 | 1.7-13.2 | 4.811 | 0.02-0.44 | 11-1000 | 1-21 | - | 0.1-12.3 | 0-12.8 |
| Transient 2 | 170-327 | 1.6-12 | 4.316 | 0.02-0.45 | 9-1000 | 1.2-21 | - | 0.1–12.4 | 0-12.7 |
| Transient 3 | 223-406 | 1.5-11.9 | 4.092 | 0.03-0.48 | 0-1350 | 4.6-21 | - | 0.1-10.9 | 0-10.5 |
| Transient 4 | 223-406 | 1.5-10 | 0.989 | 0.03-0.48 | 0-1325 | 4.5-21 | - | 0.1-10.8 | 0-10.5 |

### 3.2.2 Semi-steady state DPF data

There are two available data for the semi-steady state experiments (labeled as SS 1 and SS 2 from now on). In the semi-steady state data the temperature was increased as well as exhaust flow rate (S.V = 14200-50400 $h^{-1}$ at standard conditions) with different $NO_x$ concentration levels (130-630 ppm and 200-1000 ppm). The data was plotted and presented in Appendix C. Soot oxidation by $NO_2$ begins to be significant at approximately 300°C in these data. This is evident from the pressure drop measurements against time, see Figure 3.9. The pressure drop increases with the exhaust flow rate, but also because of the soot is introduced to the filter (positive slope). The slope is 0 at the balance point temperature. Whereas the negative slope at higher temperatures indicates the significance of soot oxidation.

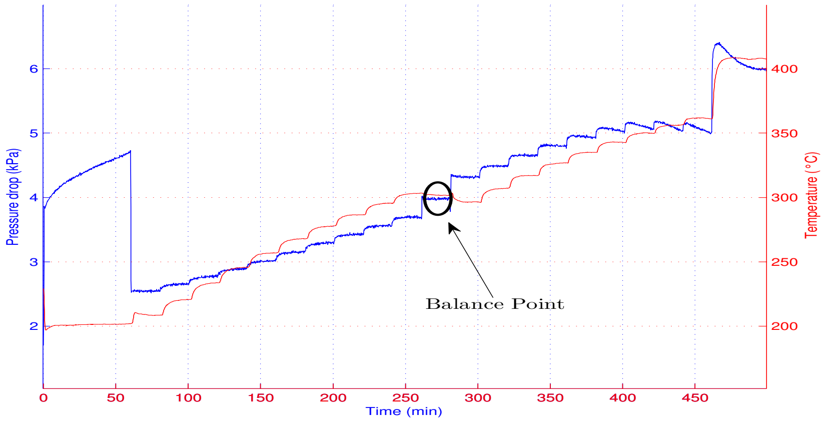

**Figure 3.9:** The balance point temperature is approximately 300°C.

The main usage of these data was to develop the DPF model. Part of the DPF model is $NO$ oxidation which is described in Section 2.2.7, pressure drop model from Section 2.3.3.2 and as well as deep filtration model elaborated in Section 2.3.3.1. Analysis of detailed kinetics was unable to be conducted here since the DPF had platinum catalysts which promoted oxidation of $CO$ to $CO_2$. Therefore, the measurements cannot be used for selectivity studies in soot oxidation. In addition, the measurements are not sensitive enough to measure the soot oxidation in details, $CO_2$ is measured in fraction while the $CO$ from soot oxidation is in ppm level (2-3 orders of magnitude larger values).

Hydrocarbons are presented in these data but they are in very low concentrations. Hence, hydrocarbons were neglected in the model. Pre-treatment of the $NO_x$ data was necessary because of $NO_x$ imbalanced caused by using two separate analyzers for inlet and outlet. The $NO_x$ outlet concentration was normalized to the inlet concentrations.

### 3.2.2.1 Deep filtration analysis

Deep filtration can be observed from the pressure drop in one of the semi-steady state DPF data (SS 1). The soot fills up the substrate and as a consequence, the pressure drop increases non-linearly due to the change in filter wall permeability. It was characterized in the initial slope from t=0-15 min, see Figure 3.10. Integrating soot mass injection within that time frame is approximately 0.1 g/L (2.5g). The slope becomes later linear which indicates the substrate is full and the injected soot thereafter is only contributing to soot cake build-up.

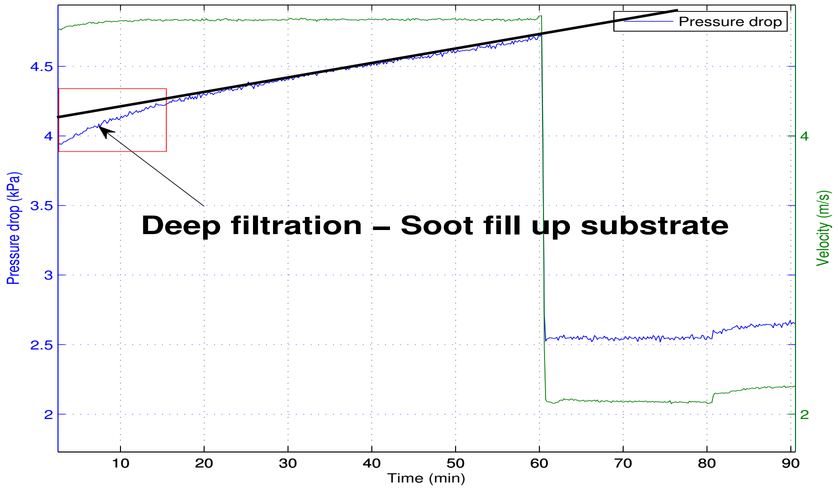

**Figure 3.10:** Deep filtration occurring in the highlighted area in data set SS 1. When pressure drop increases linearly (solid black line) indicates soot cake formation.

If 0.1 g/L of soot was loaded when the substrate is full. It would take approximately 27 min for the other data set (SS 2) to fill the substrate, see Figure 3.11. The deep filtration in these data is not obvious because of the lower soot flow rate. Therefore, the first data set (SS 1) is ideal as a starting point to calibrate the initial soot loading and pressure drop. The percolation constant and packing soot density inside the filter wall is two parameters that affect the distribution of the injected soot (i.e. governed where the soot is accumulated, either to the substrate or soot cake). These parameters were calibrated to obtain a similar shape as SS 1 and the values are shown in Table 3.5.

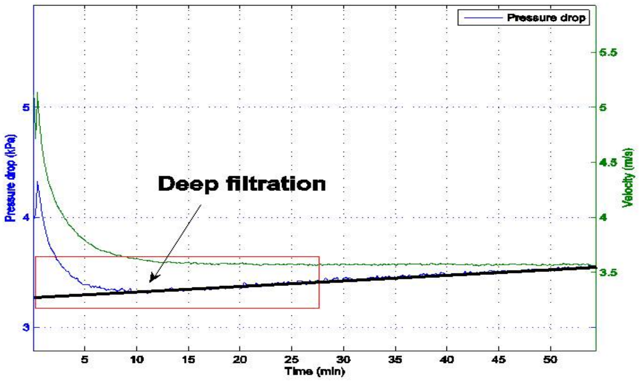

**Figure 3.11:** Deep filtration occurring in the highlighted area in data set SS 2. When pressure drop increases linearly (solid black line) indicates soot cake formation.

**Table 3.5:** Soot properties in the substrate wall. Soot packing density in the wall and percolation constant was obtained from data calibration.

| | Units | Values |
|---|---|---|
| **Soot Packing Density in the Wall** | $kg/m^3$ | 4.5 |
| **Percolation Constant** | - | 0.81 |

Furthermore, clean filter permeability is needed to account for the flow resistance of the filter. The permeability was obtained by analyzing the of pressure drop versus exhaust velocity when the DPF has negligible amount of soot, see Figure 3.12. The figure illustrates the simulated pressure drop contribution from the clean filter as well as a loaded filter. The slope from Figure 3.12 shows no quadratic behavior. Hence, the model assumes to have linear relationship to velocity and viscosity .

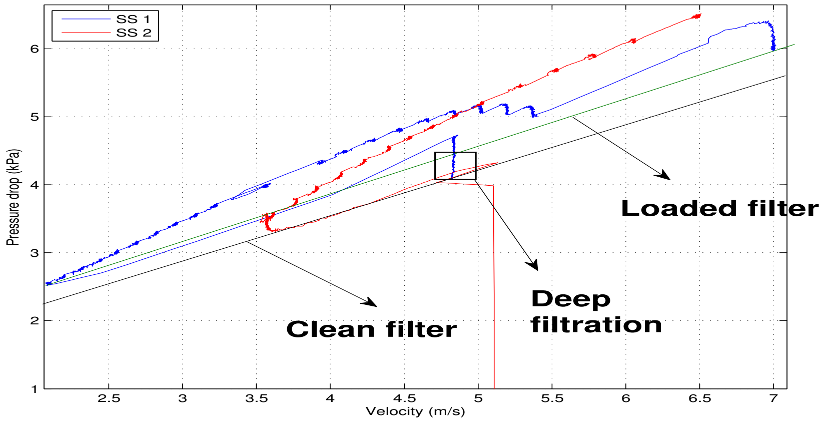

**Figure 3.12:** Plot pressure drop against velocity for data set SS 1 and SS 2. The solid black line represents the approximated pressure drop from the clean filter. The visible deep filtration regime around 4.8 m/s is highlighted. The green solid line represents the loaded filter pressure drop, while the pressure drop above that line is due to the soot cake.

Simulations of the clean filter were carried out to obtain the permeability. The result in the Figure 3.13 shows the filter permeability was approximately 6.4E-8 $mm^2$. However, The linear dependence of velocity and viscosity in pressure drop model was unable to describe the data. The pressure drop measurements shows that the model underestimates the pressure drop at lower velocity. In conclusion, the model seems to only be able to describe the pressure drop at higher velocity. This was also confirmed in data from transient experiments.

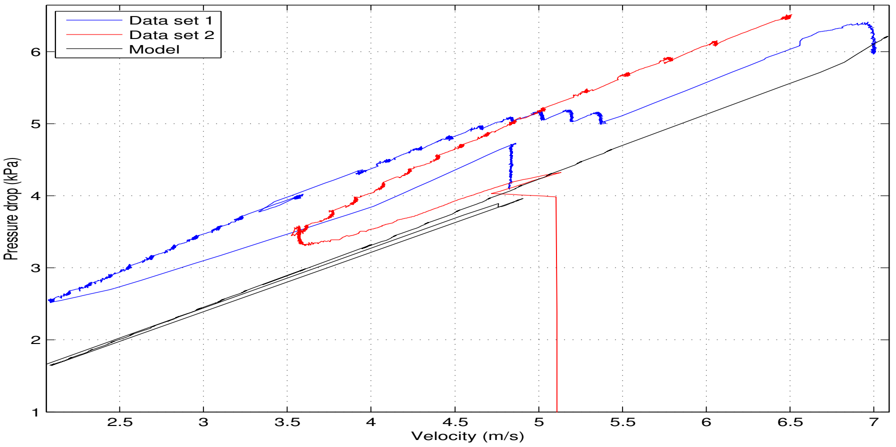

**Figure 3.13:** Simulated pressure drop with clean filter permeability of 6.4E-8 $mm^2$.

### 3.2.2.2 Kinetic parameter estimation of $NO$ oxidation

The kinetic parameters for $NO$ oxidation was obtained by analysis using equation (2.13) at low temperatures (209-235 °C), see Figure 3.14. The soot oxidation by $NO_2$ is insignificant at these temperature range and it has negligible effects on $NO$ oxidation. The analysis clearly shows two activation energies. They are both within the range of the literature value of 31 kJ/mol [44]. The intercept of the plots indicates that the pre-exponential factor for SS 2 is larger because of higher $NO_x$ inlet concentration and also exhaust flow rates.

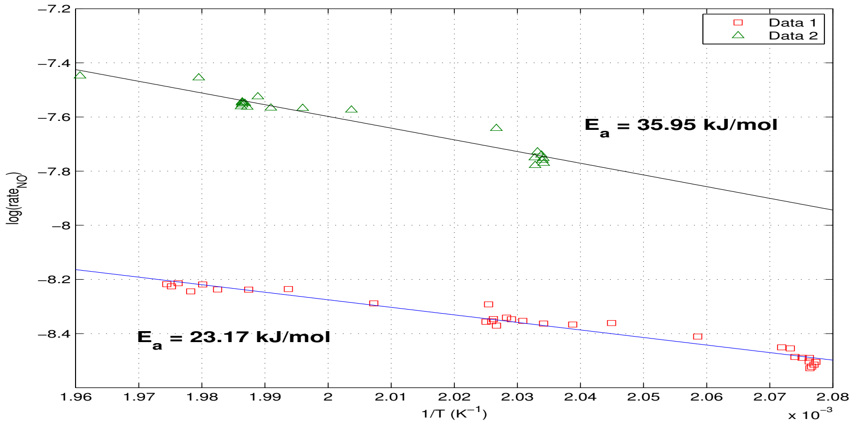

**Figure 3.14:** Arrhenius plot of $NO$ oxidation for semi-steady state data. Where the considered temperature range is 209-235 °C.

The $NO$ oxidation is thermodynamically limited, it means the temperature and space velocity may greatly affect the $NO_2/NO_x$ ratio. But that was not the case in semi-steady state data, see Figure 3.15. $NO$ oxidation does not only occur at the inlet channels but also inside the substrate walls. The converted $NO_2$ in the substrate diffuses back to the soot cake for oxidation. The concentration of $NO_x$ is balanced indicate that there is no reduction reaction to $N_2$ occurring (i.e. $NO_{x,in} = NO_{x,out}$). Moreover, $NO$ oxidation can also occur in the outlet channels since the outlet is also wash-coated with catalyst. The

$NO/NO_2$ concentration in the outlet might not be the concentration after soot oxidation, thus, leading to underestimating the soot oxidation in the model. However, as long as the $NO$ oxidation is not on the thermodynamic equilibrium, as in Figure 3.15. The model should be able to account for the NO oxidation in the outlet channels by specifying the correct amount of catalyst in the DPF.

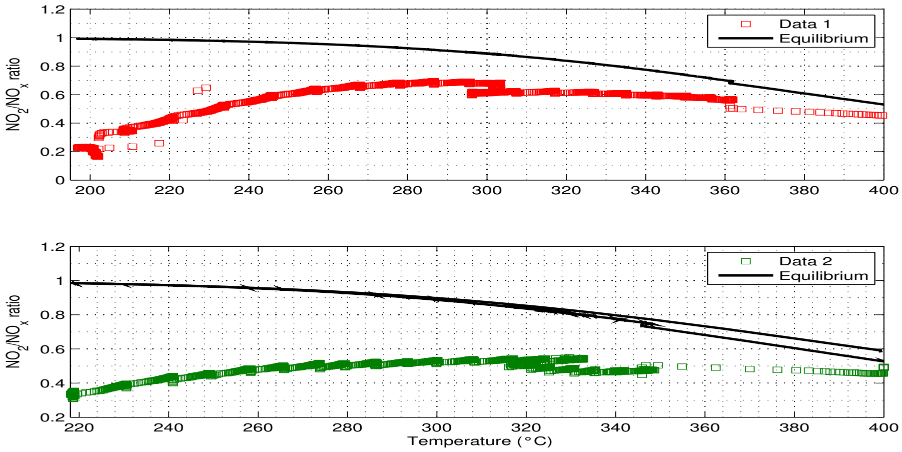

**Figure 3.15:** $NO_2/NO_x$ ratio in the outlet from semi-steady state experiments.

### 3.2.3 Transient DPF data

The same DPF was considered in these data. It was pre-loaded with soot by filtering the exhaust from an engine without performing regeneration. Thus, diesel soot was allowed to accumulate and the mass of the DPF was measured before and after. The measured total soot loading was 4.68 g/L. Soot oxidation was then performed in various engine cycles. First set of cycles consisted of six low temperature cycles (170-327°C). This was repeated twice and followed by another two sets of three high temperature cycles (223-406°C). After each set of cycles, the DPF filter was disconnected and cooled in ambient condition and weighted to find the soot load, see Table 3.6 for measured soot loading. Also, note that additional soot coming from the engine was added continuously during the cycles.

**Table 3.6:** Table shows the measured soot loading in transient data. The calculation of soot loading was based on the DPF volume (22.24 L), where the initial soot mass was 107 g and the measured soot mass 96,91,22 and 7 g after each experiments.

| Experiments | Initial soot loading (g/L) | Measured soot loading (g/L) |
|---|---|---|
| Transient 1[a] | 4.811 | 4.316 |
| Transient 2[a] | 4.316 | 4.092 |
| Transient 3[b] | 4.092 | 0.989 |
| Transient 4[b] | 0.989 | 0.315 |

---

[a] Low temperature transient cycles

[b] High temperature transient cycles

#### 3.2.3.1 Kinetic parameters for soot oxidation by $NO_2$

The activation energy of soot oxidation by $NO_2$ is estimated by using the DPF engine data of soot loadings, see Figure 3.16. The slope in Arrhenius plot shows a value of 86.8 kJ/mol. Which is reasonable compared to other studies which reported 80 kJ/mol overall activation energy of diesel soot [8, 28].

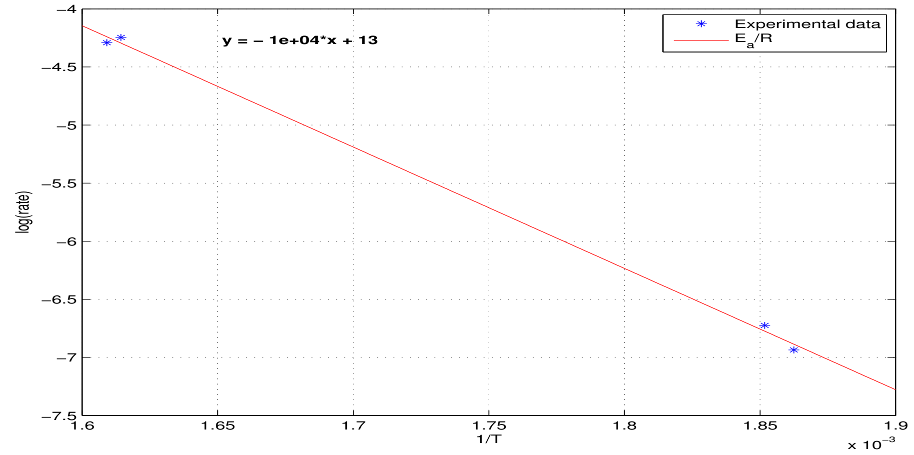

**Figure 3.16:** Estimated activation energy of DPF transient experiments.

Similar analysis was performed using the global power-law model as shown in section 3.1.2 and the result is shown in Figure 3.17. The calculations are based on the soot loadings for each experiment, see Table 3.6. The reaction order of carbon was found to be 1 in these data. The reported carbon reaction order is mixed ranging from 2/3 to 1 [8, 31, 57]. The difference might be because of different type of soot (real or synthetic) that is oxidized. Also, real diesel soot properties are correlated to fuel type and engine load [58, 59].

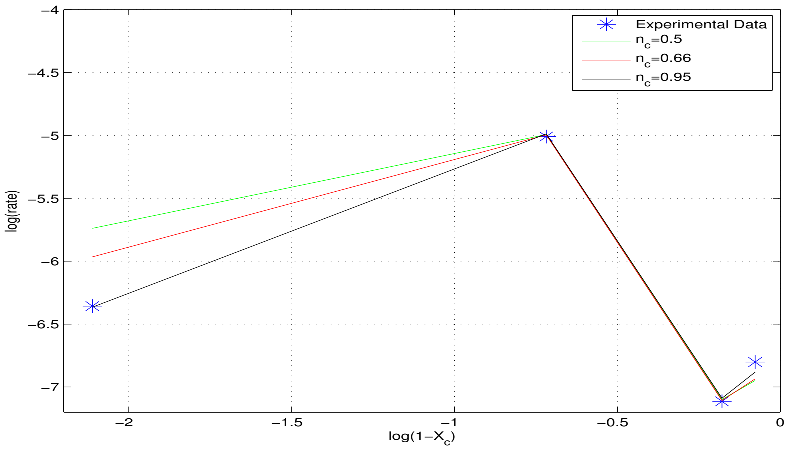

**Figure 3.17:** The reaction order of carbon for transient experiments.

### 3.2.4 Summary of estimated parameters from the analysis

**Table 3.7:** Table shows the estimated range of parameters for the models.

| | Pre-exponential factor ($m^3/mol\text{-}s$) | Activation energy (kJ/mol) | Reaction order of Carbon |
|---|---|---|---|
| Soot oxidation by ${O_2}^a$ | 2E9 | 164 | 2/3 |
| $CO^b$ | 2E11 | 168 | 2/3 |
| ${CO_2}^b$ | 1.8E9 | 140 | 0.6 |
| Soot oxidation by ${NO_2}^a$ | 3.8E6 | 86.8 | 1 |
| $NO$ oxidation | 8E2-2.7E5 | 23-35.95 | - |

---

[a] Overall
[b] Individual

# 4

# Implementation in GT-POWER

The governing equations (previously mentioned in Section 2.3) are coded into modules and the user has to define certain physical parameter before the simulation can be started. The user-interface is designed for drag and drop and connect modules to create a dynamic process simulation, see Figure 4.1. There are two main types of reactors modules for exhaust aftertreatment. One is the catalyst brick module. It is used for flow-through reactor modeling (e.g. DOC and SCR modeling). The other reactor module is the wall-flow DPF. Kinetics is applied in the reaction modules externally connected to the reactor module, either global reaction module when working with gas phase reactions or surface-reaction module for kinetics on heterogeneous catalysis. Further explanation about reaction module can be found in Appendix A.4.

## 4.1 Catalyst Brick Implementation

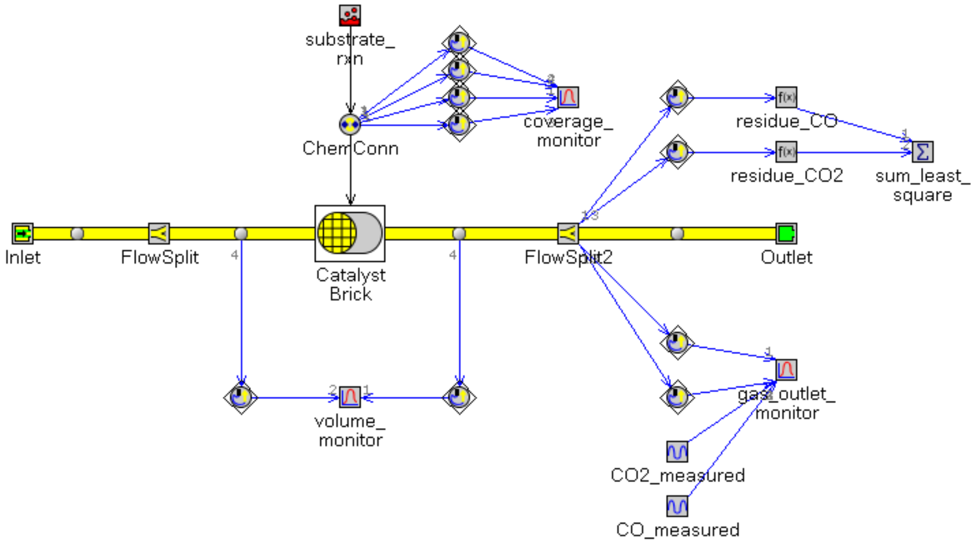

**Figure 4.1:** Overview of the constructed catalyst brick flowchart in GT-POWER.

The simulation of flow-through experiments was conducted in a catalyst brick module. The module requires inputs such as sizing of the monolith and reaction conditions were set equal to the experiment's condition. The kinetics models were implemented and solved by the solver in surface-reaction module. However, catalyst brick module prohibits solid species from being accumulated and consumed. Therefore, techniques to bypass this limitation had been developed to replicate the soot deposit in monolith experiments with this module.

The technique exploited the module's function to store molecules in active sites and the fact that soot layer is a layer of carbon atoms deposited on top of the filter wall. The technique was effectively realized by creating the active site species $Z$ dedicated for storage of carbon atoms (called carbon site species) on the substrate. The density of carbon site species (denoted as $\lambda_{carbon}$) was calculated using the amount of carbon mass deposited on the monolith in experiments, see calculation in Appendix A.3. The site occupied with carbon atom is denoted as $ZC$ while the empty site is denoted as $Z$. Thus, the coverage of $ZC$ (denoted as $\theta_{ZC}$) is equivalent to 1-$X_C$.

The carbon surface itself was considered as an active site (called surface site). The coverage of the surface active sites was implemented by creating an additional active site species. The density of these species is shown in Table 4.1 and the calculation is in Appendix A.3.

**Table 4.1:** Active site density for storage of carbon and the carbon surface active sites in model 1.

| **Active Site Density** | SR1 | SR2 | SR3 |
|---|---|---|---|
| $\lambda_{Carbon}(\mathbf{mol}_{site}/m^3)$ | 68.28 | 69.14 | 83.65 |
| $\lambda_{Surface}(\mathbf{mol}_{site}/m^3)$ | 21.785 | 22.061 | 26.692 |

### 4.1.1 Implementation of model 1

The coverage of the carbon surface active sites for model 1 consists of 4 coverage species which are $O_{ads}$, $CO_{ads}$, $O^*_{ads}$ and the vacant site $s$. The initial coverage species of $O^*_{ads}$ was obtained from the analysis in Section 3.1.3, but the value seems to be insufficient for a satisfactory fit. Hence, the initial coverage of other species were calibrated to fit the model with the experimental results. Although, the calibrated values are in the same order of magnitude to the values from the analysis, which conclude that the values from the analysis are sensitive to the utilized method obtaining the reactive species. The utilized parameters for model 1 is shown in Table 4.2.

**Table 4.2:** Initial coverage used in Model 1 simulations. Note that the carbon in the initial coverage of $CO_{ads}$ is equal to $\lambda_{carbon}(1 - ZC)$.

| **Experiments** | SR 1 | SR 2 | SR 3 |
|---|---|---|---|
| **Temperature** (°C) | 580 | 605 | 630 |
| **Initial Coverage** | | | |
| $\theta_{CO_{ads}}$ | 0.12 | 0.14 | 0.25 |
| $\theta_{O_{ads}}$ | 0.25 | 0.08 | 0.05 |
| $\theta_{O^*}$ | 0.17 | 0.075 | 0.075 |
| $\theta_{ZC}$ | 0.936 | 0.974 | 0.984 |

The mean-field kinetic models presented in Section 2.2.6 was implemented in the surface-reaction module. The parameters that were used are based on the analysis from Section 3.1.2. However, some calibration of the parameters was needed (e.g. fast reactions) because of the models' complexity. The optimized kinetics parameter is presented in Table 4.3. It should be noted that the pre-exponential factor (frequency factor) for reaction 2.26 is calculated according to the collision theory. The calculation procedure is shown in Appendix A.5. Also, note the pre-exponential factors is in units of $m^3/mol\text{-}s$. Since the rate is calculated as $mol/m^3\text{-}s$ in GT-POWER.

**Table 4.3:** Optimized kinetics parameters used in Model 1 active oxidation simulation.

| | **Pre-exponential factor** ($m^3/mol\text{-}s$) | | | $E_A$ ($kJ/mol$) | **Shrinking core term** |
|---|---|---|---|---|---|
| **Temperature** (°C) | 580 | 605 | 630 | | |
| **Reaction** (2.24) | | 2.20E+10 | | 185 | |
| **Reaction** (2.25) | | 164.48 | | 36 | |
| **Reaction** (2.26)[1] | 1.34E+08 | 1.32E+08 | 1.30E+08 | 151 | |
| **Reaction** (2.27) | | 7.90E+08 | | 162 | $G(1)$ |
| **Reaction** (2.28) | | 8.89E+11 | | 200 | $G(2)$ |
| **Reaction** (2.29) | | 8.65E+08 | | 155 | $G(2)$ |

Where

$$G(1) = (\theta_{ZC})^{2/3}$$

$$G(2) = \left(\theta_{ZC}+\theta_{CO_{ads}} \cdot \frac{\lambda_{surface}}{\lambda_{carbon}}\right)^{2/3}$$

where $\lambda_{surface}$ is the surface active site density and $\lambda_{carbon}$ is the carbon active site from Table 4.1. The function $G(1)$ is equivalent to the shrinking core. It is expressed as the coverage of carbon active sites $\theta_{ZC}$ and powered by 2/3. The function $G(2)$ is an extension of $G(1)$ but it also accounts for the carbon in the form of $CO_{ads}$ on the active sites.

---

[1] The frequency factor is calculated according to collision theory and it is temperature dependent. The calculation is presented in Appendix A.5

### 4.1.2 Implementation of model 2

The implementation of model 2 is similar to model 1, but one difference is the reactive carbon species $ZC^*$ that share the same site as normal carbon species. $ZC^*$ is analogous to $O^*_{ads}$ from model 1 (i.e. the active site density is the same). Another difference is the additional type of surface active site which is a fraction of the total surface active site density, see Table 4.4.

**Table 4.4:** Active site density for storage of carbon and the carbon surface active sites in model 2. Note that the sum of $\lambda_{Surface}$ and $\lambda_{Surface^*}$ is equal to the surface active site density used in model 1.

| **Active Site Density** | SR1 | SR2 | SR3 |
|---|---|---|---|
| $\lambda_{Carbon}(\mathbf{mol}_{site}/m^3)$ | 65.89 | 67.76 | 83.06 |
| $\lambda_{Surface}(\mathbf{mol}_{site}/m^3)$ | 21.13 | 21.44 | 26.29 |
| $\lambda_{Surface^*}(\mathbf{mol}_{site}/m^3)$ | 0.654 | 0.618 | 0.400 |

The same activation energy as model 1 was used in model 2, but the pre-exponential is not the same because of the coverage species. The optimized values of initial coverage and kinetic parameters are shown in Table 4.5 and 4.6.

**Table 4.5:** Initial coverage used in Model 2 simulations.

| **Experiments** | SR 1 | SR 2 | SR 3 |
|---|---|---|---|
| **Temperature** (°C) | 580 | 605 | 630 |
| | | | |
| **Initial Coverage** | | | |
| $\theta_{ZC}$ | 0.970 | 0.972 | 0.985 |
| $\theta_{ZC^*}$ | 0.030 | 0.028 | 0.015 |
| $\theta_{O_{ads}}$ | 0.30 | 0.18 | 0.25 |
| $\theta_{O^*_{ads}}$ | 0.9 | 0.45 | 0.95 |

**Table 4.6:** Optimized kinetics parameters used in Model 2 active oxidation simulation.

| | **Pre-exponential factor** $(m^3/mol\text{-}s)$ | | | $E_A$ $(kJ/mol)$ | **Shrinking core term** |
|---|---|---|---|---|---|
| **Temperature** (°C) | 580 | 605 | 630 | | |
| **Reaction 2.30**[2] | 1.34E+08 | 1.32E+08 | 1.30E+08 | 151 | |
| **Reaction 2.31** | | 1.00E+12 | | 185 | $G(1)$ |
| **Reaction 2.32** | | 1.80E+03 | | 36 | $G(1)$ |
| **Reaction 2.33**[2] | 1.34E+08 | 1.32E+08 | 1.30E+08 | 151 | |
| **Reaction 2.34** | | 6.00E+07 | | 168 | $G(2)$ |
| **Reaction 2.35** | | 1.10+05 | | 140 | $G(2)$ |

Where
$G(1) = (\theta_{ZC^*})^{2/3}$
$G(2) = (\theta_{ZC^*} + \theta_{ZC})^{2/3}$

$\lambda_{Surface^*}$ denotes the active site density on the reactive carbon atom. The shrinking core function $G(1)$ only accounts for the reactive carbon species while $G(2)$ includes both reactive and normal carbon species.

### 4.1.3 Simulation settings in catalyst brick

The axial discretization was set to 40 sub-volumes. The solver in the surface-reaction module was set to Advance Adaptive solver. The diffusion model was set to quasi-steady. Other parameters that are not mentioned were set to default value. Time step of 1 second was used in the simulation. The solver solved 9 state equations (3 species balances, 4 coverage balances, 1 momentum balance and 2 energy balances).

## 4.2 DPF Module Implementation

Simple global kinetics are used to model passive regeneration and $NO$ oxidation and the parameters (activation energy) was obtained from the analysis in Section 3.2.2.2 and 3.2.3.1. The Pt-catalyst loading is unknown and it is assumed to be 4 $g/ft^3$, which is equivalent to 0.724 $mol/m^3$ active sites. The active site density of the catalyst is accounted by multiplying into the rates constants for $NO$ oxidation. Pre-exponential factors were calibrated and the optimized kinetics parameters are presented in Table 4.7. A $CO$ selectivity factor of 0.17 was applied to account for the selectivity, even though it is unknown from the experimental data. The value of 17% was based on a publication that showed a range of 14-19% for $CO$ selectivity at temperatures between 200-400°C [57].

---

[2] Calculation presented in Appendix A.5

**Table 4.7:** Parameters for the Arrhenius constants in $NO$ oxidation and soot oxidation by $NO_2$

| | **Pre-exponential factor** | **Activation Energy (kJ/mol)** |
|---|---|---|
| **NO Oxidation** | 830 | 22 |
| $NO_2$ **Soot oxidation** | 3.65E7 | 86.8 |

Reproducing pressure drop was important to the kinetics modeling because it affects the space velocity and partial pressure of each species. Many of he filter properties are unknown and was assumed to be their typical values, see Table 4.8. The filter porosity was set to 0.5 and mean pore diameter of 15 $\mu m$. The analysis from Section 3.2.2.1 reduces the amount of adjustable parameters for the pressure drop model. The main parameters that were calibrated were the clean filter permeability and soot cake porosity. Other pressure drop contributions such as contraction and expansion effects are neglected and were set to 0.

**Table 4.8:** Physical filter properties that are used in the simulations.

| | **Units** | **Values** |
|---|---|---|
| **Clean Filter Wall Permeability** | $mm^2$ | 6.4E-8 |
| **Pore Diameter** | $\mu m$ | 15 |
| **Filter Porosity** | - | 0.5 |

### 4.2.1 Simulation settings in DPF

Different solver was used in the DPF, since the Advanced Adaptive solver is limited to catalyst brick. The numerical solver employed in the DPF module was the BDF solver. The number of axial discretization intervals was set to 40 sub-volumes and the substrate wall discretization was set to 5 units. The time step was set to 1 second. The simulation solved 11 state equations in total (6 species balances, 1 continuity balance, 1 momentum balance, 2 energy balances and 1 pressure drop model).

## 4.3 Detailed kinetics in DPF

One of the main objectives of this study is to implement detailed kinetics model in the DPF. Therefore, model 1 (parameters from Table 4.3) was implemented in the DPF module. However, due to limitations in GT-POWER detailed kinetics cannot be implemented directly. Instead, special implementation techniques are required to bypass this limitation. More details about the technique can be found in appendix B.

The carbon storage on active sites for catalyst brick is obsolete in the DPF module. Since the DPF module enables the storage of solid carbon on the soot cake and substrate layer. Therefore, the shrinking core term was converted to a function of local soot concentration $[C]_C^\eta$. The shrinking core functions were modified and implemented in the DPF. It is expressed as following:

$$G(1) = \left(C_{soot}\right)^{2/3}$$
$$G(2) = \left(C_{soot} + \theta_{CO_{ads}} \cdot \lambda_{surface}\right)^{2/3}$$

Where $C_{soot}$ is the local soot concentration.

### 4.3.1 Integrated Model implementation

At this point, the active and passive regeneration models were implemented in the DPF independently. They were combined together to form an integrated soot oxidation model (called integrated model). A process chart in GT-POWER is shown here to present the integrated model implementation 4.2.

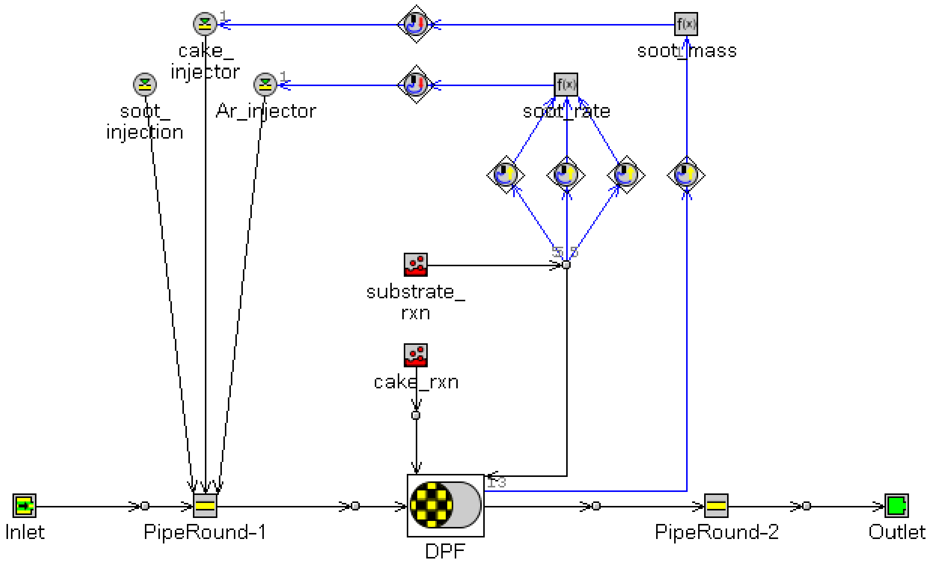

**Figure 4.2:** DPF Process Flow in GT-POWER

The simulation settings that was used for the integrated model were the same as in Section 4.2.1. However, more state equations were solved in the simulation, there were 19 state equations in total (6 species balances, 8 coverage balances, 1 continuity balance, 1 momentum balance, 2 energy balances and 1 pressure drop model).

# 5

# Results and Discussion

This chapter covers the results of the simulations using GT-POWER and the parameters from previous Section 4. Furthermore, sensitivity analysis is used to evaluate the parameters for considered models. Also, computational performance of the simulations is assessed by comparing the simulation time for different setups. Finally, the last part of this chapter will discuss suggestions for improvements of models and future work.

## 5.1 simulation results in monolith

The results show (in Figure 5.1) that model 1 and 2 are capable of capturing isothermal soot oxidation to some certain extents. The major second broad peak is greatly controlled by oxygen adsorption and the surface oxides coverage. These parameters affect the timing of the second peak. The second peak will occur earlier as a consequence of increased oxygen adsorption rate. Overall, the models have satisfactory fit with the high temperature cases and moderate fit with the reaction condition 580°C.

The reactions (2.26)-(2.29) in model 1 uses a combination of coverage species $O_{ads}$ and $CO_{ads}$ to create an initial rate-determining step. The identical effect has $O_{ads}$ on model 2. The degrees of freedom in these models are high. Therefore, the solution can be achieved with many different sets of parameters. The simulated coverage throughout the simulation is presented in Figure 5.2. Note the timing when the coverage species reach stable or maximum values. The timing is approximately the same as the occurrence of the second peak.

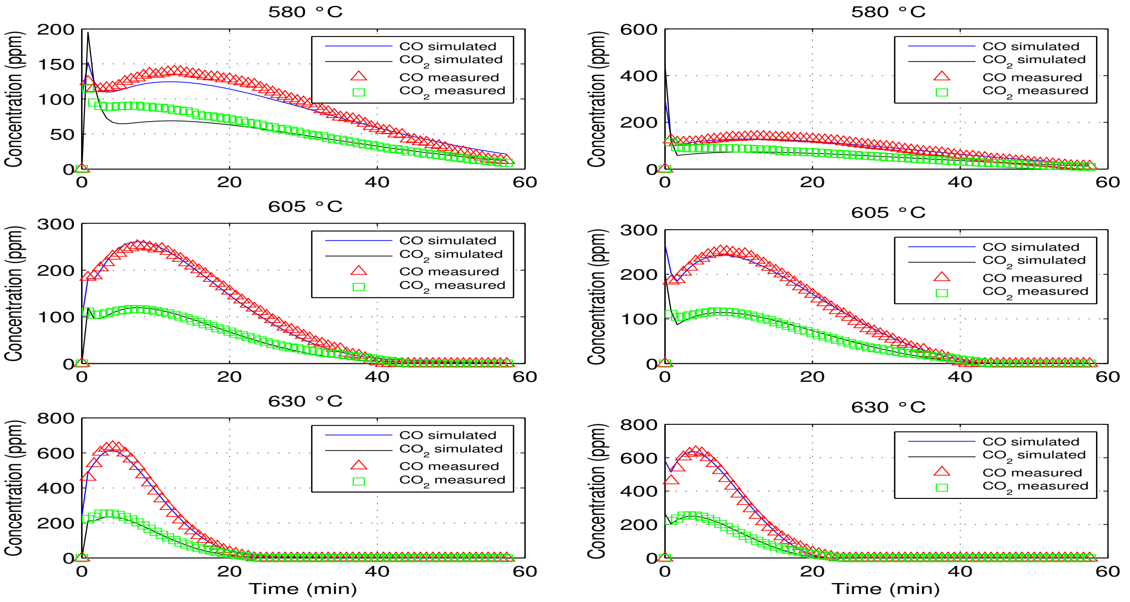

**Figure 5.1:** Left: Simulation result of the model 1. Right: Simulation result of the model 2.

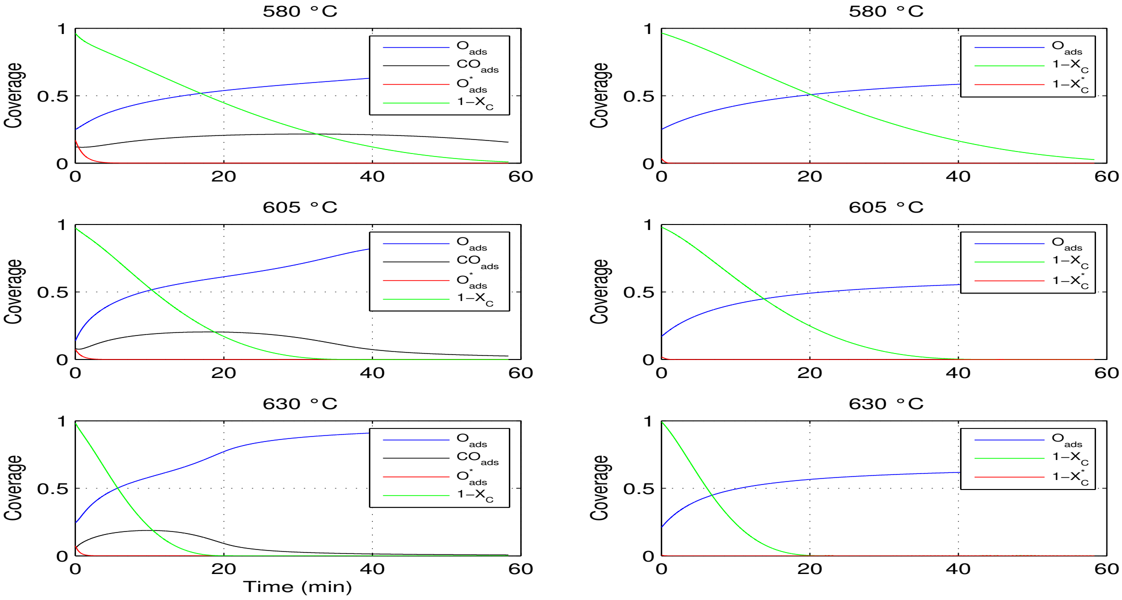

**Figure 5.2:** Left: simulation result of the model 1. Right: simulation result of the model 2.

These models consist of multiple activation energy which enables the option to model the selectivity change. As previously mentioned in Section 3.1.2, the selectivity changes over time for 580°C. The reactions are divided into two sets; fast and slow. Each set of reactions has individual kinetic parameters. The fast reactions with reactive species are able to produce the initial low selectivity of $CO$, which lasts until the reactive species are consumed, see Figure 5.3. One possible improvement of the fit for 580°C is to implement an additional carbon species that have activation energy value between the fast and slow reactions. A similar approach to multi-population kinetic models [43].

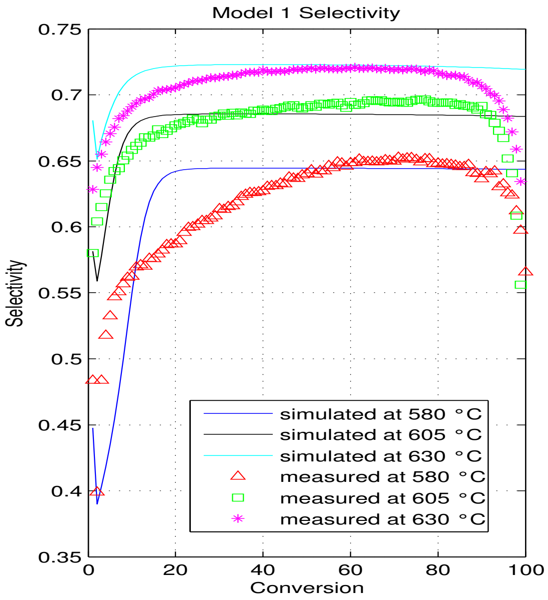

**Figure 5.3:** The simulated selectivity for model 1 and 2.

Detailed kinetics with only 2 sets of reactions are able to reduce the residue by approximately 25%, see Figure 5.4. The majority of the residue are found in the low conversion region (0-20%). In contrast, the models were able to handle most of the higher conversion region with the exception at conversion above 90%. The conclusion is that global kinetics and shrinking core are able to predict the soot oxidation from conversion 40% and above. The performance of model 1 and 2 are similar. The difference in errors in Figure is because of the more or less optimized models. Detailed kinetics have the potential to reduce the residue and the models still have room for improvement.

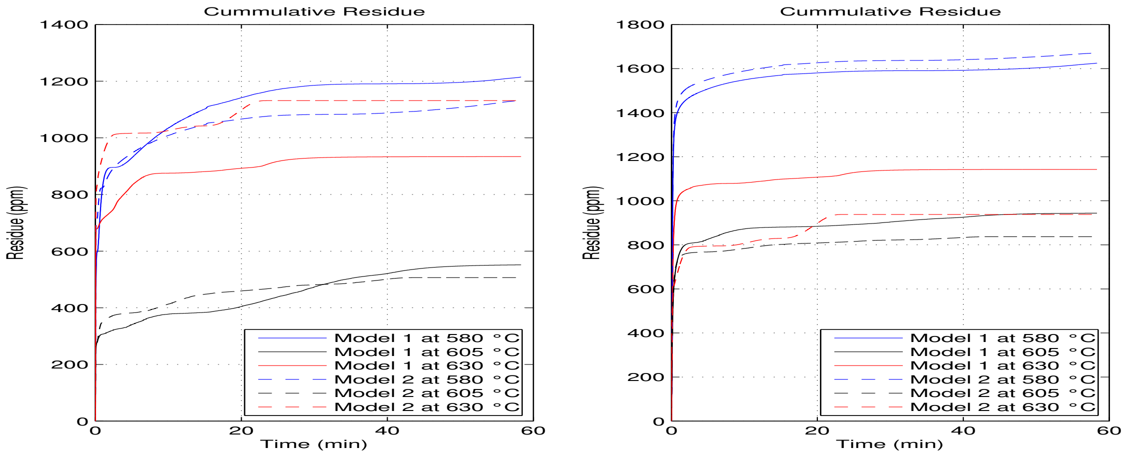

**Figure 5.4:** Left: cumulative error of model 1 and 2 with fast reaction. Right: without fast reaction to generate the sharp initial spike.

## 5.2 DPF simulation results

The $NO$ oxidation model was surprisingly effective for being a simple gas phase equilibrium reaction, see Figures in Appendix E and F. In reality, $NO$ oxidation is a heterogeneous surface reaction that interacts with the catalyst. Thus, the mechanism of $NO$ oxidation is much more complicated, e.g. involve surface coverage of the catalyst. The $NO$ oxidation model was able to explain at least 90% of the variance in the experiments.

The soot cake properties that were used to produce the pressure drop is reasonable and comparable to the literature values [19]. For simplicity reasons, the soot cake porosity was assumed to be constant. The value was chosen based on the fit for semi-steady state data. However, in reality, soot cake porosity should change over the conversion and might be different from case to case. This was evident in the transient simulations because a better fit was obtained with an increasing soot porosity. The $R^2$ for Transient 3 and 4 went from 0.5 to 0.88.
The values are presented in Table 5.1.

**Table 5.1:** Soot properties obtained from transient simulations. The soot cake density is a function of the soot cake porosity $\rho_{cake}=\rho_{soot}(1-\epsilon)$. where $\rho_{soot}$ is assumed to be the density of graphite 2000 $kg/m^3$. Note that the experiments were done consecutively, thus, it is reasonable that the soot cake porosity increases after each experiment.

| **Data set** | **Soot Cake Porosity** $\epsilon$ | **Soot Cake Density** ($kg/m^3$) |
|---|---|---|
| **Transient 1-2** | 0.7 | 600 |
| **Transient 3-6** | 0.85-0.97 | 60-300 |

Microstructural properties such as soot cake porosity are not only an interesting variable for pressure drop but also for soot oxidation as well. It can be utilized in the estimation of carbon sites (i.e shrinking core). However, no further modeling of soot cake porosity was conducted. The soot cake porosity was found to be increasing in the transient simulations. Thus, it was calibrated for best fit. The soot cake porosity is usually unknown but the obtained values agreed to the literature [19].

The soot oxidation model was based on the transient experiments. However, the model was unable to create similar pressure drop trend in the semi-steady state simulations. It was concluded that the soot oxidation was too slow. The pre-exponential factor has to be approximately three times higher than in the transient experiments. There are two explanations for this. Firstly, the difference in the generated soot in the experiments. Secondly, the pressure drop is not reliable to confirm the soot oxidation, since pore growth can potentially develop into channels in the soot cake and reduces the pressure drop non-linearly. The simulations with the adjusted pre-exponential factor for soot oxidation is presented in Appendix E. The corresponding pressure drop contribution is shown in Figure 5.5. The pressure drop contribution from the soot cake decreases around the balance point temperature which was discussed in Section 3.2.2.

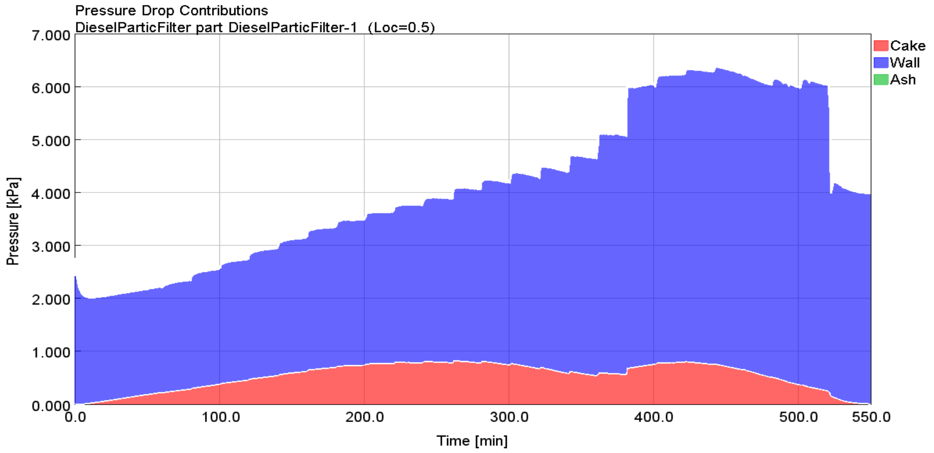

**Figure 5.5:** Simulated pressure drop contribution measured in middle of the DPF. It shows the pressure drop contribution decreases because of soot oxidation.

The predicted amount of soot in the substrate never exceeded 0.9 g/L for data set SS 2. The same assumption was made for soot loading parameters in the transient data sets. Since the data about the pre-loaded soot are missing. The amount of soot inside the filter wall is small which indicates the soot packing is not dense inside the wall. The value used in the simulation was 4.5 $kg/m^3$, which is small in contrast of graphite density 2000 $kg/m^3$. The soot cake porosity was found to be 0.7 which corresponds to a density of 600 $kg/m^3$ with the assumption that soot density is equal to graphite density. Typical values of soot cake porosity are 0.9-0.95, but, some other studies have shown 0.6 in porosity [19]. It would be ideal to conduct soot loading experiments to confirm some critical parameters such as clean filter permeability and loaded filter parameters for the pressure drop.

The pressure drop model was adequate to predict pressure drop at higher velocities above 2 $m/s$, see Figure 5.6 or the simulated results in Appendix E. The values that were used in the model was within the literature values. Critical values such as filter porosity and pore diameter can greatly influence the pressure drop contribution.

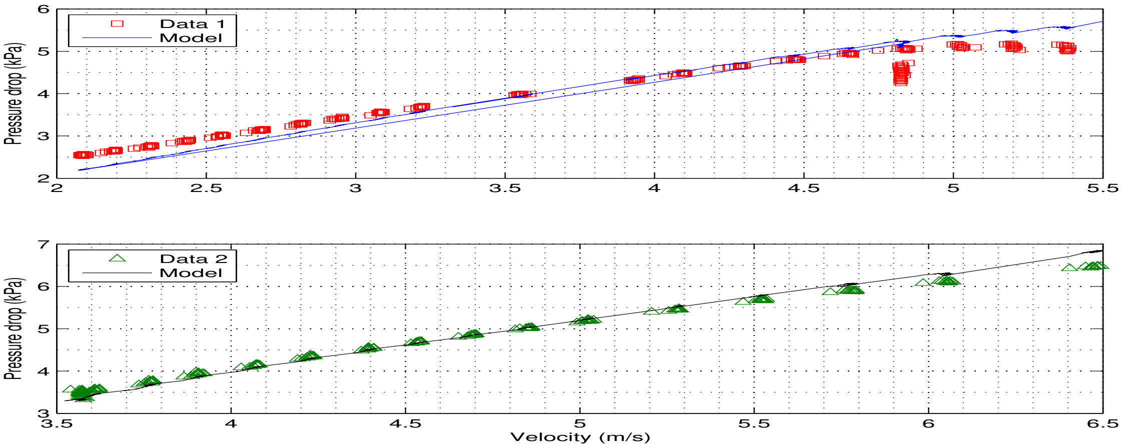

**Figure 5.6:** Pressure drop against velocity.

Compare the pressure drop in Figure E.1 and E.2. The sudden decrease in pressure drop is not proportional to the decrease in velocity in data SS 1, view velocity in figure 3.10. This observation cannot be captured with the current pressure model. The global kinetics model was able to approximately estimate the measured soot loading for the first three transient data sets with single digit cumulative error, see Table 5.2. The model overestimates the soot oxidation for data set Transient 4 had an error of 36.5%, which was equivalent to 2.55 g soot. The error can be shifted by changing the pre-exponential factors. A choice was made to weight the error to the last experiment. The errors in this range are acceptable because the measurements also contained uncertainties and errors. Since the soot mass was measured as the difference in total weight before and after. Whereas the weight of the DPF is approximately 30 kg and the weighted values are in grams. It is reasonable to believe that the measurements of soot mass are uncertain.

**Table 5.2:** Simulated soot loadings compared to measured

| Inital soot load (g/L) | Simulated (g/L) | Measured (g/L) | Error (%) |
|---|---|---|---|
| 4.811 | 4.229 | 4.316 | 2.6 |
| 4.316 | 3.924 | 4.092 | 4.1 |
| 4.092 | 1.001 | 0.989 | 1.2 |
| 0.989 | 0.200 | 0.315 | 36.5 |

## 5.3 Sensitivity analysis

The sensitivity analysis was conducted by using full factorial experimental design with ±5% parameter's value [60]. The response parameter is the cumulative error. The fast and slow reaction interactions are assumed to be negligible. Hence, the reactions were decoupled to reduce the number of simulations. The error bars in Figure 5.8 shows the corresponding confidence interval with the significant level of 0.05.

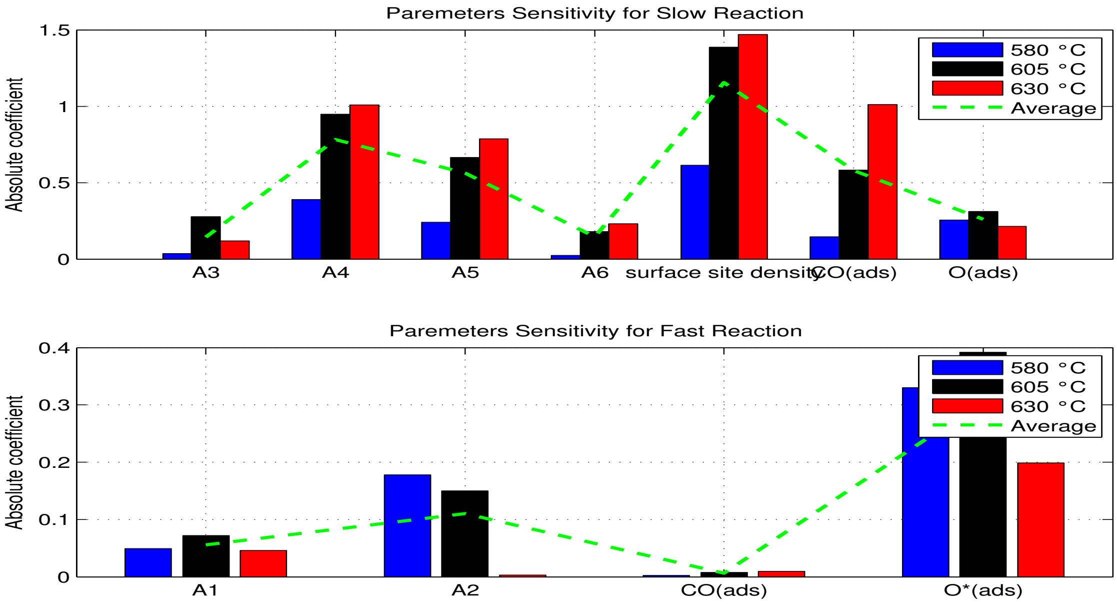

**Figure 5.7:** Top: sensitivity of parameters in model 1 for slow reaction set. Bottom: sensitivity of parameters in model 1 for fast reaction set. The confidence interval was relatively small. Thus, it was not included.

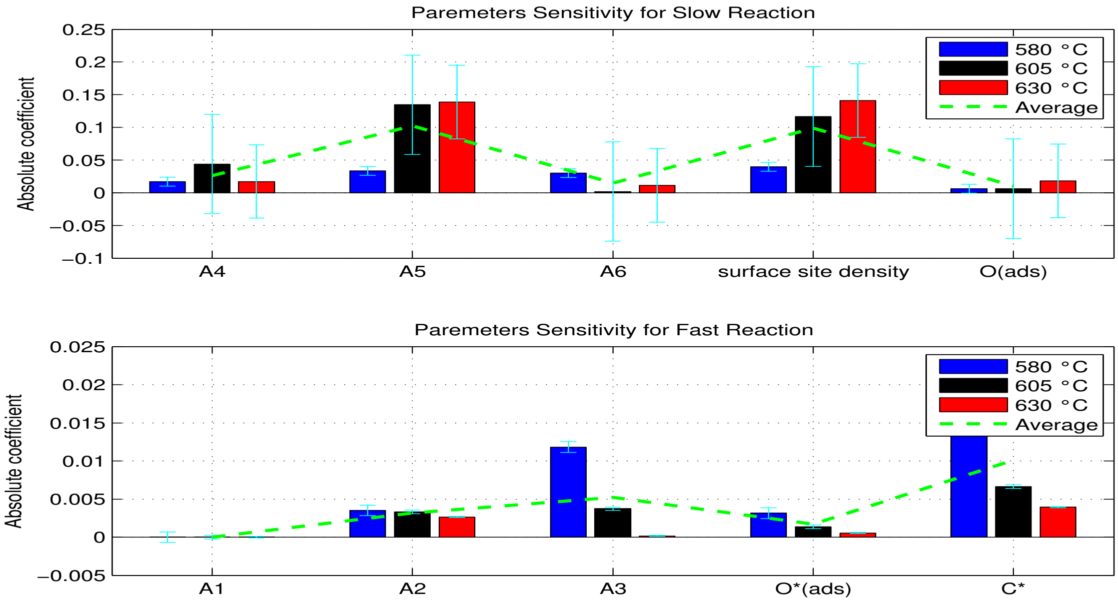

**Figure 5.8:** Top: sensitivity of parameters for each temperature in model 2 for slow reaction set. Bottom: sensitivity of parameters for each temperature in model 2 for fast reaction set.

The results show that the surface active site density has great impact on model 1.The estimation of this parameter is crucial. Recall from Appendix A.3 that this parameter was calculated based on the assumption that a single active site has the size of 8 $\forall^2$. Hence, it is essential to investigate the parameters through experiments.

Furthermore, the sensitivity analysis shows that the parameters in reaction (2.27), (2.28), and initial coverage of $CO_{ads}$ are significant and important parameters, see Figure 5.7.

The initial coverage of $O^*_{ads}$ in the fast reactions was found to be a sensitive parameter. while the other parameters have a much lower effect on the model. Again, experiments on the surface of soot discussed in the last paragraph are needed to confirm this observation.

In model 2, the effect of many parameters responsible for the slow reaction is statistically insignificant except for reaction (2.33) and the active site density. This implies that the oxygen absorption step is only a temporarily rate-determining step. Hence, the parameters are relatively insensitive compared to the transitioned rate-determining reaction (2.33). Therefore, model 2 can be seen as a combination of the global kinetics model and an additional function to shape the second peak. These observations suggest that model 2 is basically an extension of the global kinetics model. The sensitivity analysis for the fast reaction is similar to model 1. The main effect comes from the amount of initial reactive carbon. Therefore, it can be concluded that both approaches are effective and yield similar behavior for the fast reaction.

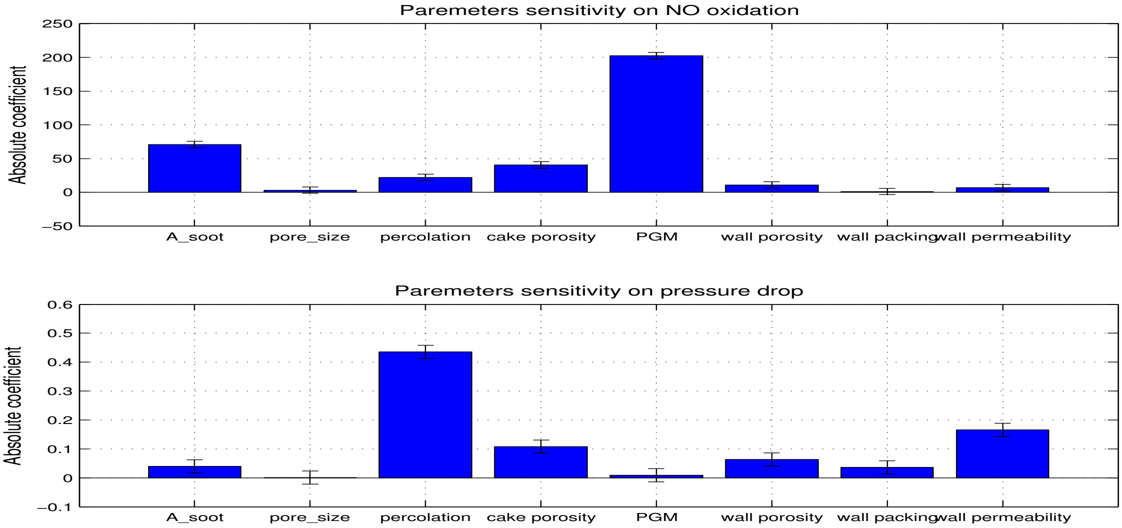

**Figure 5.9:** Top: parameter sensitivity on $NO$ oxidation. Bottom: parameter sensitivity on pressure drop.

The sensitivity analysis of the DPF models focused on selected parameters that were believed to have an effect on $NO$ oxidation model and pressure drop model. The analysis was done on the Transient 3 data and the number of investigated parameters was 8. Among these parameters are pre-exponential factor of soot oxidation, filter pore diameter, percolation constant, soot cake porosity, PGM, filter porosity, soot packing density in the wall, and clean wall permeability respectively. The result shows that $NO$ oxidation is sensitive to the catalyst loading, increasing the catalyst loading favors the soot oxidation performance.

Percolation constant was found to have a strong effect on the pressure drop model. This is as expected since this parameter controls the distribution of inlet soot to the filter wall or soot cake which indirectly affect the pressure drop. The soot oxidation seems to have relatively small effect on the pressure drop compared to other parameters (percolation constant, wall permeability and soot porosity). Since the pressure drop contribution from the soot cake is actually smaller compared to the filter's pressure drop contribution, see Figure 5.5. This can also be explained by the $NO$ oxidation parameters have a weak effect on the pressure drop, because the soot oxidation already has a weak effect on pressure drop.

## 5.4 Simulation performance

One of the objectives of this thesis is to investigate the performance of GT-POWER in soot oxidation reaction. Computational time was used as a performance measurement and compared in the Table 5.3. It is obvious that the choice of solver significantly affects the simulation time. Interestingly, the Advanced Adaptive solver provides more accurate prediction and requires less computational time, in comparison with other solvers such as BDF and Adaptive-RK. The details about the solver's algorithm cannot be examined because GT-POWER keeps the algorithm as a secret. Advanced Adaptive uses dynamic time step which is more appropriated to the problem at any given time. This is proven to be the case. Therefore, it is concluded that Advanced Adaptive solver has superior performance for kinetics modeling and it is recommended as the default solver.

**Table 5.3:** Simulation performance with different solver in isothermal experiment condition

| **Case** | Active soot oxidation by $O_2$ in catalyst brick (sequential run for 3 temperature levels) | | | | | |
|---|---|---|---|---|---|---|
| **Model** | 1 | | | 2 | | |
| **Experiment time (s)** | 3500 | | | | | |
| **Step size (s)** | 1 | | | | | |
| **Number of step** | 3500 | | | | | |
| **Number of discretized volume** | 80 | | | | | |
| **Solver** | AA | BDF | Adaptive -RK | AA | BDF | Adaptive -RK |
| **Simulation time (s)** | 8.35 | 148.19 | 532.10 | 25.41 | 162.76 | 574.47 |
| **Normalized error** | 1 | 11.19 | 11.196 | 1.159 | 11.23 | 11.229 |

Where AA denotes Advanced Adaptive solver.

The integrated model was conducted with the same transient inputs from the transient experiments with the temperature range from 170-340°C, see Table 5.4 to see the performance. The solver used in this case was BDF solver since DPF simulations are limited to RK-RADAU or BDF solvers. No data was available to validate the integrated model. However, a small difference in soot oxidation was observed in comparison to the regular DPF model with passive regeneration. This is obvious because active regeneration is insignificant at low temperatures. Also, another difference was the simulation time, which took about 4 times longer to finish, in comparison to the passive regeneration DPF model. Since the integrated model adds 8 additional state equations to the original 11 state equations. Therefore, the increase in simulation time reflects the number of unknown variables. Apparently, the simulation time seems to be quadratic dependent on the number of unknown variables. Interestingly, simulations with only 10 discretized sub-volumes gave the same result. Therefore, the simulation is grid-independent using 10 discretization intervals. Hence, computational time can be spared by reducing the number of sub-volume.

**Table 5.4:** Simulation performance in DPF module of passive regeneration model and integrated mode.

| Case | Soot oxidation by $NO_2$ in DPF, transient engine input, pre-loaded soot | | | | | | | |
|---|---|---|---|---|---|---|---|---|
| Model | $NO_2$ oxidation | | | | Integrated model (Model 1 and $NO_2$ oxidation) | | | |
| Experiment time (s) | 10805 | | 10934 | | 10805 | | 10934 | |
| Step size (s) | 1 | | | | | | | |
| Number of step | 10805 | | 10934 | | 10805 | | 10934 | |
| Number of discretized volume | 40 | | | | | | | |
| Number of discretized soot layer | 5 | | | | | | | |
| Solver | BDF | | | | | | | |
| Simulation time (s) | 293 | 283 | 294 | 296 | 1320 | 1364 | 1448 | 1358 |
| Target soot (g) | 96 | 91 | 22 | 7 | 96 | 91 | 22 | 7 |
| Soot retained (g) | 95.4 | 88.75 | 25.0 | 5.97 | 95.4 | 88.74 | 24.81 | 5.91 |

## 5.5 Model improvements and future work suggestions

In the current work, model 1 and 2 are good candidates to predict the soot oxidation. However, there is still room for improvements of these models. One of the most important aspects in these models is their reactive species. The question about their formation and what are they in reality are still open for discussion. In these models, they are assumed as reactive carbon or oxygen for modeling convenience . In reality, they are most likely functional groups attached to the carbon or carbon surface topology, which cause different reactivity in soot oxidation. In model 1 the reactive oxygen species $O^*_{ads}$ should be redefined as reactive surface oxide complex $CO^*_{ads}$. However, a similar modification is not possible for the lumped model 2. Since GT-POWER only identifies one type of solid phase soot in the reaction.

Wang-Hansen et al. observed initial high reactivity when oxidizing soot after exposing it to ambient air overnight [16]. This suggests that the reactive species can be formed and regenerated spontaneously. However, the formation of these reactive species is relatively slow. Model 1 and its simulation can be easily modified to convert the surface oxide complexes $CO_{ads}$ to reactive ones $CO^*_{ads}$ (i.e.: $CO_{ads} \rightarrow \mathrm{CO}^*_{ads}$) . Obviously, reaction (2.24) and (2.25) has to be modified as well. The transition can either be in the presence of $O_{ads}$ or gas phase oxygen.

The oxygen adsorption rate in reaction (2.26) was merely tasked to create the second peak. The second peak of $CO_2$ is actually not in sync with the $CO$ peak, see Figure 3.1. This suggests a decoupled rate-determining step, which is the opposite of the models. A probable improvement is introducing an additional adsorbed oxygen species or an additional type of active sites. Since the formation of $CO/CO_2$ mechanism is different. That is evident for $CO/CO_2$ formation with different oxygen isotopes [35].

There were problematic issues when implementing the oxygen adsorption step in the DPF module, because adsorption reactions were not allowed in the soot cake. A possible solution is to numerically imitate oxygen absorption step in the models. This can be done by using a look-up table to generate a mathematical function that is similar to the surface coverage $\theta_O$. Such approach can be implemented on the global kinetics model and improve its performance. However, it is an empirical solution and it might be unsuitable for other reaction conditions.

The detailed kinetics of soot oxidation by $NO_2$ would be an interesting topic for future work. Similar reactivity trends were observed in soot oxidation by $NO_2$ [57]. Therefore, an adoption of elementary step mechanism ought to be applicable. A potential mechanism was proposed by Muckenhuber et al. [9].

$$NO_2 + s \rightarrow NO_{2_{ads}} \tag{5.1}$$

$$C + NO_{2_{ads}} \rightarrow CO + O_{ads} + NO \tag{5.2}$$

Where $NO_2$ is adsorbed to the carbon surface which reacts further with a carbon element forming $CO$, $NO$ and $O_{ads}$. The adsorbed oxygen $O_{ads}$ is the same one from model 1 and 2. It is reported that soot oxidation with $O_2$ and $NO_2$ have a cooperative interaction [8]. This extension might be able to account for the cooperative interaction and advance the catalyzed DPF model.

The pressure drop and deep filtration model can be improved by coupling with the detailed soot oxidation kinetics. The porosity of soot cake could be modeled depending on the particle morphology, pore size, etc. [19]. The porosity can be useful to predict the change in active site density on carbon. Thus, it might improve the shrinking core model.

# 6

# Conclusion

In the development of detailed kinetics for soot oxidation, different data treatment approaches were used in order to find critical parameters for the models. From estimating reactive species to Arrhenius plot analysis. These types of analysis are efficient to find reasonable parameter range and they were useful in the simulations.

Two similar models for oxygen soot oxidation were investigated in this work. The first model used reactive surface site species with two rate determining steps. The second model assumes the presence of additional reactive carbon family with its own rate-determining step. Both of these models were able to capture initial high reactivity low conversion and broad peak afterward well. However, they were unable to capture the change in $CO/CO_2$ selectivity at low carbon conversion for 580. A potential improvement to that is adding an additional carbon species with another set of activation energy that is between the fast and slow reactions. This will introduce more degrees of freedom. But caution is needed when adding more reactions and parameters without any basis might over-fit the model.

The Arrhenius plots show that kinetics parameters also vary with carbon conversion and the exact kinetic parameters are still inconclusive. Optimization for kinetics parameters shows that there are more than one set of parameters that yields ‘good’ solution. The reaction order on the shrinking core has a significant effect on the reaction rate of $CO/CO_2$. The value within the range of 2/3 to 1 shows promising results. These models significantly outperform global kinetics in low conversion region.

Analysis of pressure drop and $NO$ oxidation in the engine data was performed in the development of a DPF model. The data was not designed to investigate the detailed kinetics of soot oxidation by $NO_2$ but the measurements of the soot mass could roughly approximate the parameters for the global kinetic model. The analysis of deep filtration and clean filter permeability was able to provide valuable parameters for the simulations. The pressure drop model was adequate to predict the pressure drop in the experiments, It is arguable if the pressure drop is reliable to determine the soot oxidation. Because the soot oxidation in the semi-steady state experiments was approximately three times faster in order to obtain similar pressure drop trend as the experimental data. Different soot cake porosity was obtained in the transient data, a reasonable trend was found; the soot porosity increases with the conversion of soot.

$NO_x$ measurements was used as a second opinion to validate the global kinetics model of soot oxidation by $NO_2$, but caution was taken since the $NO$ oxidation also occurs at the wash-coated outlet channels in DPF. It might affects the $NO_2/NO_x$ ratio and as a consequence carbon consumption might be underestimated.

Overall, GT-POWER is an easy-to-use platform to simulate kinetics model but not flexible for complex reaction mechanism in the DPF. Straightforward implementation was not possible since the DPF module only supports global kinetics. GT-POWER also prohibits adsorption and desorption reactions in the soot cake. Implementation techniques were developed in order to override the limitations. The techniques operated flawlessly. However, it might encounter more issues with other modeling and fall short in the long term usage. A temporary solution was suggested; use a look-up table to convert the oxygen absorption step a mathematical function which can be applied global kinetics rate expressions. The approach is empirical but it will practically eliminate the implementation difficulties in the DPF module.

The integrated kinetics model is a combination of the developed models (active and passive regeneration) together without accounting for cooperative interactions between them. However, the integrated model is limited because the parameters origin from Printex-U and diesel soot. Even though Printex-U is used to model the soot oxidation for real soot, it has totally different kinetic parameters [21]. However, the model can be calibrated towards diesel soot if data is available.

Improvements of the current models were suggested but also suggestions about possible extensions of the current work. First of all, improvements of the fast reaction set in model 1 and 2 by investigating the formation of reactive species. Secondly, account the individual rate-determining for $CO$ and $CO_2$ formation. Thirdly, integrate the pressure model and deep filtration model with the detailed kinetic that might find soot properties and soot morphology, which can be useful to improve the shrinking core model. Finally, include detailed kinetics of soot oxidation by $NO_2$ that may account for the cooperative interaction between soot oxidation by $O_2$ and $NO_2$.

# References

[1] *Emission standards*. Accessed: 2nd February 2016. URL: `http://www.dieselnet.com/standards/eu/hd.php`.

[2] B. Lundberg. “Aspects of efficient parameter estimation for diesel oxidation catalysts”. PhD-thesis. Chalmers University of Technology, 2015.

[3] S. R. Katare and P. M. Laing. “Hydrogen in Diesel Exhaust: Effect on Diesel Oxidation Catalyst Flow Reactor Experiments and Model Predictions”. *SAE International Journal of Fuels and Lubricants* 2.1 (2009), pp. 605–611.

[4] K. C. Premchand, K. Raghavan, and J. H. Johnson. “A Modeling Study of the Exhaust Flow Rate and Temperature Effects on the Particulate Matter Thermal Oxidation Occurring during the Active Regeneration of a Diesel Particulate Filter”. *SAE Technical Paper* (Apr. 2015). URL: `http://dx.doi.org/10.4271/2015-01-1044`.

[5] I. Nova and E. Tronconi. *Urea-SCR Technology for deNOx After Treatment of Diesel Exhausts*. 1;2014; New York, NY: Springer New York, 2014.

[6] S. B. Simonsen, S. Dahl, E. Johnson, and S. Helveg. “Ceria-catalyzed soot oxidation studied by environmental transmission electron microscopy”. *Journal of Catalysis* 255.1 (2008), pp. 1–5.

[7] *Diesel Filter Regeneration*. `http://www.dieselnet.com/dpf_regen.php`. Accessed: 9th February 2016.

[8] M. Jeguirim, V. Tschamber, J. F. Brilhac, and P. Ehrburger. “Interaction mechanism of NO 2 with carbon black: effect of surface oxygen complexes”. *Journal of Analytical and Applied Pyrolysis* 72.1 (2004), pp. 171–181.

[9] H. Muckenhuber and H. Grothe. “The heterogeneous reaction between soot and NO 2 at elevated temperature”. *Carbon* 44.3 (2006), pp. 546–559.

[10] B. R. Stanmore, J. F. Brilhac, and P. Gilot. “The oxidation of soot: a review of experiments, mechanisms and models”. *Carbon* 39.15 (2001), pp. 2247–2268.

[11] *Continously Regeneration Trap ((C)CRT©systems*. `http://www.jmdpf.com/diesel-exhaust-filter-system-CRT-NRMM-johnson-matthey`. Accessed: 17th may 2016.

[12] Y. Li, M. Weinstein, and S. Roth. "NO oxidation on catalyzed soot filters". *Catalysis Today* 258 (2015), pp. 396–404.

[13] R. H. Hurt and B. S. Haynes. "On the origin of power-law kinetics in carbon oxidation". *Proceedings of the Combustion Institute* 30.2 (2005), pp. 2161–2168.

[14] B. A. A. L. van Setten, M. Makkee, and J. A. Moulijn. "Science and technology of catalytic diesel particulate filters". *Catalysis Reviews* 43.4 (2001), pp. 489–564.

[15] P. Carlsson. "Detailed modeling of carbon oxidation". *Journal of Physical Chemistry C* 116.16 (2012), pp. 9063–9071.

[16] C. Wang-Hansen, C. J. Kamp, M. Skoglundh, B. Andersson, and P. Carlsson. "Experimental Method for Kinetic Studies of Gas–Solid Reactions: Oxidation of Carbonaceous Matter". *J. Phys. Chem. C The Journal of Physical Chemistry C* 115.32 (2011), pp. 16098–16108.

[17] C. Arnal, M. U. Alzueta, A. Millera, and R. Bilbao. "Experimental and kinetic study of the interaction of a commercial soot with NO at high temperature". *Combustion Science and Technology* 184.7-8 (2012), pp. 1191–1206.

[18] R. Dominik and B. Thorsten. "Different Approaches to Soot Estimation as Key Requirement for DPF Applications" (Apr. 2009). DOI: `10.4271/2009-01-1262`. URL: `http://dx.doi.org/10.4271/2009-01-1262`.

[19] A. G. Konstandopoulos, E. Skaperdas, and M. Masoudi. "Microstructural Properties of Soot Deposits in Diesel Particulate Traps". *SAE Technical Paper* (Mar. 2002). URL: `http://dx.doi.org/10.4271/2002-01-1015`.

[20] E. A. Kladopoulou, S. L. Yang, J. H. Johnson, G. G. Parker, and Athanasios G. Konstandopoulos. "A Study Describing the Performance of Diesel Particulate Filters During Loading and Regeneration - A Lumped Parameter Model for Control Applications". *SAE Technical Paper* (Mar. 2003). URL: `http://dx.doi.org/10.4271/2003-01-0842`.

[21] J. P. A. Neeft, T. X. Nijhuis, E. Smakman, M. Makkee, and J. A. Moulijn. "Kinetics of the oxidation of diesel soot". *Fuel* 76.12 (1997), pp. 1129–1136.

[22] V. P. Zhdanov, P. Carlsson, and B. Kasemo. "Kinetics of oxidation of nm-sized soot spherules". *Chemical Physics Letters* 454.4-6 (2008), pp. 341–344.

[23] M. Schejbal, J. Štěpánek, M. Marek, P. Kočí, and M. Kubíček. “Modelling of soot oxidation by NO 2 in various types of diesel particulate filters”. *Fuel* 89.9 (2010), pp. 2365–2375.

[24] A. Mayer. *Particle Filter Retrofit for All Diesel Engines*. Fachbuch. expert-Verlag, 2008. ISBN: 9783816928508. URL: `https://books.google.se/books?id=kxxGpt9zKTwC`.

[25] E. Tronconi, I. Nova, C. Ciardelli, D. Chatterjee, B. Bandl-Konrad, and T. Burkhardt. “Modelling of an SCR catalytic converter for diesel exhaust after treatment: Dynamic effects at low temperature”. *Catalysis Today* 105.3 (2005), pp. 529–536.

[26] M. E. Myers, J. Stollsteimer, and A. M. Wims. “Determination of hydrocarbon-type distribution and hydrogen/carbon ratio of gasolines by nuclear magnetic resonance spectrometry”. *Analytical Chemistry* 47.12 (1975), pp. 2010–2015.

[27] R. H. Hurt and J. M. Calo. “Semi-global intrinsic kinetics for char combustion modeling”. *Combustion and Flame* 125.3 (2001), pp. 1138–1149.

[28] A. Messerer, R. Niessner, and U. Pöschl. “Comprehensive kinetic characterization of the oxidation and gasification of model and real diesel soot by nitrogen oxides and oxygen under engine exhaust conditions: Measurement, Langmuir–Hinshelwood, and Arrhenius parameters”. *Carbon* 44.2 (2006), pp. 307–324.

[29] R. O. Lussow, F. J. Vastola, and P. L. Walker. “Kinetics of oxygen interaction with graphon between 450 and 675°C”. *Carbon* 5.6 (1967), pp. 591–602.

[30] T. Ishiguro, N. Suzuki, Y. Fujitani, and H. Morimoto. “Microstructural changes of diesel soot during oxidation”. *Combustion and Flame* 85.1-2 (1991), pp. 1–6.

[31] C. J. Tighe, M. v. Twigg, A. N. Hayhurst, and J. S. Dennis. “The kinetics of oxidation of Diesel soots by NO2”. *Combustion and Flame* 159.1 (2012), pp. 77–90.

[32] H. Jung, D. B. Kittelson, and M. R. Zachariah. “Kinetics and visualization of soot oxidation using transmission electron microscopy”. *Combustion and Flame* 136.4 (2004), pp. 445–456.

[33] B. S. Haynes and T. G. Newbury. “Oxyreactivity of carbon surface oxides”. *Proceedings of the Combustion Institute* 28.2 (2000), pp. 2197–2203.

[34] T. C Brown, A. E. Lear, C. Ma, and B. S. Haynes. *Fundamental Issues in Control of Carbon Gasification Reactivity*. expert-Verlag, 1991. Chap. Surface Complexes on Carbon During Oxidation and Gasification, pp. 307–328.

[35] B. S. Haynes and T. G. Newbury. “Oxyreactivity of carbon surface oxides”. *Proceedings of the Combustion Institute* 28.2 (2000), pp. 2197–2203.

[36] M. E. Davis, R. J. Davis, and Knovel (e-book collection). *Fundamentals of chemical reaction engineering*. Dover. Mineola, N.Y: Dover Publications, 2012.

[37] Z. Du, A. F. Sarofim, J. P. Longwell, and C. A. Mims. "Kinetic measurement and modeling of carbon oxidation". *Energy Fuels* 5.1 (1991), pp. 214–221.

[38] J. Hong, W.C. Hecker, and T.H. Fletcher. "Modeling high-pressure char oxidation using langmuir kinetics with an effectiveness factor". *Proceedings of the Combustion Institute* 28.2 (2000), pp. 2215–2223. ISSN: 1540-7489.

[39] K. Leistner. "Experimental and Modelling Study of Catalytic Diesel Soot Oxidation". PhD-Theses. Université Pierre et Marie Curie - Paris VI, May 2012. URL: `https://tel.archives-ouvertes.fr/tel-00858763`.

[40] W. J. Ceyrolles, P. Viot, and J. Talbot. "Kinetics of Heterogeneous Adsorption: Mean-Field Theory and Simulations". *Langmuir* 18.4 (2002), pp. 1112–1118.

[41] S. Ahmed, M. H. Back, and J. M. Roscoe. "A kinetic model for the low temperature oxidation of carbon: I". *Combustion and Flame* 70.1 (1987), pp. 1–16.

[42] C. J. Kamp, B. Andersson, Chalmers University of Technology, Chalmers tekniska högskola, Department of Chemical, and Chemical Reaction Engineering Biological Engineering. "The Role of Active Sites in the Non-Catalytic Oxidation of Carbon Particulate Matter: A Theoretical Approach". *Topics in Catalysis* 52.13-20 (2009), pp. 1951–1956.

[43] G. Kastrinaki, S. Lorentzou, and A. G. Konstandopoulos. "Soot Oxidation Kinetics of Different Ceria Nanoparticle Catalysts". *Emission Control Science and Technology* 1.3 (2015), pp. 247–253.

[44] V. Bacher, C. Perbandt, M. Schwefer, R. Siefert, and T. Turek. "Kinetics of the NO/NO2 equilibrium reaction over an iron zeolite catalyst". *Applied Catalysis B: Environmental* 134-135 (2013), pp. 55–59.

[45] J. B. Butt. *Reaction kinetics and reactor design*. Prentice-Hall, 1980.

[46] Gamma Technologies LLC. *Exhaust Aftertreatment Application Manual*. 2016.

[47] E. Fuller, P. Schettler, and J. C. Giddings. "NEW METHOD FOR PREDICTION OF BINARY GAS-PHASE DIFFUSION COEFFICIENTS". *Industrial Engineering Chemistry* 58.5 (1966), pp. 18–27.

[48] N. Mladenov, J. Koop, S. Tischer, and O. Deutschmann. "Modeling of transport and chemistry in channel flows of automotive catalytic converters". *Chemical Engineering Science* 65.2 (2010), pp. 812–826.

[49] A. G. Konstandopoulos, M. Kostoglou, E. Skaperdas, E. Papaioannou, D. Zarvalis, and E. A. Kladopoulou. "Fundamental Studies of Diesel Particulate Filters: Transient Loading, Regeneration and Aging" (Mar. 2000). DOI: `10.4271/2000-01-1016`. URL: `http://dx.doi.org/10.4271/2000-01-1016`.

[50] G. H. Juncu, V. Lavric, and R. Mihail. "A comparison between the insensitive Runge—Kutta, the semi—implicit extrapolation and the backward differencing methods in solving the ODE systems which describe the radical hydrocarbons pyrolysis". *Computers Chemical Engineering* 13.9 (1989), pp. 1075–1079. DOI: `10.1016/0098-1354(89)87048-6`.

[51] D. Duong. Do. *Adsorption Science and Technology*. 2000. ISBN: 9789814493376.

[52] I. W. Smith. "The intrinsic reactivity of carbons to oxygen". *Fuel* 57.7 (1978), pp. 409–414.

[53] K. Otto, M. H. Sieg, M. Zinbo, and L. Bartosiewicz. "The Oxidation of Soot Deposits from Diesel Engines" (Feb. 1980). URL: `http://dx.doi.org/10.4271/800336`.

[54] K. J. Higgins, H. Jung, D. B. Kittelson, J. T. Roberts, and M. R. Zachariah. "Kinetics of diesel nanoparticle oxidation". *Environmental science technology* 37.9 (2003), pp. 1949–1954.

[55] A. F. Ahlström, C. U. I. Odenbrand, Department of Chemical Engineering, LTH Faculty of Engineering, Lunds universitet, Institutioner vid LTH, Lunds Tekniska Högskola, Departments at LTH, Lund University, and Institutionen för kemiteknik. "Combustion characteristics of soot deposits from diesel engines". *Carbon* 27.3 (1989), pp. 475–483.

[56] C. Wang-Hansen, S. Soltani, B. Andersson, Chalmers University of Technology, Department of Chemical, and Chemical Reaction Engineering Biological Engineering. "Kinetic analysis of O2- and NO2-based oxidation of synthetic soot". *Journal of Physical Chemistry C* 117.1 (2013), p. 522.

[57] M. Ahmadinejad, A. Tsolakis, J. M. Becker, C. F. Goersmann, A. D. Newman, and T. C. Watling. "Modelling of Soot Oxidation by NO2 in a Diesel Particulate Filter". *SAE Int. J. Fuels Lubr.* 5 (Aug. 2011), pp. 359–369. DOI: `10.4271/2011-01-2083`. URL: `http://dx.doi.org/10.4271/2011-01-2083`.

[58] M. Lapuerta, F. J. Martos, and J. M. Herreros. "Effect of engine operating conditions on the size of primary particle composing diesel soot agglomerates". *Journal of Aerosol Science* 38.4 (2007), pp. 455–466.

[59] L. Labecki, A. Lindner, W. Winklmayr, R. Uitz, R. Cracknell, and L. Ganippa. "Effects of injection parameters and EGR on exhaust soot particle number-size distribution for diesel and RME fuels in HSDI engines". *Fuel* 112 (2013), p. 224.

[60] J. Sjöblom. "Parameter estimation in heterogeneous catalysis". PhD-thesis. Chalmers University of Technology, 2009.

[61] F. Gruvnäs. "Modellering av åldring av dieseloxidationskatalysatorer". MA thesis. KTH, School of Chemical Science and Engineering (CHE), 2015, p. 48.

[62] A. G. Konstandopoulos, E. Skaperdas, and M. Masoudi. "Microstructural Properties of Soot Deposits in Diesel Particulate Traps". *SAE Technical Paper Series* (2002).

[63] J. L. Ambs and B. T. McClure. "The Influence of Oxidation Catalysts on NO2 in Diesel Exhaust" (Sept. 1993). URL: `http://dx.doi.org/10.4271/932494`.

[64] B. Gadzhiev Oleg, S. K. Ignatov, S. Gangopadhyay, A. E. Masunov, and A. I. Petrov. "Mechanism of Nitric Oxide Oxidation Reaction (2NO + O2 → 2NO2) Revisited". *Journal of chemical theory and computation* 7.7 (2011), p. 2021.

[65] E. Hairer and G. Wanner. *Solving Ordinary Differential Equations II: Stiff and Differential-Algebraic Problems*. Second Revis. Vol. 14. Berlin, Heidelberg: Springer Berlin Heidelberg, 1996.

[66] J. Fjällman. *GT-POWER Report*. 2013. URL: `https://www.diva-portal.org/smash/get/diva2:624472/FULLTEXT01.pdf`.

[67] S. K. Bhatia and D. D. Perlmutter. "A random pore model for fluid-solid reactions: I. Isothermal, kinetic control". *AIChE Journal AIChE J.* 26.3 (1980), pp. 379–386.

[68] E. A. Kladopoulou, S. L. Yang, J. H. Johnson, G. G. Parker, and A. G. Konstandopoulos. "A Study Describing the Performance of Diesel Particulate Filters During Loading and Regeneration - A Lumped Parameter Model for Control Applications". *SAE Technical Paper Series* (Mar. 2003). DOI: `10.4271/2003-01-0842`.

# A

# Appendix - Parameter Calculation

## A.1 Pressure drop parameters and calibration

It is recommended to calibrate the pressure drop parameter with clean filter data (experiment on DPF without soot deposited or injection) but only soot injection data was available in this thesis. Therefore, there are 2 possible approaches to calibrating the pressure; the first approach is to adjust physical properties of soot cake and wall substrate. The second approach is to adjust the soot oxidation rate which indirectly regulate the thickness of soot cake. Both of them has to be adjusted together to replicate the pressure drop correctly. This was done by trial and error method by guessing from the possible value suggested in the literature.

Some of the parameters for pressure drop can be set to 'define' value which means they are calculated by the correlation found in the literature.

### A.1.1 Clean wall calibration

**Clean filter wall permeability**

This parameter governs the flow resistance in the substrate wall. Thus, affects the slope of the pressure-volumetric flow rate. This value can either be calibrated using clean filter experiments or calculated using the filter properties and following relationship from Dullien et al, 1979:

$$k_{p,s}(\mathtt{i},0) = \frac{\epsilon_s^3(\mathtt{i},0)d_{pore}^2}{180\big(1-\epsilon_s(\mathtt{i},0)\big)^2}$$

### A.1.2 Soot loading calibration

**Percolation constant**

This parameter is used to controls the magnitude and timing of the pressure drop at the transition point from deep bed filtration mechanism to soot cake filtration mechanism. This should be the first parameter to calibrate and in conjunction with the packing density of substrate and cake.

**Packing density of substrate and cake**

The packing density in the substrate controls the slope of the pressure drop vs. time during deep bed filtration regime. While the packing density in the soot cake layer controls the slope of the pressure drop vs. time during the soot cake filtration regime.

**Soot cake layer porosity**

Similar to the substrate wall permeability, this value is used to tune the slope of the pressure-volumetric flow curve of the soot cake. Which will have fine-tuned effect on the pressure drop vs. time slope. Since as soot cake is building up, the wall velocity is decreasing.

**Soot cake layer permeability**

This parameter is used to adjust how soot cake resistance to the flow. Which affect the pressure drop by adjusting its slope when plot against the volumetric flow. The equations shown here are from a paper by Konstandopoulos et al. [62].

$$k_{p,cake} = f(\epsilon_{cake}) \cdot d_0^2 \cdot SCF$$

$$f(\epsilon_{cake}) = \frac{2}{9} \cdot \frac{2 - \frac{9}{5}(1-\epsilon_{cake})^{1/3} - \epsilon_{cake} - \frac{1}{5}(1-\epsilon_{cake})^2}{1-\epsilon_{cake}}$$

$$SCF = 1 + Kn \cdot \left(1.257 + 0.4 \cdot exp(\frac{-1.1}{Kn})\right)$$

$$Kn = \frac{2\mu}{d_0\rho_g} \cdot \sqrt{\frac{\pi M_g}{2RT}}$$

## A.2 Deep filtration parameters

Deep bed filtration model governs how much soot can be stored by the wall substrate. The key parameter is the local collection efficiency which is used to adjust how much soot is collected in each discretized substrate layer. Substrate wall permeability and substrate wall porosity change with the amount of soot that filled up the substrate. This is done by default by GT-POWER when collection efficiency is set to ’defined’ [46]. The equations shown here origin from by Kladopoulou et al. [68].

$$E(\mathtt{i},t) = 1 - exp\Big( - \frac{3\eta_{DR}(\mathtt{i},t) \cdot (1 - \epsilon_s(\mathtt{i},t)) \cdot w_s(\mathtt{i})}{2 \cdot \epsilon_s(\mathtt{i},t) d_c(\mathtt{i},t)} \Big)$$

$$\eta_{DR} = \eta_D + \eta_R - \eta_D \cdot \eta_R$$

$$\eta_D = 3.5 \cdot g(\epsilon_s) \cdot Pe^{-2/3}$$

$$\eta_R = 1.5 \cdot N_R^2 \frac{g(\epsilon_s(\mathtt{i},t))^3}{(1 + N_R)^{\frac{3-2\epsilon_s(\mathtt{i},t)}{\epsilon_s(\mathtt{i},t)}}}$$

$$N_R = \frac{d_0}{d_c(\mathtt{i},t)}$$

$$\epsilon_s(\mathtt{i},t) = 1 - \big(\frac{d_c(\mathtt{i},t)}{d_c(\mathtt{i},0)}\big)^3 \cdot (1 - \epsilon_s(\mathtt{i},0))$$

$$d_c(\mathtt{i},t) = 2 \cdot \Big(\frac{3}{4\pi} \frac{m_w(\mathtt{i},t)}{\rho_{soot,wall}} + \big(\frac{d_c(\mathtt{i},0)}{2}\big)^3\Big)^{1/3}$$

$$d_c(\mathtt{i},0) = \frac{3(1 - \epsilon_s(\mathtt{i},0))}{2\epsilon_s(\mathtt{i},0)} \cdot d_{pore}$$

$$g(\epsilon_s) = \Big(\frac{\epsilon_s(\mathtt{i},t)}{2 - \frac{9}{5}(1 - \epsilon_s(\mathtt{i},t))^{1/3} - \epsilon_s(\mathtt{i},t) - \frac{1}{5}(1 - \epsilon_s(\mathtt{i},t))^2}\Big)^{1/3}$$

$$\frac{k_{p,s}(\mathtt{i},t)}{k_{p,s}(\mathtt{i},0)} = \Big(\frac{d_c(\mathtt{i},t)}{d_c(\mathtt{i},0)}\Big)^2 \frac{\epsilon_s(\mathtt{i},t)}{\epsilon_s(\mathtt{i},0)}$$

## A.3 Calculation of carbon active site density

The carbon active site density is calculated from the carbon species balance by integrating with respect to time on the outlet concentration of $CO$ and $CO_2$. Assuming all the soot deposited in the monolith is consumed, then the integration yields carbon moles initially deposited in the system. The equation is as followed:

$$\lambda_{carbon} = C_{carbon} = \frac{\int_{t=0} \dot{n}(t) \cdot 10^{-6} \cdot (CO_{<ppm>} + CO_{2<ppm>})dt}{V} \tag{A.1}$$

Where $\dot{n}(t)$ is the molar flow rate at time t and V is the reactor volume. For surface active site density, the calculation is presented by Carlsson [15].

$$\lambda_{surface} = \frac{6m_{C_0}(1 - X_c)^{2/3}}{d_0 \rho_{soot} N_A A_d V} \tag{A.2}$$

Where $m_{C_0}$ is the initial carbon mass in the system, the term $(1 - X_c)^{2/3}$ is accounted for in the shrinking core term. $d_0$ is the diameter of the soot spherules which is assumed to be 25 nm. $\rho_{soot}$ is the packing density of the soot. $N_A$ is the Avogadro's number. $A_d$ is the surface area on the spherules occupied by a single active site which is assumed to be 0.8 nm$^2$|||[|||||||||15|||]{[.

## A.4 Reaction Modules in GT-POWER

GT-POWER provides three types of reaction modules which are 1) global reaction, 2) gaseous reaction and 3) surface-reaction. Only the surface-reaction module was used in this thesis. The advantage of surface-reaction module lies in the built-in support for surface active site species which can be used to simulate the absorption and desorption. The DPF module accounts for the local concentration of soot. This is the only built-in method provided by GT-POWER to react and track solid-phase soot trapped inside the DPF.

The unit of rate of reaction is specified by the conditioned set in rate expression basis option. There are 3 types of possible options which are turnover (site) basis, reactor volume basis, and surface area basis. The final unit are $\frac{mol}{s \cdot mol_{site}}$, $\frac{mol}{s \cdot m^3}$ and $\frac{mol}{s \cdot m^2}$ respectively. The turnover basis is the recommended settings suggested by GT-POWER manual [46]. The settings requires user to define the associated site species for the reaction.

To convert volume basis reaction rate to turnover basis, multiply the reaction rate by active site density associating with the reaction. In the same manner, converting volume basis reaction rate to surface area basis is done by dividing the specific surface area.

$$\begin{aligned} r_{j,turnover} &= \lambda_j \cdot r_{j,volume} \\ r_{j,area} &= \frac{1}{S_p} \cdot r_{j,volume} \end{aligned} \tag{A.3}$$

where $\lambda_j$ is the active site density associated with reaction j and $S_p$ is the specific surface area.

## A.5 Calculation of frequency factor of oxygen adsorption

Both model 1 and 2 assumes an oxygen adsorption step, equation (2.26) and (2.33). The corresponding frequency factor $F$ for these reactions is assumed to be according to collision theory with a sticking factor of 1.

$$F = 2\pi\sigma_{O-C}\sqrt{\frac{8RT}{\pi\mu_m}}N_A \tag{A.4}$$

$\sigma_{O-C}$ is the molecular distance between oxygen and carbon, R the gas constant, T temperature in K and $\mu_m$ is the reduced mass of carbon and oxygen:

$$\mu_m = \frac{M_C M_{O_2}}{M_C + M_{O_2}} \tag{A.5}$$

# B

# Appendix - Implementation techniques

Special techniques were developed to allow detailed kinetics model implementation in the soot cake layer. The idea of this technique is to put all of the active regeneration reactions intended for cake layer in the substrate layer instead (since it is the only option) and exchange information between them. The information about soot mass is sent from cake layer to substrate layer to calculate the soot consumption rate. Then, soot consumption rate is sent back to the cake layer to adjust soot mass accordingly (see. Figure B.1).

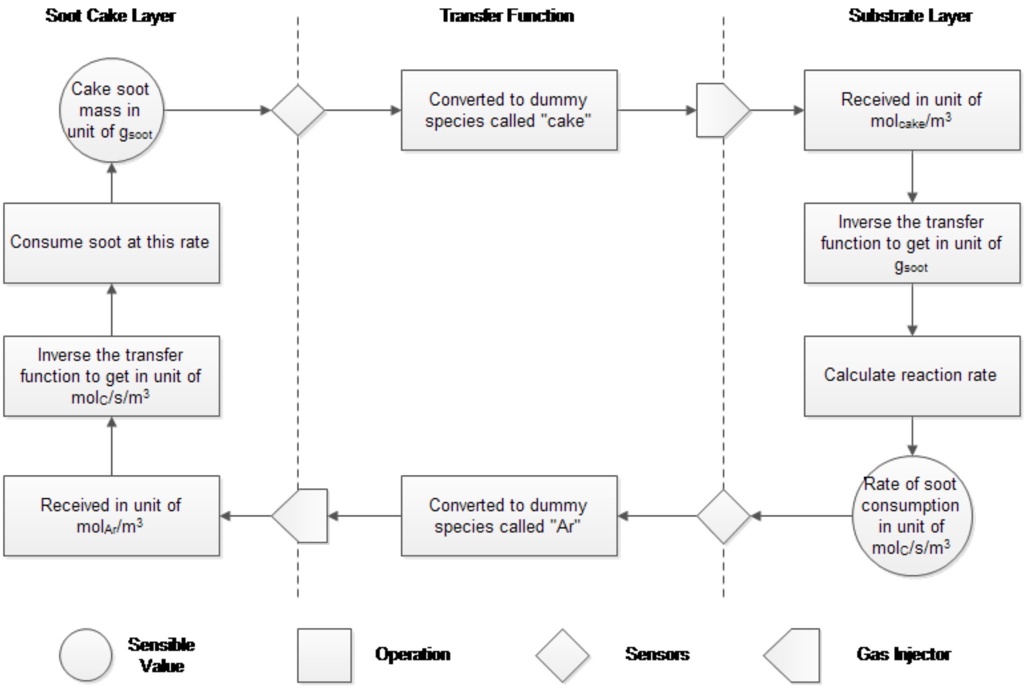

**Figure B.1:** Process flowchart of the technique. The loop runs once for every simulation time step.

The inputs which can dynamically reach the reaction module are temperature, pressure, and species concentration in gas-phase in the unit of $mol/m^3$. Therefore, two dummy species were created with the objective of carrying the information we wanted to pass. These dummy species should not be viewed as reactant that can be depleted. This was done by set the species solver to exclude them from the species balance.

Injecting new species to the inlet will affect the mole and mass fraction. To minimize the effect, the injected species have to be in trace amount. This was done by scaling down the injection and scaling up the reaction rate calculation to receive the right value.

The reaction in the substrate needs information about the soot mass left in the soot cake layer. Imaginary species of Argon-Carbon(Ar-C) was used as a dummy species to carry this information; it is referred as "cake" species in the model. Soot mass in cake layer data was gathered by connecting a sensor to the DPF and sent it to the math function to scale down (in this case, scale it down by 1E7 times). Finally, it was passed to the injector. The information is injected into the inlet in the unit of grams per second.

In the reaction rate calculation, the species concentration (in the unit of $mol_{dummy}/m^3$) has to be converted back to gram per second. The conversion factor is shown to be:

$$C_{dummy} \cdot (M_{dummy} \cdot \dot{V}) = \dot{m}_{dummy} \tag{B.1}$$

With this factor multiplied, the reaction solver received the right information of soot mass in the cake layer. This information was used to calculate the shrinking core term $[C_0](1 - X_c)^{2/3}$. Where $[C_0]C, 0$ is the initial soot concentration which was lumped in the pre-exponential factor. In the DPF, it is better to use local soot concentration to avoid ambiguity in the case of new soot is deposited faster than being consumed. Therefore, the shrinking core terms become $(C_{soot})^{2/3}$. Note that $[C_0]$ was found to be 4 and was taken out from the pre-exponential factor.

To converted to soot concentration, conversion factor is:

$$\begin{aligned} \dot{m}_{dummy} &= m_{soot} \\ m_{soot} \cdot (\frac{1}{M_{soot}} \cdot \frac{1}{\dot{V}}) &= C_{soot} \\ \therefore C_{soot} &= C_{dummy} \cdot \frac{M_{dummy}}{M_{soot}} \end{aligned} \tag{B.2}$$

The consumption rate of soot has to be sent to the cake layer to take out the exact amount of soot mass. Imaginary species of Argon (Ar) was used as a dummy species to carry this information, it is referred as "Ar" species in the model. The consumption rate was gathered by measuring the reaction rate of every reaction that consumes soot. The information was scaled down and injected to the inlet gas in the same manner as discussed before. Only the conversion factor B.1 is needed in this case because the unit of the reaction rate is in $mol/s/m^3$.

The disadvantage of this approach is that the cake kinetics model will use the pressure, temperature and linear velocity of the substrate resulting in wrong reaction rate prediction. The same technique can be used to transfer these parameters from the cake to the kinetics model to treat the problem.

# C

# Appendix - Semi-steady state DPF data sets

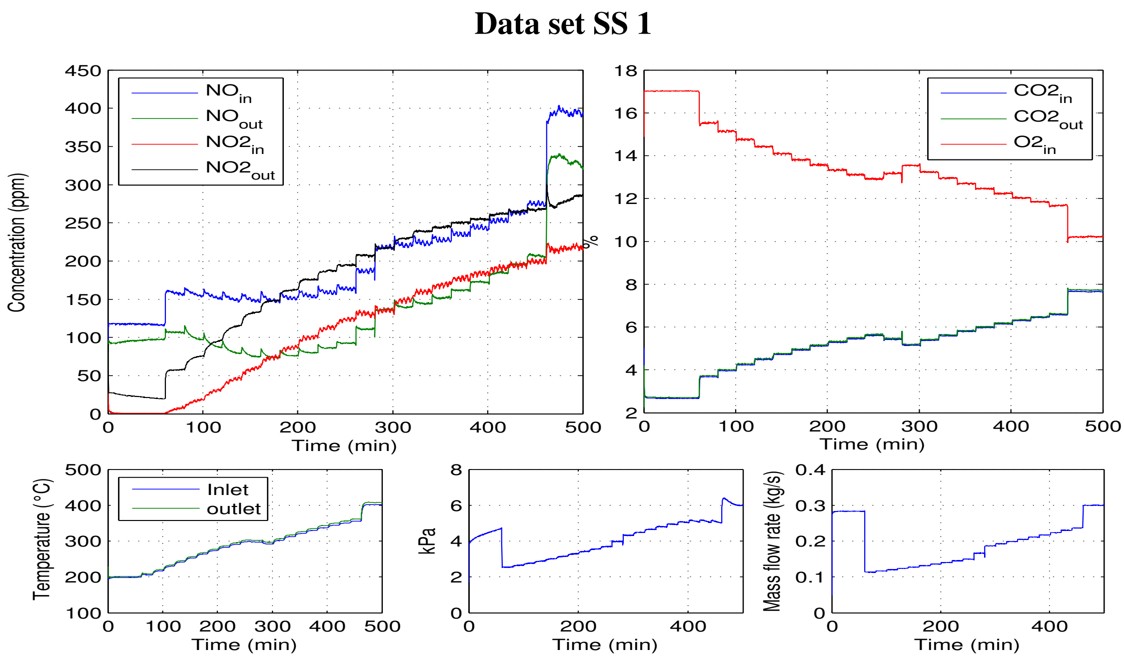

**Figure C.1:** Semi-steady state engine data with step-wise increment in temperature from 200-400°C with exhaust flow rate 0.1-0.3 kg/s.

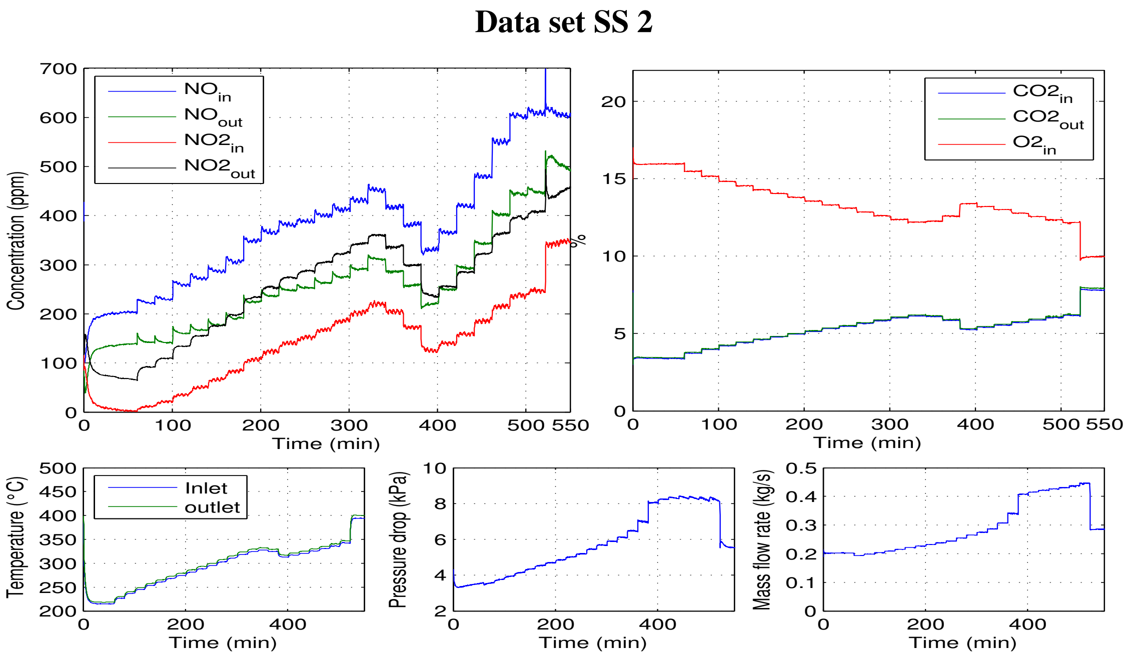

**Figure C.2:** Semi-steady state engine data for temperature between 220-400°C where the exhaust flow rate is 0.19-0.45 kg/s. The $NO_x$ level is higher here than data set SS 1.

# D

# Appendix - Transient DPF data sets

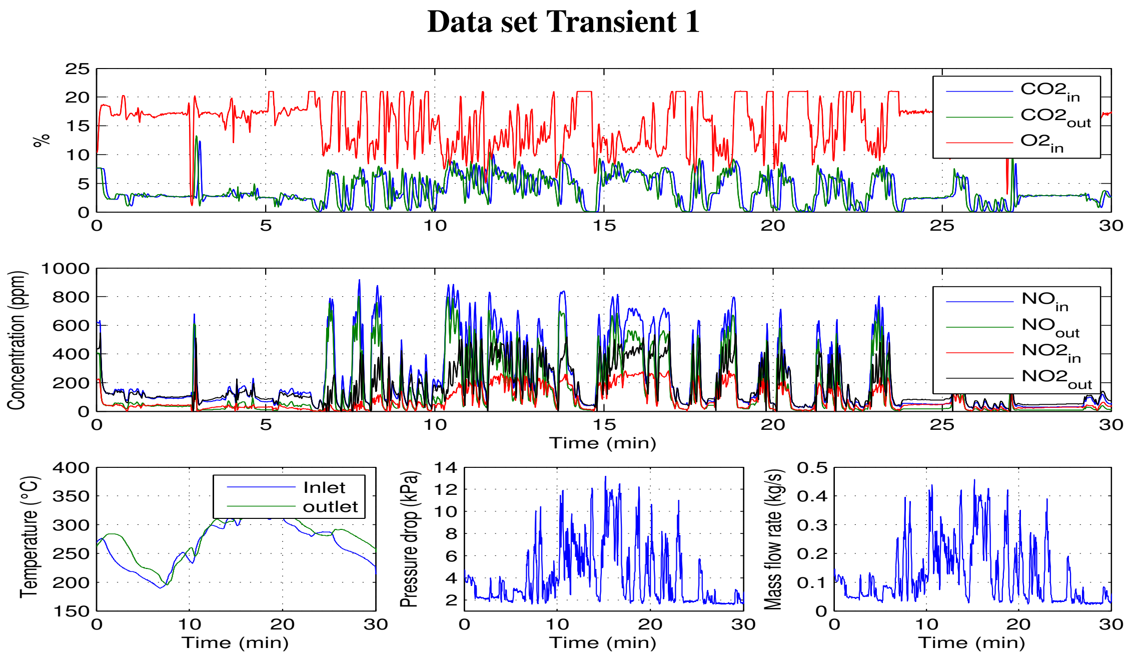

Data set Transient 1

**Figure D.1:** The plot represents of one of six cycles lasting 30 min. The initial soot loading 4.68g/L and post-experiment 4.32g/L. Bottom right plot shows the mass flow rate of the exhaust as the air intake increases along with the fuel injections. Middle row plot shows $NO$ is converted to $NO_2$.

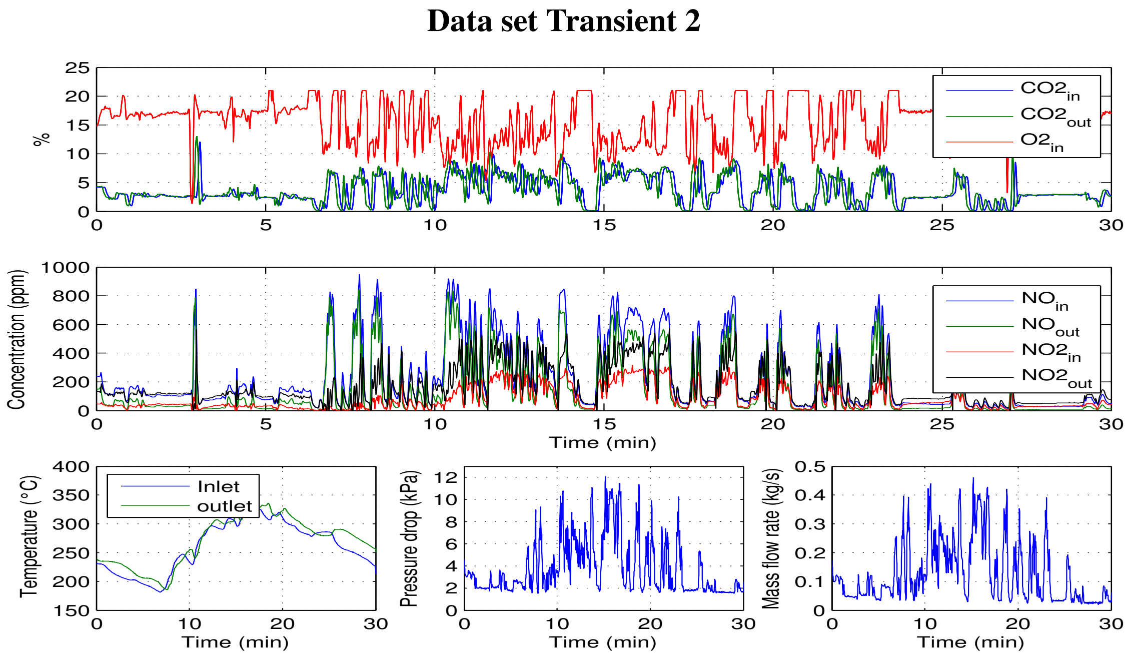

Data set Transient 2

**Figure D.2:** The plot represents of one of six cycles lasting 30 min with a temperature range of 200-350°C. The initial soot loading 4.32g/L and post-experiment 4.09g/L.

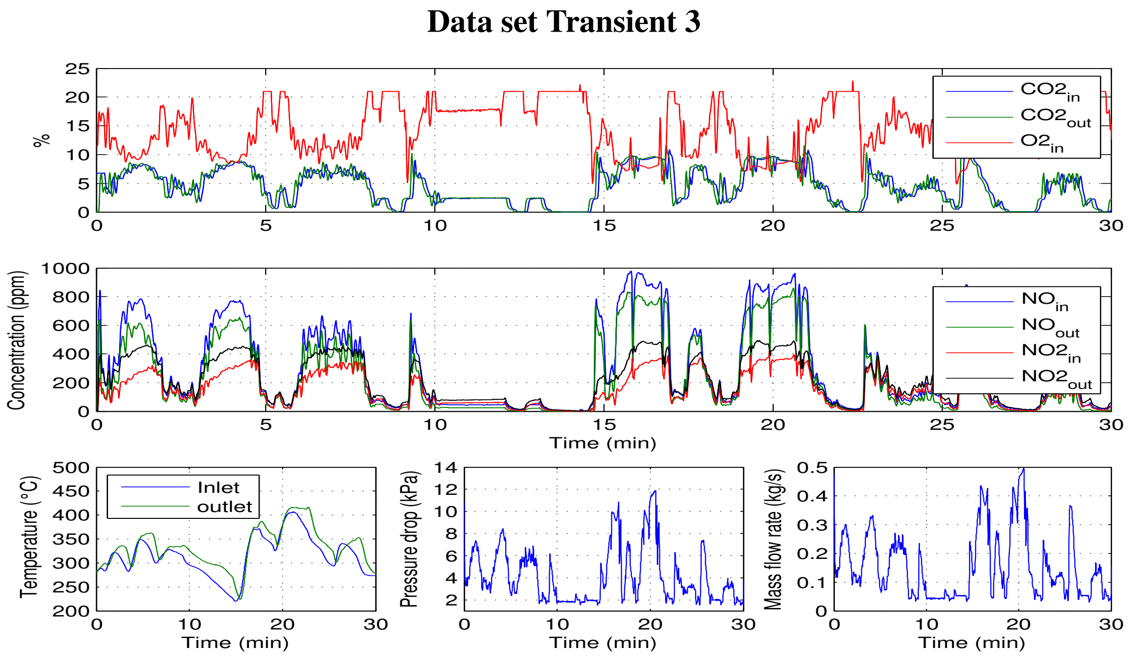

**Figure D.3:** Data from one of three high temperature exhaust flow cycles from 224-416°C. The initial soot loading 4.09g/L and post-experiment 0.99g/L.

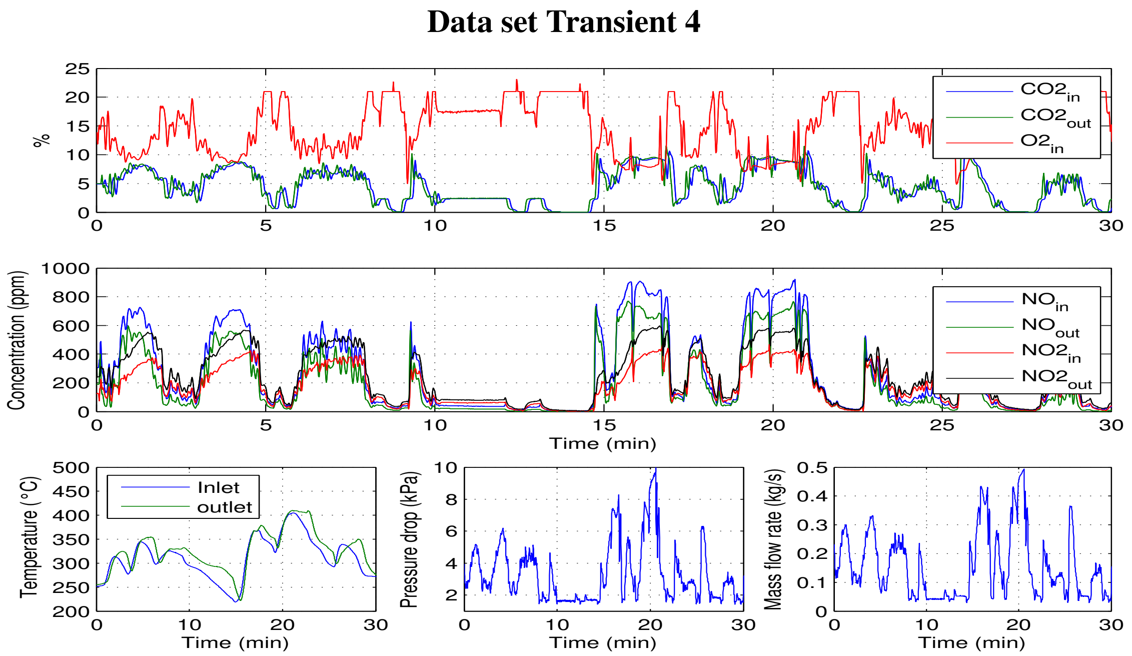

**Figure D.4:** Engine data from high temperature cycles 224-416°C. The initial soot loading 0.99g/L and post-experiment 0.32g/L.

# E

# Appendix - Simulation results of Semi-steady state data sets

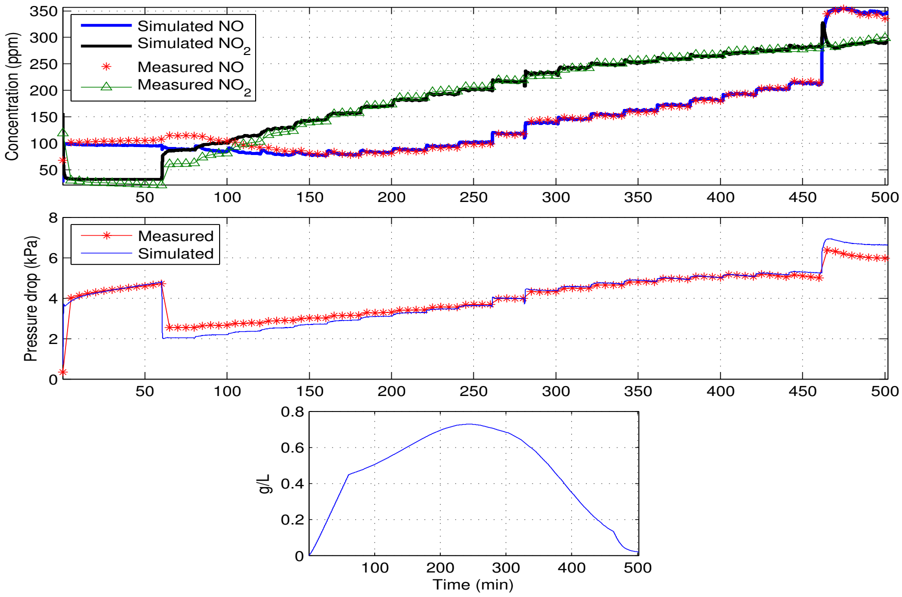

**Figure E.1:** Simulation results of data set SS 1. The pressure drop model was able to explain 92.9% of the variance, while the $R^2$ for $NO$ oxidation model indicated 98.6% .

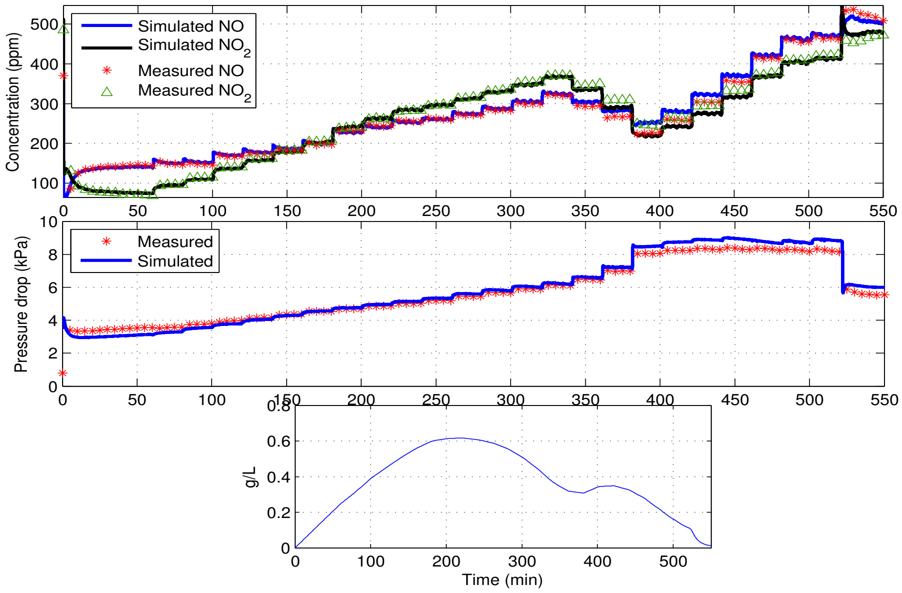

**Figure E.2:** Simulation results of data set SS 2. The pressure drop model was able to explain 99.2% of the variance, while the $R^2$ for $NO$ oxidation model indicated 96.17%

# F

# Appendix - Simulation results of transient DPF data sets

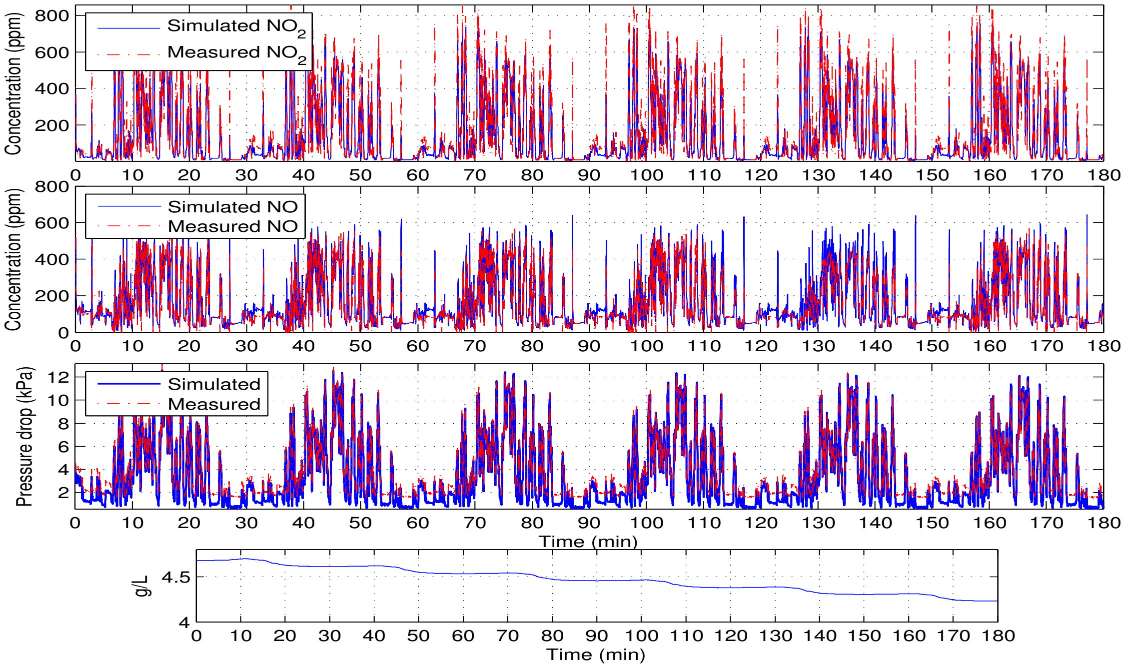

**Figure F.1:** Simulation results from data set Transient 1, where the pressure drop model was able to explain 90.1% of the variance and the $NO$ oxidation model had $R^2 = 0.934$, see also F.5 for zoomed version of the plot.

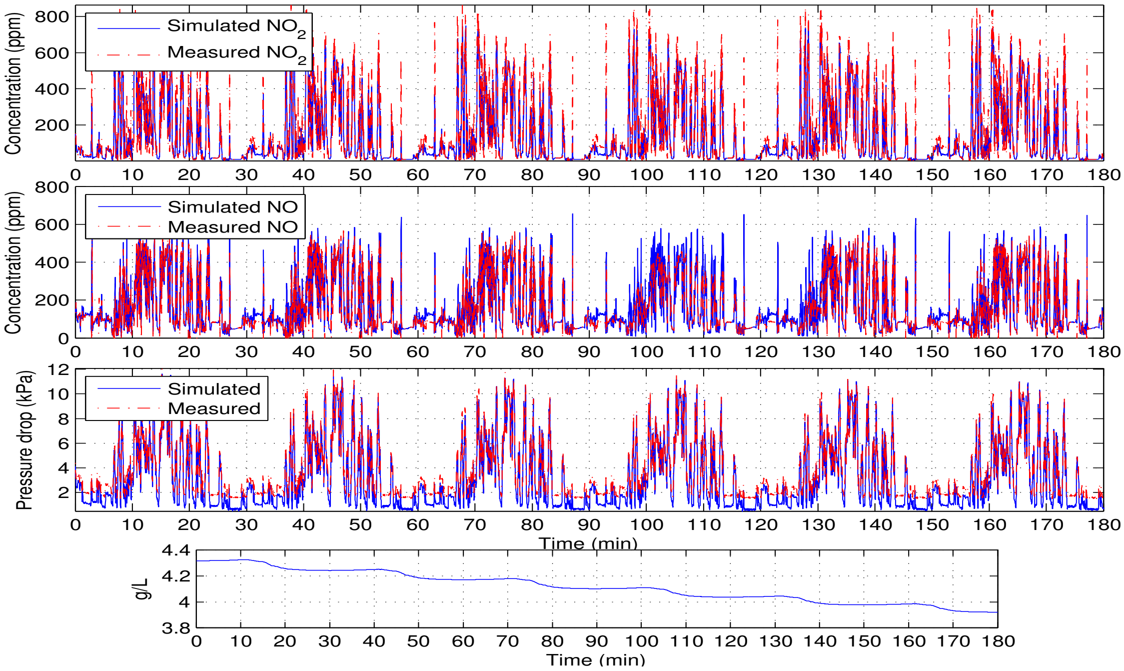

**Figure F.2:** Simulation results from data set Transient 2. Pressure drop model $R^2 = 0.920$ and the $NO$ oxidation model $R^2 = 0.906$, see also F.6 for zoomed version of the plot.

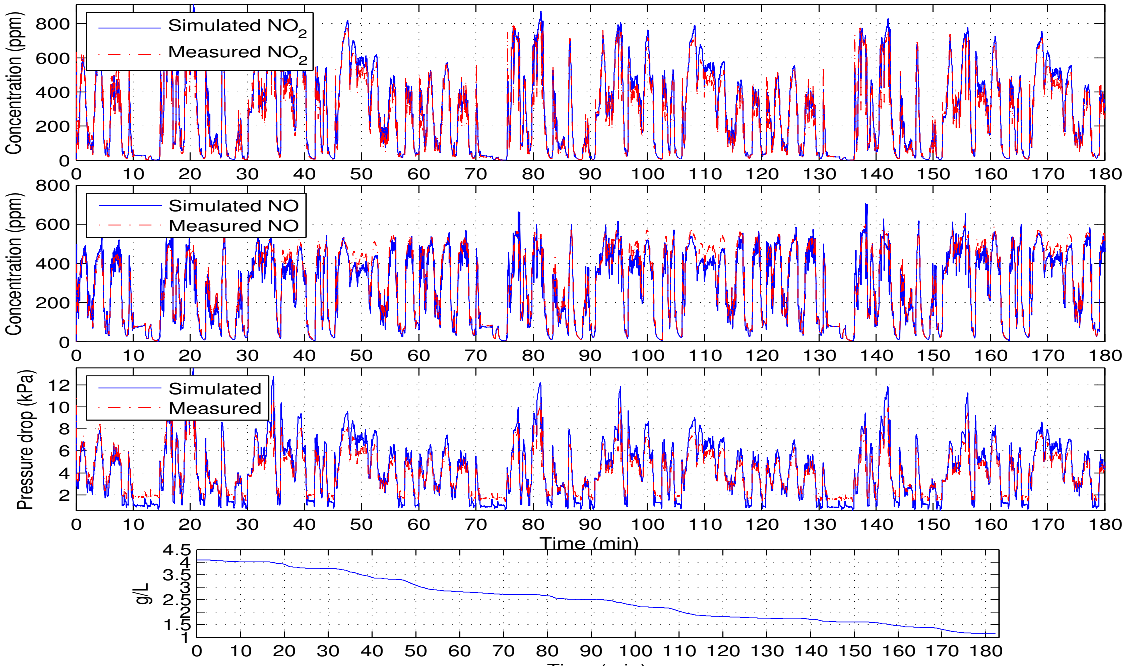

**Figure F.3:** Simulation results from data set Transient 3. Pressure drop model $R^2 = 0.967$ and the $NO$ oxidation model $R^2 = 0.880$, see also F.7 for zoomed version of the plot.

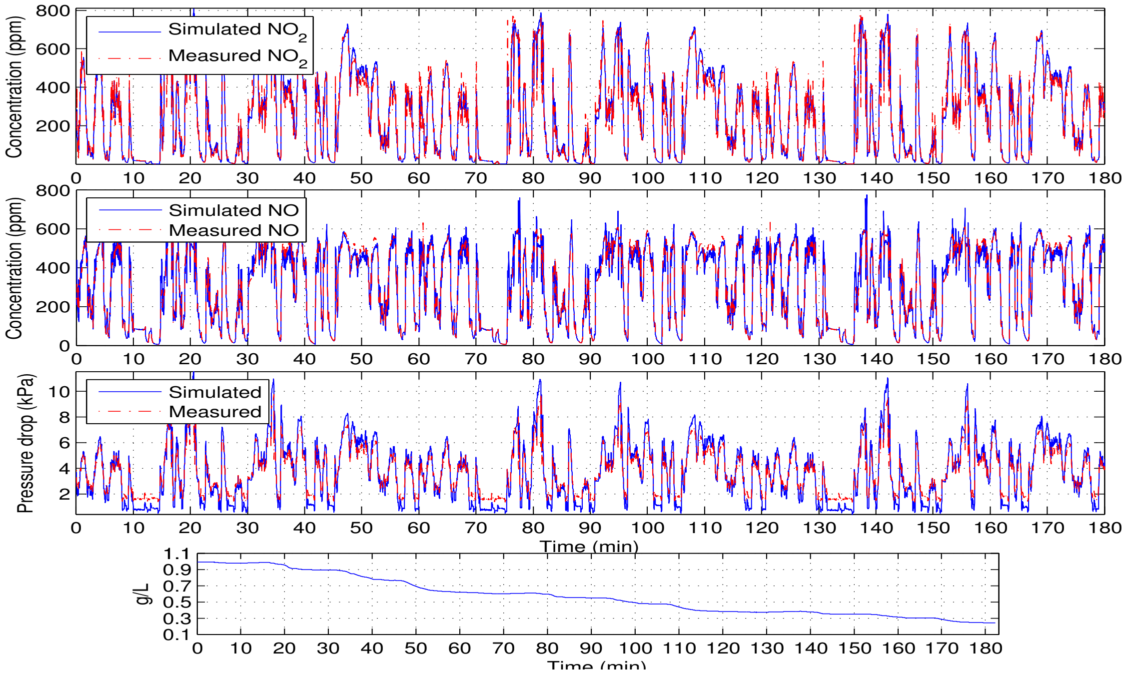

**Figure F.4:** Simulation results from data set Transient 3. Pressure drop model $R^2 = 0.893$ and the $NO$ oxidation model $R^2 = 0.975$, see also F.8 for zoomed version of the plot.

## Zoomed figures

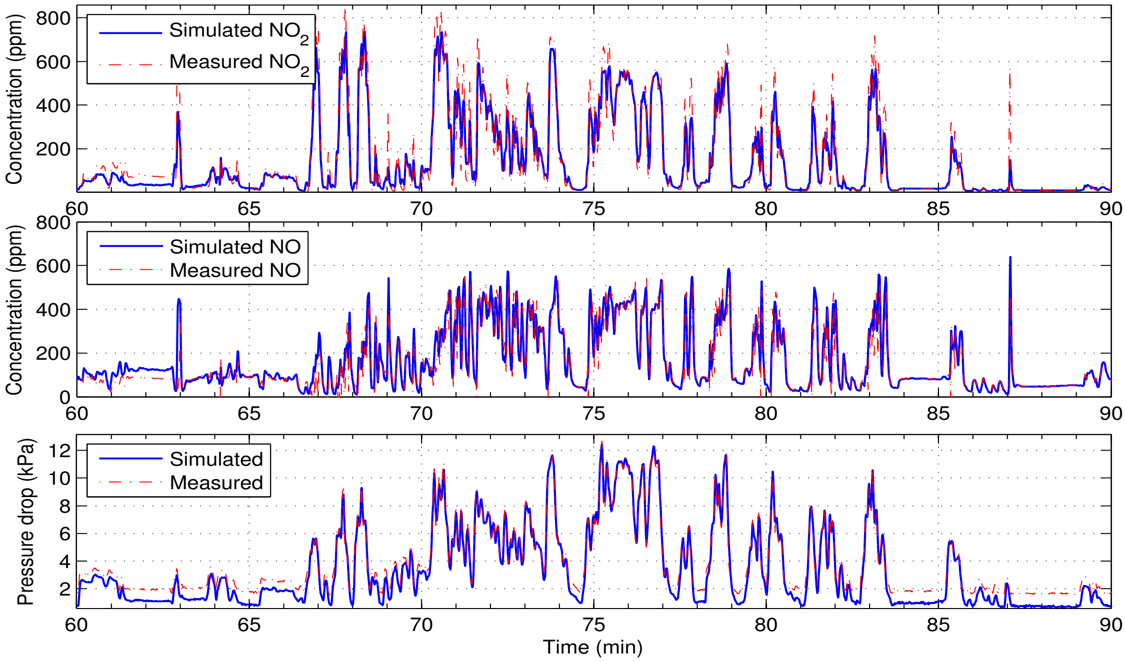

**Figure F.5:** Zoomed plot of the Transient 1 simulation result.

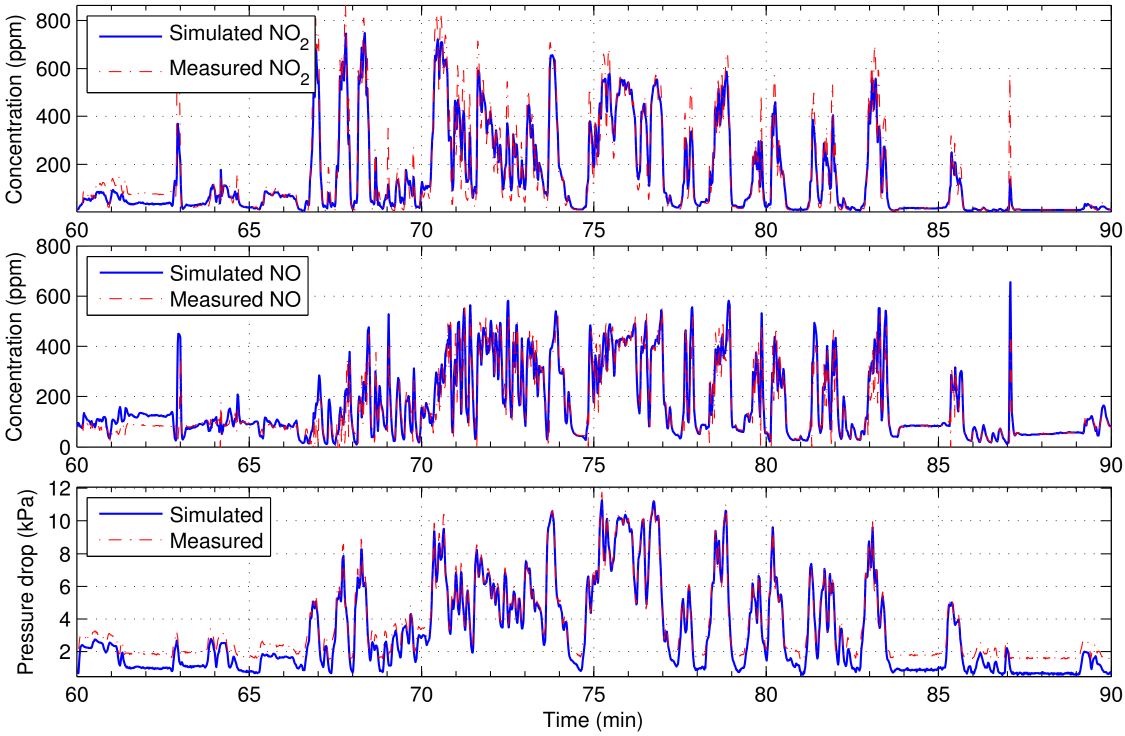

**Figure F.6:** Zoomed plot of the Transient 2 simulation result.

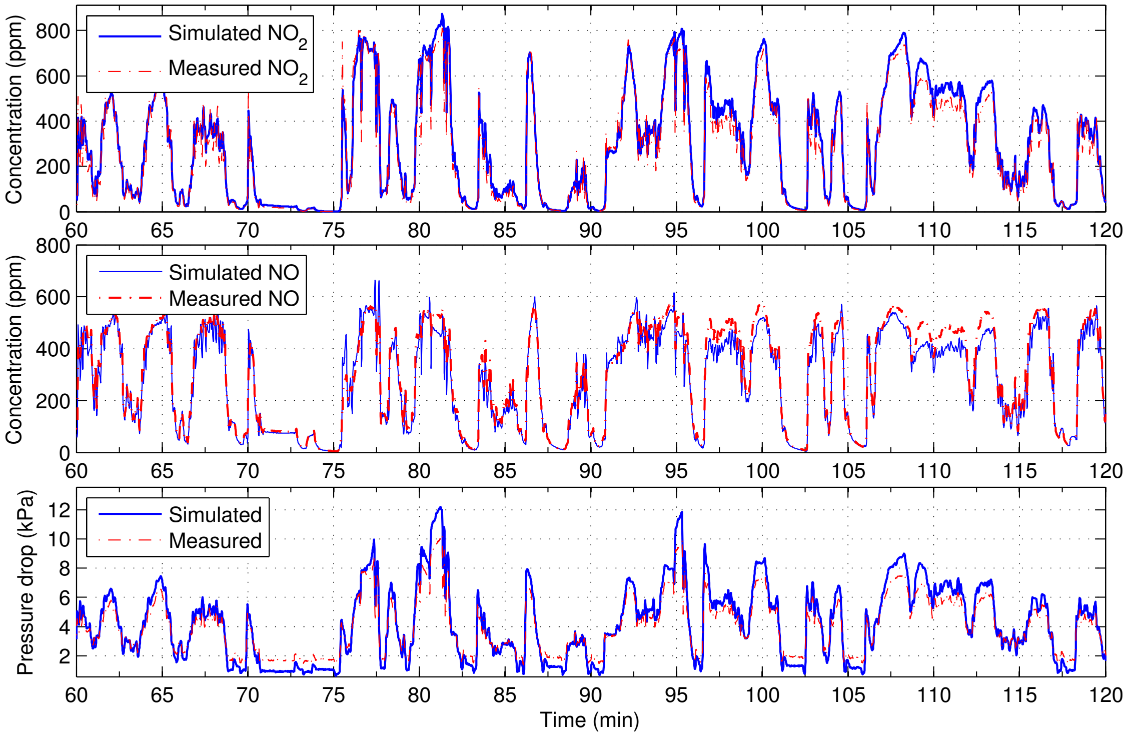

**Figure F.7:** Zoomed plot of the Transient 3 simulation result.

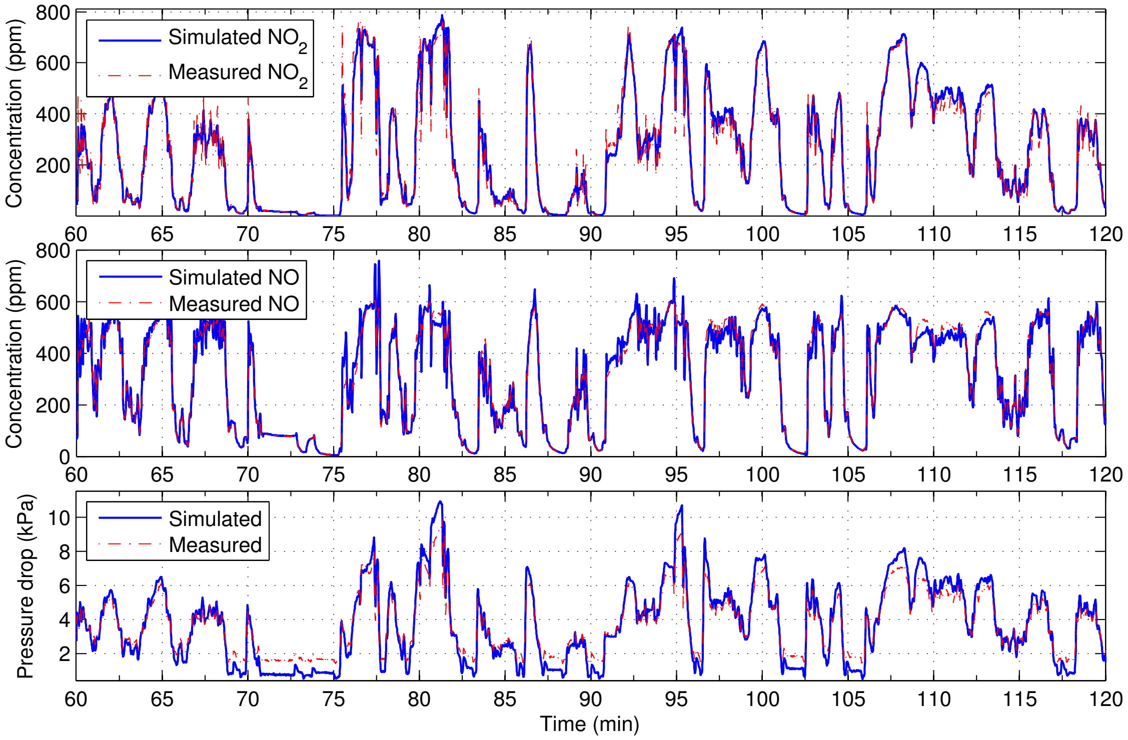

**Figure F.8:** Zoomed plot of the Transient 4 simulation result.